AN IMPROVED MEASUREMENT OF THE HUBBLE CONSTANT USING THE SUNYAEV-ZELDOVICH EFFECT

THESIS BY
BRIAN S. MASON

IN PARTIAL FULFILLMENT OF THE REQUIREMENTS OF THE DEGREE OF DOCTOR OF PHILOSOPHY

UNIVERSITY OF PENNSYLVANIA
PHILADELPHIA, PENNSYLVANIA

1999

This thesis is dedicated to the memory of Dora B. Mason

Acknowledgements

While this thesis contains five years of my own time and effort, it contains much more than this of the vision, dedication, and friendship of others. I thank my advisor Steve Myers for introducing me to the brave new world of radio astronomy, giving an unforgettable first tour of the Owens Valley, and having enough confidence in my abilities to give me free reign (through trials and tribble-ations) for the past couple of years. This work is an outgrowth of the survey he began some time ago, and what success we have had is in no small part due to the hard work and imagination he invested at the start. During my year of voluntary exile in California, Erik Leitch often served as a surrogate advisor. He never hesitated to answer my questions, and was always exemplary of an inspiring standard of excellence. Aside from this, his brainchild `CMBPROG` has been inexpressibly useful for a wide range of tasks including, but not limited to, the reduction of single-dish telescope data. I thank Tony Readhead for guidance and good cheer throughout this work, as well as his support for the project.

The OVRO 5.5-meter telescope in its current incarnation is the result of the work of many people. Aside from those mentioned above, Tom Herbig and Charlie Lawrence put in vital efforts towards making the 5.5-meter fit for ground-based CMB observations. Our undertakings at the Owens Valley have been blessed by a team of very talented engineers: Harry Hardebeek, Mark Hodges, and Russ Keeney. These individuals, together with software maven Tim Pearson, have created a reliable and easy-to-use system at OVRO.

The road to cluster models would have been longer and lonelier without the remarkable helpfulness of a few members of the x-ray community. I thank in particular Maxim Markevitch, Steve Snowden, and Alexey Vikhlinin for the advice and software they happily provided at the start of my efforts. At a later stage, conversations with Joe Mohr were very helpful in refining and improving the Monte Carlo procedures we used to evaluate our cluster models.

I thank Russ Keeney for assistance at a few key points in the 1.5-meter absolute calibration project, Stan Hudson for constructing the cold load box, John Cartwright of Caltech for assistance in the initial characterization of the receiver in September of 1997, and the OVRO Millimeter Array staff for useful discussions and periodic loans of equipment. Thanks to Ken Kellermann, Ed Wollack, and Tim Pearson for comments on Chapter 5 which improved the content and presentation.

Friends near and far made the journey more pleasant. Without Vibhat Nair, the past few years wouldn't have been the same. He is a person of rare quality whom I will miss. I thank Mary D'Aiuto for her friendship, and for many clocks. Quintessential cosmologist Rob Caldwell always seemed to know the happening places in Old City, and assorted adventures and misadventures with Ben Oppenheimer made my stay in Pasadena enjoyable. Kevin Marvel and Hemant Shukla showed me the cultural hot spots of the Bishop metropolitan area, and fellow astronomers (and Pez/Orange Monkey enthusiasts) Dan Marlow and David Rusin were always good company in Philadelphia. I thank Barbara King for Zen dinners, Fritz the über puppy, endless conversation, rainy mornings at Lutecia, and everything else that for the past year has made life outside of work so rewarding. Without her kind and encouraging words the months of thesis-writing would have been much more difficult than they were.

Finally and most of all I thank my family: Mom, Dad, Anne, Aunt Audrey, Papa, and my late grandmother. Whatever I may have achieved owes much to the generous and unhesitating love, support, and encouragement they have given through the years. I would count myself lucky to have any one of these individuals in my life, and am truly blessed to have them all.

Abstract

We present an improved measurement of the Hubble Constant (H_0) based on observations of the Sunyaev-Zeldovich Effect (SZE) in 5 nearby galaxy clusters from an x-ray flux-limited sample. This measurement incorporates cluster observations from the Owens Valley Radio Observatory (OVRO) 5.5-meter radio telescope, improved cluster models based on public ROSAT PSPC data, and an improved radio frequency absolute calibration based on observations with the OVRO 1.5-meter telescope.

A 90% volume complete x-ray sample of 31 clusters with $F_x > 1.0 \times 10^{-11}\,\mathrm{erg\,cm^{-2}\,s^{-1}}$, $L_x > 1.13 \times 10^{44}\,h^{-2}\,\mathrm{erg\,s^{-1}}$, and $z < 0.1$ is defined based on an x-ray cluster sample existent in the literature. We analyze ROSAT PSPC data for 22 of these clusters, deriving masses and SZE predictions accurate to $\sim 5\%$. In conjunction with electron temperatures from the literature we find a mean gas mass fraction of $(7.02 \pm 0.28)\,h^{-3/2} \times 10^{-2}$ at a radius of $\sim 1\,h^{-1}$ Mpc.

Our absolute calibration yields a flux density $S_{Cas,1998} = 194^{+5}_{-6}$ Jy at 32.0 GHz for the bright supernova remnant Cas-A, which becomes the basis for our SZE calibration. New observations of A399 were conducted from October 1996 through March 1997, yielding $\Delta T_{obs} = -187 \pm 21\,\mu\mathrm{K}$. With our ROSAT model, this gives $H_0 = 85^{+27}_{-23}\,\mathrm{km\,s^{-1}\,Mpc^{-1}}$. Observations of A478, Coma, A2142, and A2256, together with our models, yield $H_0 = 61^{+15}_{-14}$, 61^{+23}_{-21}, 80^{+19}_{-17}, and 68^{+21}_{-19} $\mathrm{km\,s^{-1}\,Mpc^{-1}}$ respectively. The sample average is $H_0 = 71(\pm 5)_{rand.}(\pm 8)_{calib.}\,\mathrm{km\,s^{-1}\,Mpc^{-1}}$. This is the most accurate measurement of H_0 from the SZE to date, and the only one based on an unbiased cluster sample. Our result is in agreement with recent Cepheid-based determinations of the Hubble constant, as well as the results of other more traditional measurements, confirming the integrity of the local distance ladder.

Contents

List of Figures

List of Tables

Chapter 1

Introduction

1.1 Scientific and Historical Background

The Sunyaev-Zeldovich Effect (SZE) is a distortion in the spectrum of the Cosmic Microwave Background (CMB) caused by inverse Compton scattering of CMB photons by hot electrons. Its existence was first predicted by Sunyaev & Zeldovich (1970), shortly after the discovery of the CMB by Penzias & Wilson (1965). Not long after the prediction of Sunyaev and Zeldovich, the Coma and Perseus clusters of galaxies were discovered to be bright sources of x-rays (Fritz et al. 1971; Gursky et al. 1971). Data from the UHURU satellite (Giacconi et al. 1972) confirmed that many other clusters of galaxies were also strong x-ray emitters, as well as suggesting that the emission came from extended and not discrete sources, and there was soon great interest in the problem of determining the origin of the x-rays. It was from this perspective that the first searches for the SZE in clusters of galaxies were undertaken (Gull & Northover 1976). X-ray spectra of galaxy clusters obtained by ARIEL V showed the exponential slope characteristic of thermal bremsstrahlung emission from a hot plasma, as well as the 7 keV iron line (Mitchell et al. 1976). This latter feature strongly argued against the dominant alternative models existent at the time (Bahcall & Sarazin 1977), and it was soon accepted that the x-ray emission from galaxy clusters originated in thermal plasmas with temperatures $kT_e \sim 7$ keV and densities of $n_e \sim$ a few $\times\ 10^{-3}\mathrm{cm}^{-3}$. For an excellent overview of the subject of x-ray clusters and its history, see Sarazin (1988).

The form of the spectral distortion in the CMB due to inverse Compton scattering by thermal electrons is given by

$$\frac{\Delta I_\nu}{I_\nu} = \tau \frac{xe^x}{e^x - 1} \times \frac{kT_e}{m_e c^2} \left[x \coth(x/2) - 4\right] \tag{1.1}$$

where I_ν is the specific intensity of the radiation incident upon the hot gas, $x = h\nu/kT_{CMB}$, and τ is the optical depth for inverse Compton scattering. This is given by

$$\tau = \sigma_T \int dz\, n_e(z) \tag{1.2}$$

where σ_T is the Thompson scattering cross-section and the integral is along the line of sight. At low frequencies ($x << 1$), the specific intensity of a blackbody is simply $2kT/\lambda^2$, and Eq. 1.1 takes the form

$$\frac{\Delta T}{T} = \tau \frac{xe^x}{e^x - 1} \times \frac{kT_e}{m_e c^2} \left[x \coth(x/2) - 4\right] \tag{1.3}$$

or simply

$$\frac{\Delta T}{T} = -2\,\tau \times \frac{kT_e}{m_e c^2}. \tag{1.4}$$

With path lengths ($\sim$ 1Mpc), densities, and temperatures characteristic of rich clusters of galaxies, this gives temperature decrements of $100 - 500\ \mu$K. The peak microwave decrement is independent of the redshift of the electron cloud which generates it.

Cavaliere et al. (1979) pointed out that with the improved understanding of the ICM which had resulted from advances in x-ray astronomy, SZE measurements could be used to directly determine the luminosity distance to a cluster. Such a determination bypasses systematic uncertainties introduced at each step by bootstrap methods of measuring the distance scale. As we will discuss in Chapter 2, x-ray observations yield a measurement of the electron density profile in the cluster up to a power $h^{1/2}$ (at low redshifts)[1]. In conjunction with an electron temperature obtained from the x-ray spectrum, we can predict the SZ decrement which would be observed if $h = 1$. By comparing this with radio-frequency observations of the decrement, we determine H_0:

$$h = \left(\frac{\Delta T_{pred}}{\Delta T_{obs}}\right)^2. \tag{1.5}$$

[1]Throughout this thesis we use the parameterization $H_0 = 100\,h\,\mathrm{km\,sec^{-1}\,Mpc^{-1}}$. We also assume $q_0 = 1/2$ and neglect any further cosmology dependence in distances; this results in a $\pm 2.5\%$ error in H_0 for $\Delta q_0 = \pm 1/2$ at $z = 0.1$, the redshift limit of our sample.

Two facts should be noted. First, any errors in ΔT_{pred} or ΔT_{obs} will be amplified in H_0 due to the quadratic dependence of the distance on these two quantities. This implies that for an accurate and reliable measurement of H_0, all uncertainties must be well-understood, and efforts must be taken to make them as small as possible. Second, since the x-ray images yield information only in the plane of the sky, it must be assumed that the cluster is spherical in order to predict the SZ decrement. Any systematic departures from spherical symmetry, such as would result in a surface-brightness limited sample which would tend to select objects elongated along the line of sight, will bias the value of H_0 which is inferred. These two facts are the driving considerations behind this thesis and the OVRO SZ survey as a whole; we will return to them shortly.

With the added incentive of a direct measurement of H_0, a few tireless pioneers pursued SZE measurements in clusters throughout the following decade; for a thorough account of these efforts, see Birkinshaw (1999). This proved to be slow going, primarily due to systematic effects such as point source contamination and residual ground signals in the data as well as relatively low-sensitivity receiver systems, and it was not until the 1990's that reliable measurements of the SZE were reported (e.g., Birkinshaw et al. 1991; Herbig et al. 1995; Carlstrom et al. 1996; Grainge et al. 1996). The improvement was due to several factors, not the least of which was an increased sophistication in dealing with the previously mentioned systematics. The development of low-noise, wide-bandwidth HEMT amplifiers also greatly improved the effectiveness of observations; aside from being more sensitive than earlier maser-based receivers, they proved to be significantly more reliable. Bolometer technology evolved during this period, resulting in the first measurements of the SZE at millimeter wavelengths (Holzapfel et al. 1997).

These developments opened new horizons in SZE astronomy. Heartened by the success of Herbig et al. (1995) on Coma using the OVRO 5.5-m system, Myers et al. (1997) undertook an ambitious program to determine H_0 from 5.5-m observations of targets in an x-ray flux-limited sample of 11 nearby galaxy clusters (including Coma). The distinguishing feature of this survey is the sample selection: the Myers et al. sample is drawn from the x-ray selected, x-ray flux limited sample of Edge et al. (1990). Such a sample is less prone to orientation bias than optically selected cluster samples, or higher redshift clusters selected on the basis of exceptional cluster properties. This is especially true at the low redshifts and high luminosity and flux levels which are imposed on the Myers sample. Myers et al. reported observed decrements of $-375 \pm 28\,\mu$K , $-437 \pm 25\,\mu$K, and $-243 \pm 29\,\mu$K on A478 , A2142 , and A2256; together with the Herbig et al. measurement of Coma ($-302 \pm 48\,\mu$K) and x-ray models from the literature, these yield $H_0 = 54 \pm 14\,\mathrm{km\,sec^{-1}\,Mpc^{-1}}$. The quoted uncertainty in H_0 includes a 7% flux density calibration uncertainty as well as estimated $15 - 30\%$ uncertainties in the predicted decrements due to the x-ray models. Calibration and x-ray modeling therefore result in 14% ($\sim \pm 8\,\mathrm{km\,sec^{-1}\,Mpc^{-1}}$) and 30 + % ($\sim \pm 16\,\mathrm{km\,sec^{-1}\,Mpc^{-1}}$ or greater) uncertainties in H_0, respectively, and are clearly the high-priority issues for improving results from the Myers et al. SZE survey.

The bulk of the work in this thesis nucleated around these two concerns. A great deal of ROSAT data is publicly available over the internet; using this, together with improved temperature measurements from the ASCA satellite, we sought to construct models of the 4 clusters measured by Myers et al. and Herbig et al., as well as 18 other clusters from an x-ray flux-limited sample based on the XBAC catalog (Ebeling et al. 1996). In order to address the issue of radio calibration, we undertook absolute flux density measurements of the supernova remnant Cas A with the OVRO 1.5-meter telescope system. Finally, three seasons of OVRO 5.5-m observations were conducted to extend the coverage of the sample.

1.2 Cosmology and Distance Measures

Modern cosmology has its origins in Edwin Hubble's discovery (Hubble & Humason 1931) of the redshift-distance relationship. Using Cepheid variables as a standard candle together with spectroscopic observations of galaxies, he found that the apparent recessional velocity[2], v, of a galaxy was related to its distance, d, by

$$v = H_0\, d, \tag{1.6}$$

where H_0 is the Hubble constant, typically expressed in units of $\mathrm{km\,sec^{-1}}$ $\mathrm{Mpc^{-1}}$. Such a relationship occurs naturally in the context of General Relativity. The simplest cosmological solutions to Einstein's field equations are not static, but imply a space-time metric which changes as a function of time. Under the assumptions of isotropy and homogeneity, we find that the time-dependence of the metric is contained in a single factor $R(t)$ which cor-

[2]The redshift, z, is defined as v/c.

responds to an overall expansion or contraction of space (see, e.g. Weinberg 1972; Schutz 1985). It can then be shown that for small values of d, the constant H_0 in Eq. 1.6 is simply

$$H(t_0) \equiv H_0 = \frac{\dot{R}(t_0)}{R(t_0)}. \tag{1.7}$$

Throughout this discussion we denote the present time by t_0, and the current values of dynamical variables by H_0 , R_0 , etc. The Friedmann equation governs the dynamical evolution of R:

$$H^2(t) = \frac{8\pi G}{3}\rho(t) - \frac{k}{R^2(t)}. \tag{1.8}$$

Here ρ is the energy density of the universe at time t and k is a constant governing the overall geometry of the universe; this constant can always be chosen to be $+1$, 0 , or -1, corresponding to closed, flat, and open geometries respectively. The energy density ρ contains contributions from all existing components of the universe (baryons, other matter, photons, vacuum energy, etc.). From this perspective two of the major tasks of cosmology are to determine the *form* of this equation (by inventorying the components of ρ and determining the sign of k) and to determine the values of R_0 and H_0 (i.e., the current state of the dynamical variables). This will allow us to understand the age, origin, and fate of the universe as a whole.

From a more concrete point of view, a measurement of H_0 sets the distance scale of the universe. This is due to the fact that the most direct and routinely used method of obtaining distances is to measure a spectroscopic redshift (or a recessional velocity v); any distances measured by this method automatically contain an uncertainty due to our imperfect knowledge of H_0. An accurate measurement of H_0 would therefore have implications for a wide variety of astrophysical and cosmological problems.

There are two general classes of methods used to measure the distance scale: direct and indirect methods. Indirect methods are based on a series of distance measures, each valid only over a limited range of distances, which together are used to reach into the regime where the expansion of the universe (or Hubble flow) dominates over the random motions of individual objects. For expected galaxy peculiar velocities of $\lesssim 1000\,\mathrm{km\,sec^{-1}\,Mpc^{-1}}$, this corresponds to $z \sim 0.02$ or $60\,h^{-1}$ Mpc. A sequence of distance measures which together are used to reach these distances are referred to as a distance ladder. Cepheid variable stars form the basis of most such ladders. These are periodic variable stars whose absolute luminosity is related to the period of their optical pulsations. The period-luminosity (P-L) relationship must be calibrated by means of some independent method, such as parallax measurements of nearby Cepheids or statistical parallax methods applied to stellar clusters containing Cepheids. The Hubble Space Telescope (HST) has enabled Cepheid variables to be observed to greater distances ($\sim$ 20 Mpc) than was previously possible from the ground. Even at this distance galaxy peculiar velocities are important, and to obtain a secure measurement of H_0 secondary distance indicators must be calibrated using the Cepheids. With Cepheids plus a set of secondary distance indicators (such as Tully Fisher and SN Ia's), the HST Key project on the extragalactic distance scale has recently determined $H_0 = 72\,(\pm 5)_{rand}\,(\pm 7)_{sys}\,\mathrm{km\,sec^{-1}\,Mpc^{-1}}$ (Madore et al. 1999). In an independent program (using, however, the HST Cepheid distances) Riess et al. (1998) find $H_0 = 64 \pm 7\,\mathrm{km\,sec^{-1}\,Mpc^{-1}}$;Sandage et al. (1996) have measured H_0 in an independent program, using Cepheids to calibrate 7 SN Ia's, obtaining $H_0 = 56 \pm 4\,\mathrm{km\,sec^{-1}\,Mpc^{-1}}$ (presumably including systematic errors). The origin of this discrepancy is not clear. The HST Key project Cepheid distances are based on a P-L relation which is calibrated from Cepheids in the Large Magellenic Cloud (LMC). For this calibration a distance modulus of $\mu_{LMC} = 18.50 \pm 0.15$ is used (Madore & Freedman 1998), corresponding to a distance to the LMC of 50.1 kpc. This scale is somewhat controversial, however, and should probably be regarded as uncertain at about the 10% level (see, e.g., Stanek et al. 1998, and references therein). This highlights one of the difficulties with indirect methods: the cosmic distance which is ultimately determined depends upon systematic and random errors at *each* step of the distance ladder.

Direct methods, in contrast, permit measurements (without the use of intermediate indicators) at distances great enough that the Hubble flow dominates the observed redshift. One such method, as indicated previously, is the combination of SZ and x-ray measurements in galaxy clusters. Aside from the results of Herbig et al. and Myers et al. discussed earlier, most SZ cluster observations have targeted more distant clusters. For these clusters projection effects are more of a concern, and due to the reduced signal-to-noise, the x-ray models are of lower quality. By applying this method to A665 and A2218, Birkinshaw & Hughes (1994) find a value of $H_0 = 55 \pm 17\,\mathrm{km\,sec^{-1}\,Mpc^{-1}}$. Time delays in gravitational lens systems provide another direct probe of the cosmic distance scale, since the time delay between two paths is proportional to the path length, which itself is proportional to H_0^{-1}. This method has been used with success on the lens systems 0957+561 (Kundic et al. 1997), B0218+357 (Biggs et al. 1999) , and 1608+656 (Fassnacht 1999); these measurements yield $H_0 = 64 \pm 13\,\mathrm{km\,sec^{-1}\,Mpc^{-1}}$ (95% confidence, including modeling uncertainties), $H_0 = 69^{+13}_{-19}\,\mathrm{km\,sec^{-1}\,Mpc^{-1}}$ (95% confidence, with a preliminary mass model), and $H_0 = (59^{+6}_{-5} \pm 15)\,\mathrm{km\,sec^{-1}\,Mpc^{-1}}$ (95% confidence random and 68% modeling errors) respectively. Fluctuations of the optical or infra-red surface brightness of galaxies provide another (in principle) direct distance measure (Tonry & Schneider 1988); this has been applied to several nearby clusters (e.g. Thomsen et al. 1997; Jensen et al. 1999). Another promising technique which has emerged recently is that of high-redshift water maser proper motion studies (Herrnstein 1999).

Overall, a number of reliable direct and indirect methods of determining the cosmic distance scale are in practice. From our informal survey of these, it is apparent that most of them are consistent to within their estimated error bars, and fall in the range of $55 - 75\,\mathrm{km\,sec^{-1}\,Mpc^{-1}}$. This in itself represents good progress in the field; nevertheless, it would be highly desirable to have a more accurate measurement of H_0. In order to achieve this it is important to understand and reduce the systematic errors associated with all of the methods, and eventually to have a number of independent methods which agree at the desired level of accuracy. As indicated in the previous section, the reduction of systematic errors in the SZ plus x-ray determination of H_0 is the primary impetus for this thesis.

1.3 An Overview of the Thesis

The goal of this thesis is to obtain an accurate measurement of the Hubble constant using measurements of the SZE on the OVRO 5.5-meter (including the results of Myers et al. as well as new data); the principle focus of our efforts will be better x-ray models and an improved radio calibration. Chapter 2 reviews the basic theory of thermal bremsstrahlung and the SZE , as well as discussing the modeling strategies we adopt and the potential impact of cooling-flow emission and multi-phase structure on our predictions. In Chapter 3 we present an expanded cluster sample, catalog the public ROSAT data upon 22 members of this sample, and summarize other data (redshifts and electron temperatures) from the literature on these 22 clusters. Chapter 4 details the procedures employed in the analysis of ROSAT data, presents the results of a detailed study of the effects of the uncertainties in the resulting density profile on our SZE predictions, and gives baryonic and total mass models for these 22 clusters. The surface brightness images and x-ray profiles resulting from this analysis are presented in Appendix A, and the best-fit `XSPEC` plasma models are presented in Appendix B. In Chapter 5 we discuss the 1.5-meter absolute calibration measurements, which result in an absolute flux density for Cas A accurate to $\sim 3\%$. Results on a set of secondary sources with somewhat lower accuracy are also given. Chapter 6 presents the results of recent SZE observations at the Owens Valley, in addition to summarizing the results of Myers et al. and Herbig et al. as referenced onto the current flux density and instrument calibration. In this chapter we also discuss the interpretation of these observations and, together with the x-ray models of Chapters 3 and 4, obtain a highly accurate measurement of H_0. In Chapter 7 we summarize our findings, discuss the wider implications, and indicate some fruitful directions for future work in the field.

Chapter 2

Radiative Processes In Clusters

2.1 Theory of Thermal Bremsstrahlung

The total or bolometric luminosity due to thermal bremsstrahlung emission from an ionized thermal plasma of electrons and protons is (Rybicki & Lightman 1979)

$$L = W \times \int_{ICM} n_e n_p T^{1/2} \overline{g} dV, \tag{2.1}$$

where

$$W = \left(\frac{2\pi k_B}{3m_e} \right)^{1/2} \times \frac{2^5 \pi e^6}{3hm_e c^3}, \tag{2.2}$$

n_e is the electron number density, n_p is the proton number density, k_B is Boltzmann's constant, T is the local temperature of the plasma, and $\overline{g}$ is the thermally averaged Gaunt factor. The quantity $\overline{g}$ is typically of order unity, and expressions for it are given by Rybicki & Lightman (1979). If the plasma is isothermal, as we will assume for the rest of the discussion, g and T may be factored out of the integral. For a plasma with the cosmic helium mass fraction $Y = 0.24$, $n_p/n_e = 0.862$; this is the value we adopt. For a uniform, isothermal plasma occupying a volume V, we find

$$\begin{aligned} L \;=\;& 4.3 \times 10^{44} \,\mathrm{erg\,s^{-1}} \times \\ & \frac{n_p/n_e}{0.862} \left(\frac{n_e}{10^{-3}\,\mathrm{cm^{-3}}} \right)^2 \left(\frac{T_e}{10\,\mathrm{keV}} \right)^{1/2} \frac{\overline{g}}{1.2} \frac{V}{1\,\mathrm{Mpc}^3}. \end{aligned} \tag{2.3}$$

The total flux observed from the plasma, assumed to be at a redshift z, is

$$S = \frac{W\overline{g}T^{1/2}}{4\pi D_L^2(z)} \times \int n_e^2 dV. \tag{2.4}$$

Here D_L is the luminosity distance. In this case, the emission measure EM (or the emission integral EI), is usually defined:

$$EM = \int n_e^2 dV. \tag{2.5}$$

If the electrons are spherically distributed according to

$$n_e(r) = n_{eo} \times (1 + \frac{r}{r_o})^{-\frac{3\beta}{2}} \tag{2.6}$$

then the EM over all space is

$$EM = \pi^{\frac{3}{2}} r_o^3 n_o^2 \frac{\Gamma(3\beta - 3/2)}{\Gamma(3\beta)} \tag{2.7}$$

and for an observed total flux S we may obtain the central electron density (see Appendix C):

$$n_{eo} = \sqrt{\frac{4}{\pi^{1/2}} \frac{\Gamma(3\beta)}{\Gamma(3\beta - \frac{3}{2})} \frac{1}{r_o^3} \frac{S D_L^2}{W\overline{g}T^{1/2}}}. \tag{2.8}$$

Using the fact that the luminosity distance is related to the angular diameter distance by $D_L = D_A \times (1+z)^2$, we can express this in terms of the observed core radius of the cluster θ_o,

$$n_{eo} = \sqrt{\frac{4}{\pi^{1/2}} \frac{\Gamma(3\beta)}{\Gamma(3\beta - \frac{3}{2})} \frac{1}{\theta_o^3} \frac{(1+z)^6}{D_L} \frac{S}{W\overline{g}T^{1/2}}}. \tag{2.9}$$

Thus if the temperature T, the bolometric flux S, the redshift, and the profile parameters θ_o,β are known, the electron density is determined. This equation also illustrates the $h^{\frac{1}{2}}$ dependence of the derived electron density. Since the x-ray emission is strongly peaked and the $\beta-$ model is typically a good description of the observed profiles out to moderate radii, the result obtained for the density is not highly sensitive to the assumed form of the plasma profile so long as the profile fits the data reasonably well.

In practice there are several complications to this simple picture, the most significant of which is that all observations are obtained over a finite band with a finite energy resolution. Real plasmas also contain species heavier than hydrogen which give rise to line features as well as making contributions to the bremsstrahlung continuum; many observations are attenuated by photoionization due to neutral hydrogen along the line of sight, which distorts the observed spectrum. This necessitates fitting the observed spectra to detailed plasma models convolved with the instrumental response function, a task which is implemented in several publicly available software packages. We chose to use `XSPEC`, NASA GSFC's standard x-ray spectral analysis program. The x-ray spectrum of a typical cluster is shown in Figure 2.1. At low energies, the spectrum rolls off due to photo-absorption, while at high energies the exponential slope characteristic of thermal bremsstrahlung can be seen.

We now turn our attention to the issue of relating the quantity reported by `XSPEC` (a spectrum normalization, K) to the quantity of physical interest, the electron density n_e, for spectra extracted from a finite aperture. The `XSPEC` model of choice for modeling the ICM in clusters is "raymond", an implementation of the Raymond-Smith plasma models (Raymond & Smith 1977). The normalization of the model spectrum (proportional to the total flux over the observation band) is reported as the parameter K, defined as

$$K = \frac{10^{-14}}{4\pi D_L^2} \int n_e \, n_p \, dV. \tag{2.10}$$

Here all distances are in cm, and n_p is the number density of protons. We can re-express the EM as

$$\int n_e n_p dV = \int dA \int_{-\infty}^{+\infty} dz \, n_e \, n_p, \tag{2.11}$$

where the area integral is over the plane parallel to the image plane, and the z integral is along the line of sight. For an observation with a finite aperture, the integral over dA will be truncated. We assume a circular aperture with an inner radius θ_1 and an outer radius θ_2. The resulting integral yields (Appendix C):

$$\int dA \int_{-\infty}^{+\infty} dz \, n_e \, n_p = n_{eo}^2 D_A^3 \theta_o^3 \sqrt{\pi} \frac{\Gamma(3\beta - 1/2)}{\Gamma(3\beta)} \times \frac{2\pi}{3(2\beta - 1)} \left(C(\theta_1) - C(\theta_2)\right) \tag{2.12}$$

where

$$C(\theta) = \left[1 + (\frac{\theta}{\theta_o})^2\right]^{-3\beta + 3/2}. \tag{2.13}$$

Combining Equations 2.10 and 2.12, and using (Weinberg 1972)

$$D_L = 6000\,h^{-1}\,\left[(1+z) - \sqrt{1+z}\right]\,\mathrm{Mpc} \tag{2.14}$$

(valid for $q_o = 0.5$), we find for the central electron density

$$\begin{aligned} n_{eo} \;=\;& 4.160\times 10^{-3}\,\mathrm{cm}^{-3}\,h^{1/2}\,\times \qquad (2.15)\\ & \left[\frac{n_e/n_p}{1.16}\,(\beta-1/2)\,\theta_o^{-3}\,\frac{(1+z)^6}{1+z-\sqrt{1+z}}\,\frac{\Gamma(3\beta)}{\Gamma(3\beta-1/2)}\,\frac{K/10^{-2}}{C(\theta_1)-C(\theta_2)}\right]^{\frac{1}{2}} \end{aligned}$$

where θ_0 here is in arcminutes. Note that Equation 2.15 uses the *total* observed x-ray flux and the observed x-ray profile to derive a central density. An analogous relation using the central surface brightness to estimate the central density has found some use in the literature (e.g. Briel et al. 1992). While not likely to be systematically in error, these latter methods will be more affected by Poisson noise, uncertainties in the form of the profile, and cooling flow emission than will Eq. 2.15.

Given a model for the distribution of baryons in the cluster, it is straightforward to calculate the baryonic mass within a specified radius. For a $\beta-$ model, the answer is[1]

$$M_{bary}(<R) = \frac{4}{3}\pi r_o^3 \rho_B \left(\frac{R}{r_o}\right)^3 {}_2F_1\left(\frac{3}{2}, \frac{3\beta}{2}, \frac{5}{2}, -(\frac{R}{r_o})^2\right) \tag{2.16}$$

where ρ_B is the baryonic mass density

$$\rho_B = n_e\,m_p \times \mu_e. \tag{2.17}$$

Here m_p is the proton mass and μ_e is the baryon to electron ratio. For a fully ionized plasma with an overall metal abundance of f relative to solar, and individual element number abundances A_i relative to hydrogen, this is

$$\mu_e = \frac{1 + 4A_2 + f\,\sum_{i>2} A_i\,\frac{m_i}{m_p}}{1 + 2A_2 + f\,\sum_{i>2} A_i\,i}. \tag{2.18}$$

[1]The Numerical Recipes (Press et al. 1992) algorithm for ${}_2F_1$ is sometimes somewhat unstable in the regime of interest. Adding an imaginary part of order 10^{-3} to the final argument eliminates this instability without affecting the result at greater than the 0.1% level.

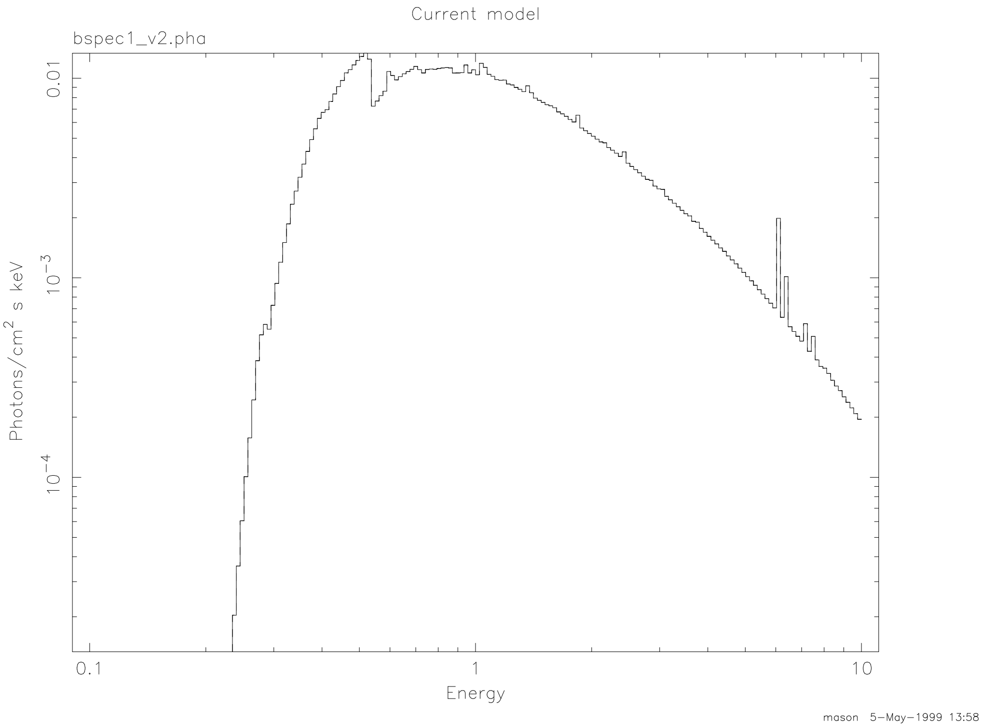

Figure 2.1: The observed x-ray flux (0.1-10 keV) for a Raymond-Smith plasma having a temperature of 7 keV, a metal abundance of 30% solar, and an absorbing hydrogen column density of $1.0 \times 10^{21}\mathrm{cm}^{-2}$. The $0.5 - 2.0$ keV luminosity of this cluster is $\sim 1.4 \times 10^{44}\, h^{-2}$ ergs/sec, and it is assumed to be at a redshift of 0.07.

Assuming the cosmic Helium abundance, solar metal abundances of Anders & Grevesse (1989), and an overall abundance $f = 30\%$, we calculate $\mu_e = 1.142$. We can also compute the total baryonic mass within a projected radius ρ; the result is

$$M_{bary}(<\rho) = \rho_B\, r_o^3 \sqrt{\pi}\, \frac{\Gamma(3\beta/2 - 1/2)}{\Gamma(3\beta/2)} \times \frac{2\pi}{3(1-\beta)} \times \left((1 + (\frac{\rho}{r_o})^2)^{\frac{3}{2}(1-\beta)} - 1 \right) \tag{2.19}$$

Under the assumption of hydrostatic equilibrium, and with knowledge of the gas temperature profile, the total mass profile of the cluster may be inferred. We find

$$-\rho_B(r) G \frac{M(r)}{r^2} = \frac{k_B}{\mu m_p} \frac{d}{dr}(\rho(r) T(r)). \tag{2.20}$$

or

$$M(<r) = -\frac{kT(r)}{G\mu m_p} \times r \times \left(\frac{\partial \ln n_e}{\partial \ln r} + \frac{\partial \ln T}{\partial \ln r} \right) \tag{2.21}$$

Here $M(r)$ is the total mass enclosed within a radius r, and μ is the mean molecular mass in units of the proton mass. For a fully ionized plasma with an overall metal abundance of f relative to solar, and individual element number abundances A_i relative to hydrogen, we have for μ

$$\mu = \frac{1 + 4A_2 + f\, \sum_{i>2} A_i\, \frac{m_i}{m_p}}{2 + 3A_2 + f\, \sum_{i>2} A_i\,(i+1)}. \tag{2.22}$$

Using the same prescription as before, we find $\mu = 0.592$.

If we assume that the gas follows a beta-model, then we have

$$\frac{\partial \ln n_e}{\partial \ln r} = -3\beta \frac{r^2/r_o^2}{1 + r^2/r_o^2} \tag{2.23}$$

and

$$\begin{aligned} M(<r) &= 3.70 \times 10^{13}\, \mathrm{M}_\odot \times \frac{T(r)}{\mathrm{keV}} \frac{r}{\mathrm{Mpc}} \frac{0.60}{\mu} \times \\ & \left(3\beta \frac{r^2/r_o^2}{1 + r^2/r_o^2} - \frac{\partial \ln T}{\partial \ln r} \right). \end{aligned} \tag{2.24}$$

Several properties of this relationship are worthy of note. First, the mass calculated at any given radius depends *only* upon the density gradient and temperature at that radius. We will find this to be important in our profile analysis (Chapter 4). Secondly, the possible presence of temperature gradients at large radii may have a significant affect upon the inferred total mass at these radii. This issue will also be addressed in Chapter 4.

With this formalism in hand, we may note some interesting general properties of the radial behavior of the baryon fraction under an isothermal β model. At small radii, the baryon fraction is seen to rise sharply out to a couple of core radii, after which it flattens. For models with $\beta < 2/3$, the baryon fraction continues to rise out to arbitrarily large radius. For models with $\beta > 2/3$, the baryon fraction falls at large radius after the initial rise; and for models with $\beta = 2/3$, it is constant. Departures from isothermality at large radius will tend to make the baryon fraction profile fall more rapidly, as will steepening of the density profiles at large radius. These properties follow directly from the assumption of hydrostatic equilibrium as applied to the isothermal β model. The constancy of the baryon fraction for $\beta = 2/3$ may be understood from the standpoint that in this special case the baryons and the dark matter are both assuming a singular isothermal sphere $(1/r^2)$ profile. Figure 2.2 shows the baryon fraction as a function of radius for three density profiles with fixed x-ray emission measures within a $1.5\,h^{-1}$ Mpc projected radius.

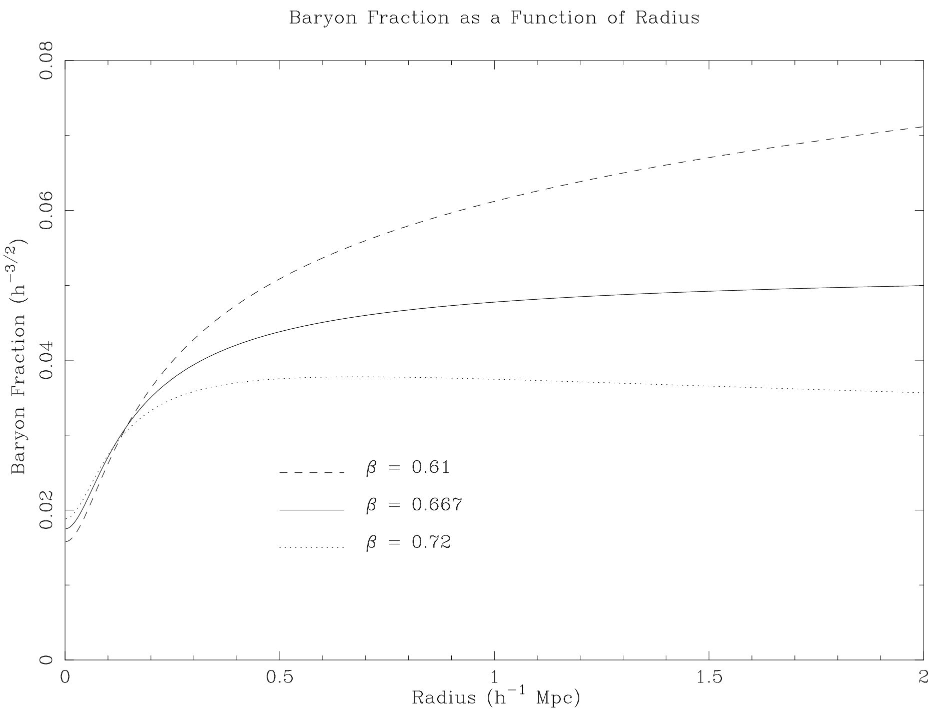

Figure 2.2: Baryon Fraction as a function of radius for three different models, illustrating how the asymptotic behavior depends on β. The central density of each model was floated to yield a fixed x-ray emission measure within a $1.5\,h^{-1}$ Mpc projected radius. For this model a core of 200 h^{-1} kpc was assumed.

2.2 ICM Models

One model for the cluster gas which has enjoyed great phenomenological success is the *isothermal beta model* (Cavaliere & Fusco-Femiano 1976). In this case, the gas is assumed to be isothermal, and the electrons distributed according to

$$n_e(r) = n_{eo}\left(1 + r^2/R_0^2\right)^{-3\beta/2}. \tag{2.25}$$

Here n_{eo} is the central electron number density, r is the spherical metric radius, and R_0 is a characteristic scale. This is the form we first introduced in Equation 2.6. Numerous properties of this model, including the x-ray surface brightness profiles and surface mass densities which result from it, are summarized in Appendix C.

One generalization of the isothermal β model which has some support both observationally and theoretically is the class of hybrid isothermal/adiabatic ICM models. In these models, the cluster gas is assumed to follow the same form as in Eq. 2.25. The temperature is taken to be isothermal inside some radius (typically $\sim 500\,h^{-1}\,\mathrm{kpc}$), outside of which it follows an adiabatic equation of state, declining as

$$T_e(r) \propto n_e(r)^{\gamma-1}. \tag{2.26}$$

In this case, the cluster temperature profile is

$$T_e(r) = \begin{cases} T_{eo} & r < r_{iso} \\ T_{eo} \times \left(n_e(r)/n_e(r_{iso})\right)^{\gamma-1} & r > r_{iso} \end{cases} \tag{2.27}$$

Hughes et al. (1988a,b) have found that this model provides a substantially better fit to TENMA and EXOSAT data on Coma than pure adiabatic or isothermal models. They find best-fit parameters of $\gamma \sim 1.6$ and $r_{iso} \sim 0.5\,h^{-1}\,\mathrm{Mpc}$. Navarro et al. (1995) have seen similar temperature profiles in numerical simulations of clusters.

Markevitch et al. (1998) have found some indications from ASCA data that for many clusters the temperature profile follows an adiabatic profile (Eq. 2.26) with $\gamma \sim 1.2$ even well into the core. Spatially resolved spectroscopy of extended sources with the ASCA satellite is a tricky business, however, and the results will in general be corrupted by any errors in the characterization of the energy-dependent ASCA point-spread function. Until these results are confirmed by, e.g., Chandra or XMM, we do not consider this class of models; if they were to be borne out by further x-ray observations, they could lower our SZE predictions by 25% or more. We note, however, that an independent analysis by Irwin et al. (1999) using a "color ratio" approach with ROSAT data does not confirm the Markevitch et al. profile results. This question will be conclusively resolved by near-future x-ray observations.

2.3 Predicting the SZE

Given a temperature and a model for the spatial distribution of electrons in a cosmic plasma, it is straightforward to predict the change in the intensity of the CMB which will be observed due to inverse Compton scattering. We discuss both the basic theory and the formalism for applying this to observations with single-dish radio telescopes.

2.3.1 Fundamentals

Since the original work of Sunyaev & Zeldovich (1970) and Sunyaev & Zeldovich (1980), much effort has gone into understanding the SZE more thoroughly; see, e.g., Rephaeli (1995), Challinor & Lasenby (1998), Itoh et al. (1998), and Sazonov & Sunyaev (1998). This work has concentrated on determining the relativistic corrections to the original expressions of Sunyaev & Zeldovich (1970) and Sunyaev & Zeldovich (1980), as well as understanding the limitations of the diffusion approximation used to derive the Kompaneets equation. The most recent and definitive work is that of Sazonov & Sunyaev (1998), who have derived analytic expressions for the total fractional change in the CMB intensity due to inverse Compton scattering; their calculations encompass both the thermal and kinematic effects along with relativistic corrections to each. They find

$$\begin{aligned} \frac{\Delta I_\nu}{I_\nu} &= \tau \frac{x e^x}{e^x - 1} \times \left[\frac{kT_e}{m_e c^2} f_1(x) + \left(\frac{kT_e}{m_e c^2}\right)^2 f_2(x) + \right. \\ &\left. \frac{v}{c}\mu + \left(\frac{v}{c}\right)^2 f_3(x,\mu) + \frac{kT_e}{m_e c^2}\frac{v}{c}\mu f_4(x) \right], \end{aligned} \tag{2.28}$$

where

$$f_1(x) = x \coth(x/2) - 4, \tag{2.29}$$

$$f_2(x) = -10 + \frac{47}{2}x\coth(x/2) - \frac{42}{5}x^2\coth^2(x/2) + \frac{7}{10}x^3\coth^3(x/2) + \frac{7}{5}\frac{x^2}{\sinh^2(x/2)}(x\coth(x/2) - 3), \quad (2.30)$$

$$f_3(x,\mu) = -(1+\mu^2) + \frac{3+11\mu^2}{20}x\coth(x/2), \quad (2.31)$$

and

$$f_4(x) = 10 - \frac{47}{5}x\coth(x/2) + \frac{7}{10}x^2\left(2\coth^2(x/2) + \frac{1}{\sinh^2(x/2)}\right). \quad (2.32)$$

We have defined

$$x = \frac{h\nu}{kT_{cmb}} \quad (2.33)$$

and μ, which is the cosine of the angle of the cluster velocity to the line of sight ($\mu = +1$ for a cluster moving *towards* the observer). The optical depth τ is given by

$$\tau = \sigma_T \int dz\, n_e \quad (2.34)$$

where σ_T is the Thompson-scattering cross-section ($6.65 \times 10^{-25}\mathrm{cm}^2$) and n_e is the electron number density. As a measure of the magnitude of the thermal SZE, it is conventional to define the Compton y-parameter:

$$y = \frac{kT_e}{m_e c^2} \times \tau. \quad (2.35)$$

In Equation 2.28, the first term corresponds to the thermal SZE; the second, to the relativistic corrections to the thermal SZE; the third to the kinematic effect; the fourth to relativistic corrections to the kinematic effect. The last term is a cross term between the kinematic and thermal effects. The last two terms are newly discovered by Sazonov & Sunyaev (1998); the expression given for the correction to the thermal effect is in agreement with those derived in the Fokker-Planck approximation by Itoh et al. (1998) and Challinor & Lasenby (1998). While all of these calculations for the thermal corrections employed the diffusion approximation, they are in reasonable ($\sim 0.6\%$) agreement with the numerical results of Rephaeli (1995), which do not. Sazonov and Sunyaev have performed similar numerical calculations, and they find that the analytic expressions overall are good to better than 2% out to the far Wien regime for clusters with $T_e < 20$ keV and $v < 3000\,\mathrm{km\,sec^{-1}}$. In the far Wien regime, some caution may be indicated in using these expressions. In this limit the assumption that the spectrum is slowly varying, used to justify the diffusion approximation common to all of the analytic results, is violated.

Note that the leading term in the kinematic effect can be a source of noise in thermal SZE measurements at the $\sim 5\%$ level for typical clusters. Since this term is proportional to μ, however, it will average out when the thermal effect is measured in a sample of clusters. It is also possible to measure and remove the contribution of the kinematic effect using high-frequency SZ measurements. The relativistic correction to the kinematic effect, on the other hand, depends only on μ^2, and hence is a potential source of bias to any measurements which do not account for the cluster peculiar velocity. Fortunately this is a 0.1% effect or less compared to the thermal SZE at low frequencies. Therefore we will set $v = 0$ for the remainder of the discussion.

The spectral intensity of the CMB is given by

$$I_\nu = \frac{2kT_{cmb}}{\lambda^2} \times \frac{x}{e^x - 1}; \tag{2.36}$$

at 30 GHz and using $T_{cmb} = 2.728 \pm 0.004\,\mathrm{K}$ (95%) (Fixsen et al. 1996) this yields an intensity of $57.1\,\frac{\mathrm{MJy}}{\mathrm{Sr}}$. Using Eq. 2.36, the total intensity change due to the thermal SZE may then be written

$$\Delta I_\nu = y \times \frac{2kT_{cmb}}{\lambda^2} \times \frac{x^2 e^x}{(e^x - 1)^2} \left(f_1(x) + \frac{kT_e}{m_e c^2} f_2(x) \right). \tag{2.37}$$

The proportionality between the total decrement in specific intensity and the Compton y parameter is plotted in Figure 2.3 for the non-relativistic case and for a 10 keV plasma including relativistic corrections. Also indicated in this figure are our observing frequency of 32 GHz and the non-relativistic null in the SZE at 218 GHz.

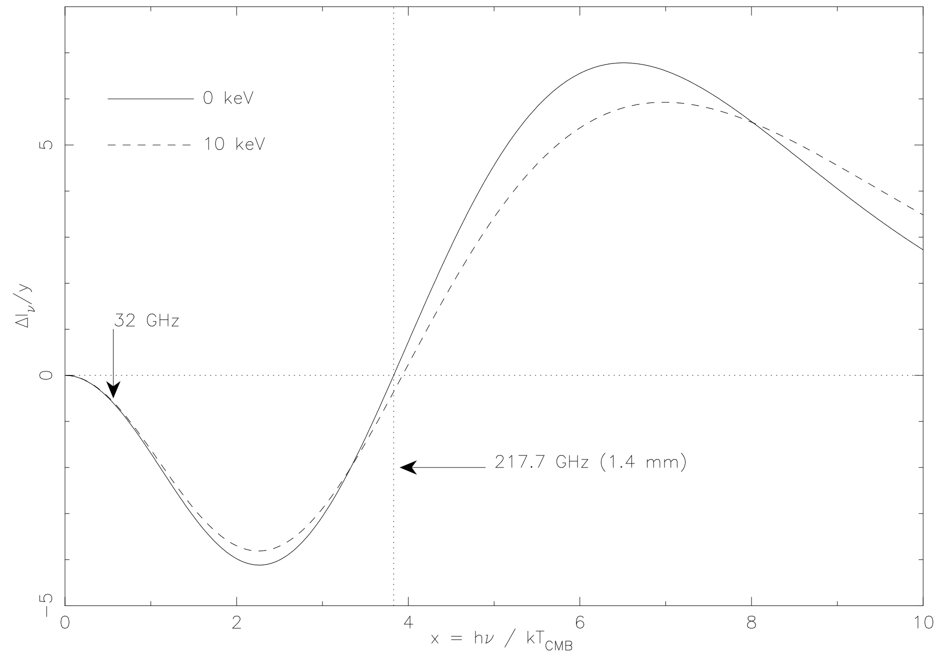

Figure 2.3: The proportionality between the total decrement in specific intensity due to the SZE and the Compton y parameter. The units on the y-axis are arbitrary.

2.3.2 Observing the SZE with a Single Dish

A single-dish radio telescope measures power differences in units of the *antenna temperature* T_A, defined as

$$\Delta T_A = \frac{\Delta P_\nu}{k_B} \tag{2.38}$$

where P_ν is the spectral power (power per unit frequency) the telescope is receiving and k_B is Boltzmann's constant. If this telescope has an effective area A_{eff} and is looking at a specific intensity distribution $\Delta I_\nu(\hat{\Omega})$, the observed spectral power will be

$$\Delta P_\nu = \frac{1}{2} A_{eff} \int d\Omega \, \Delta I_\nu(\hat{\Omega}) \, R_N(\hat{\Omega}). \tag{2.39}$$

For a source with a specific intensity given by Eq. 2.37, we have

$$\begin{aligned} \Delta P_\nu &= \frac{2kT_{cmb}}{\lambda^2} \times \frac{x^2 e^x}{(e^x - 1)^2} \left(f_1(x) + \frac{kT_e}{m_e c^2} f_2(x) \right) && (2.40) \\ &\quad \times \frac{1}{2} A_{eff} \int d\Omega \, y(\hat{\Omega}) \, R_N(\hat{\Omega}). && (2.41) \end{aligned}$$

Here $R_N(\hat{\Omega})$ is the telescope response function normalized to unity at the maximum. It can be shown (e.g. Rohlfs & Wilson 1996) that the telescope effective area A_{eff} is related to the total solid angle of the beam pattern Ω_A by $\Omega_A A_{eff} = \lambda^2$. Then

$$\begin{aligned} \Delta P_\nu &= kT_{cmb} \times \frac{x^2 e^x}{(e^x - 1)^2} \left(f_1(x) + \frac{kT_e}{m_e c^2} f_2(x) \right) && (2.42) \\ &\quad \times \frac{1}{\Omega_A} \int d\Omega \, y(\hat{\Omega}) \, R_N(\hat{\Omega}). && (2.43) \end{aligned}$$

Using Eq. 2.38, we obtain

$$\begin{aligned} \Delta T_A &= T_{cmb} \times \frac{x^2 e^x}{(e^x - 1)^2} \left(f_1(x) + \frac{kT_e}{m_e c^2} f_2(x) \right) && (2.44) \\ &\quad \times \frac{1}{\Omega_A} \int d\Omega \, y(\hat{\Omega}) \, R_N(\hat{\Omega}). && (2.45) \end{aligned}$$

This is the antenna temperature difference that our single-dish radio telescope observes from the thermal SZ source characterized by $y(\hat{\Omega})$.

Since most sources do not fill the entire beam of the telescope, it is conventional to reference the measured antenna temperatures onto the main beam of the telescope. To this end, we define an *equivalent brightness temperature*, T_{eq}, as

$$\Delta T_{eq} = \frac{\Omega_{Ant}}{\Omega_{Beam}} \times T_A. \tag{2.46}$$

Here Ω_{Beam} is the volume of the primary beam of the telescope, usually determined from beam maps of point sources. The equivalent brightness temperature for the case we are considering is then given by Eq. 2.44 with $\Omega_{Ant} \to \Omega_{Beam}$. Since in Eq. 2.44 everything before the integral (aside from the relativistic correction) is independent of the observing geometry and the target of observation, it is convenient to define a beam-averaged y-factor:

$$y_{Beam} = \frac{1}{\Omega_{Beam}} \int d\Omega \, y(\hat{\Omega}) \, R_N(\hat{\Omega}). \tag{2.47}$$

Then we have

$$\Delta T_{eq} = T_{cmb} \times \frac{x^2 e^x}{(e^x - 1)^2} \left(f_1(x) + \frac{kT_e}{m_e c^2} f_2(x) \right) \times y_{Beam} \tag{2.48}$$

At 32 GHz ($x = 0.563$), this is (neglecting the relativistic correction):

$$\Delta T_{eq} = -1.897 \times y \times T_{cmb}. \tag{2.49}$$

The proportionality between the observed antenna temperature and the beam-averaged Compton y parameter is shown in Figure 2.4 for a non-relativistic plasma and for a plasma at 10 keV including the relativistic correction.

Realistically, some signal ($\sim 5 - 10\%$) is removed by the beam-switching, and it is necessary to consider to consider the effects of this switching. In this case we simply define the switched y-factor

$$y_{sw} = \frac{1}{\Omega_{Beam}} \int d\Omega \, y(\hat{\Omega}) \, R_{N,sw}(\hat{\Omega}) \tag{2.50}$$

where $R_{N,sw}(\hat{\Omega})$ is the difference of the two individual normalized response patterns for either beam. The observed equivalent brightness temperature including the effects of switching is then given by Eq. 2.48 with $y_{Beam} \to y_{sw}$. For most instruments the main beam is fairly well described by a Gaussian so

$$R_N(\hat{\Omega}) = e^{-\theta^2/2\sigma^2} \tag{2.51}$$

and

$$\Omega_{Beam} = 2\pi\sigma^2. \tag{2.52}$$

In analogy with Eqs. 2.47 and 2.50, we may define the beam averaged (and fully switched) optical depths:

$$\tau_{beam} = \frac{1}{\Omega_{Beam}} \int d\Omega\, \tau(\hat{\Omega})\, R_N(\hat{\Omega}) \tag{2.53}$$

and

$$\tau_{sw} = \frac{1}{\Omega_{Beam}} \int d\Omega\, \tau(\hat{\Omega})\, R_{N,sw}(\hat{\Omega}). \tag{2.54}$$

This will prove useful for the cluster modeling since the ROSAT data naturally produce density models.

Thermal SZE predictions which have been made without accounting for relativistic affects can be corrected by dividing by the factor

$$\chi_{Rel} = \left(1 + \frac{kT_e}{m_e c^2} \frac{f_2(x)}{f_1(x)}\right)^{-1}. \tag{2.55}$$

This correction is typically $\sim 3\%$ at 32 GHz. This is the same definition of χ_{rel} given by Myers et al. (1997). The overall result of the relativistic correction is to make the predicted decrement slightly smaller than it would be otherwise. In practice, consistent with the convention of Myers et al., we will not include χ_{rel} in the model prediction, but will apply it as a (multiplicative) correction factor to the observed decrement. This is the correct prescription to follow in order for y_{obs} to remain interpretable as a Compton y-parameter as usually defined (Eq. 2.35). In the end, the SZE decrement we predict at 32.0 GHz is

$$\Delta T_{eq,sw} = -1.897\, \chi_{rel}^{-1} \times T_{cmb} \times \frac{kT_e}{m_e c^2}\, \tau_{sw} \tag{2.56}$$

or equivalently

$$\Delta T_{eq,sw} = -1.897\, \chi_{rel}^{-1} \times T_{cmb} \times y_{sw}. \tag{2.57}$$

It is also useful to define several quantities which measure the efficiency of a given observing strategy. We define the overall efficiency η_{obs} as the ratio of the observed Compton y to the peak (central) y:

$$\eta_{obs} = \frac{y_{sw}}{y_o}. \tag{2.58}$$

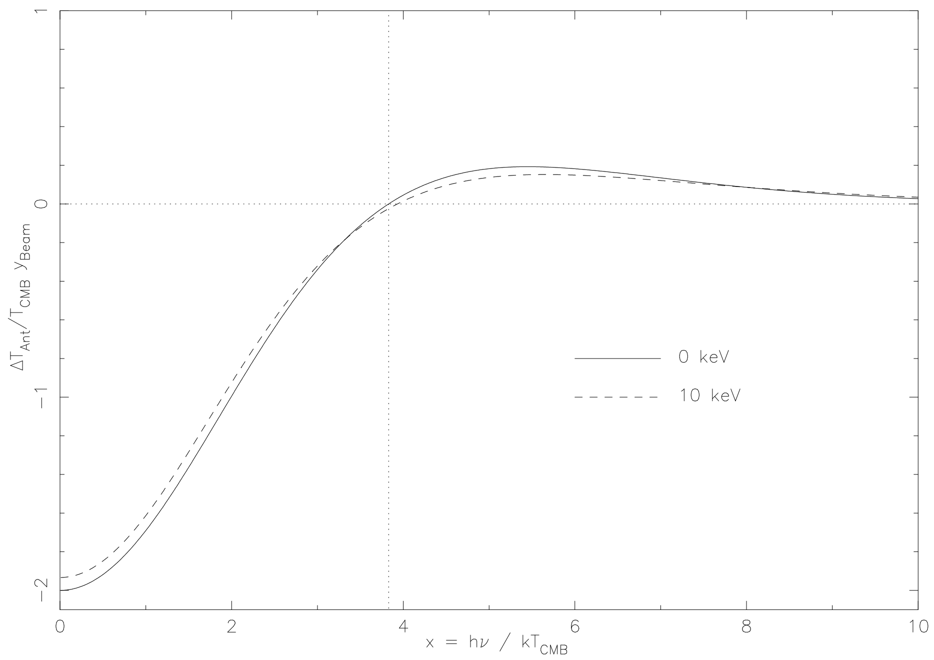

Figure 2.4: The proportionality between the observed antenna temperature and the beam-averaged Compton y parameter. In the Rayleigh-Jeans ($x \to 0$) limit for a non-relativistic cloud of electrons this is just -2.

We also define the Gaussian efficiency η_G as the ratio of the observed Compton y to the maximum Compton y averaged over the main beam:

$$\eta_G = \frac{y_{sw}}{y_{Beam}}. \tag{2.59}$$

This diagnoses the magnitude of the SZ signal lost to beam switching.

2.3.3 Impact of Cooling Flows and Phase Structure

The foregoing discussion all assumes that the ICM consists of a distribution of electrons which, at each point within the cluster, can be characterized by a single temperature and density. However it is well known that within the cooling radius the cluster gas has a multi-phase structure (Nulsen 1986; Thomas 1988). This occurs due to the cooling instability first pointed out by Nulsen (1986). This mechanism assumes the existence of a range of density fluctuations in the gas; these fluctuations become denser as they cool in order to maintain hydrostatic equilibrium with their surroundings, which in turn increases the cooling rate. The net effect of this is to create an inhomogeneous medium consisting of blobs of gas at different temperatures and densities. From our point of view the primary effect of a multi-phase ICM will be to increase the x-ray luminosity of the gas, since the x-ray emissivity is proportional to n_e^2 but only $T^{1/2}$. Because hydrostatic equilibrium obtains within the cluster core the integrated pressure is not changed by the cooling process, and the SZE signal is entirely unaffected by the development of a cooling flow. It is clear that the primary concern will be guarding the x-ray models from being contaminated by cooling-flow-related emission.

In Chapter 4, we describe our analysis of 44 ROSAT PSPC data sets on 22 clusters, including many with cooling flows. The strategy we adopt throughout the spectral analysis will be to excise the x-ray emission from the inner $150\,h^{-1}$ kpc of the cluster; this is a somewhat larger radius than the cooling radius of any of the clusters in our sample (Peres et al. 1998). In order that the profile fits not be biased by the enhanced x-ray emission at the cluster core, we fit the profiles with an extra free component (a Gaussian) to represent the cooling flow emission. The Gaussian component, since it is likely to be contaminated at some level by x-ray emission from many phases, is *not* used in our final density model. Instead, we model the SZE profile using just the β model component. Since the Gaussian component of the profile is negligible beyond $150\,h^{-1}$ kpc, a density model derived by combining the β model profile only and the count rate observed in the outer region will be an accurate representation of the cluster density profile in this regime. In this case even though the development of the cooling flow *dynamically* does not alter the SZE signal, there is the question of how accurately our radial extrapolation of the density profile into the cluster core describes the actual pressure there. We expect the uncertainty associated with this extrapolation to be small because the solid angle subtended by the cooling flow relative to the main beam is small.

To assess this uncertainty quantitatively, we calculated τ_{beam} for two models of A478, one of the prototypical cooling flow clusters in our sample. The first one was a single β model fit to the entire cluster emission, including the cooling flow. The second was a β model fit to all of the cluster emission with a free component to describe the cooling flow. Consistent with the analysis methods detailed in Ch. 4 (§ 4.1) we determine the relative densities in these models by the constraint that the x-ray luminosity between $0.15\,h^{-1}$ kpc and 1.5 h^{-1} Mpc is fixed. We find that the predicted value of τ_{beam} for the cooling flow model exceeds the prediction for the model which excises the cooling flow by 4.2%. Since the single β model fit is unrealistic in representing the gas inside the core by a single phase, this will overestimate the actual discrepancy; additionally, the fact that the single β model fits tend to bias β low will result in some cancellation of the excess in the predicted *switched* decrement.[2] Figure 2.5 shows the radial profile of the SZ signal along with the area-weighted 5.5-meter beam. In this example, our fiducial cooling radius of $150\,h^{-1}$ kpc corresponds to $2'.2$. In this calculation we have assumed that the ICM retains the same temperature in the cluster core as in the region outside. Waxman & Miralda-Escude (1995) have argued that the mass-weighted temperature of the ICM must remain approximately isothermal within the cluster core in order to reconcile the x-ray masses inferred at small radius with the strong-lensing masses, so this is not an entirely unrealistic assumption. All of this together indicates that the SZE measurements are rather insensitive to the details of the cluster-core astrophysics.

Gunn & Thomas (1996) have raised the possibility that other, more complicated astrophysical mechanisms could sustain a multi-phase ICM even at radii larger than the cooling radius. Since there is as yet no unambiguous observational evidence for the existence of such a situation, we regard these models as somewhat speculative. If it were to be the case, the consequences for the SZE predictions depend somewhat on the phase model assumed. If multiple phases were to exist throughout the cluster, there are two competing effects which would influence SZ models. First is the x-ray emissivity enhancement indicated previously, which would cause the overall electron density in the ICM to be overestimated. Second, the x-ray emission weighted temperature for the cluster as a whole would be underestimated. For more

[2]Since interferometers effectively switch on the scale of the spatial frequency associated with a given baseline, there will be a qualitatively similar effect for visibility predictions.

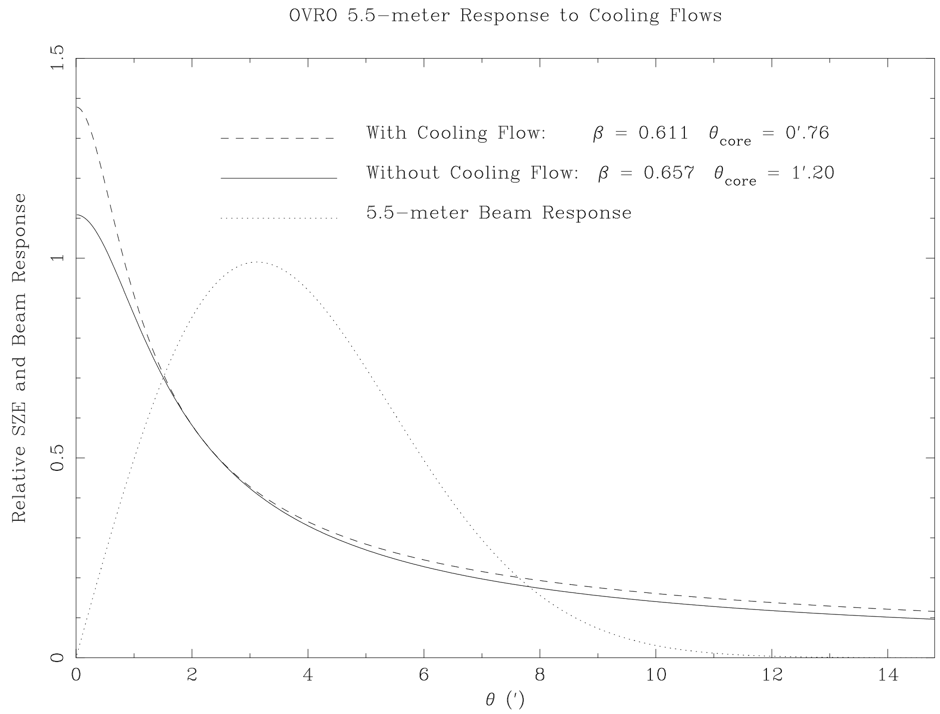

Figure 2.5: The effect of cooling flow emission on 5.5-m SZE predictions. Shown here are the SZE profiles for two models of A478. See text for details.

details on such models with specific discussions of the effect on the predicted SZ decrement, see Daisuke et al. (1999) and Holzapfel et al. (1997).

Note that our analysis of ROSAT PSPC data has in fact found some preliminary indications of cool phases outside of the cooling radius in several clusters (see Chapter 4). We discuss the potential error ($\sim 2\%$) in our inferred x-ray luminosities induced by the detected phases in § 4.1.2. Also, as we point in § 4.1.1, there are some potential ROSAT calibration issues which could give rise to spurious cool phases. In light of these considerations a multi-phase ICM can not be said to be confidently detected at a significant level in our analysis. New data from Chandra and XMM should be valuable in addressing this situation.

Chapter 3

X-ray Data on an Expanded Sample of Clusters

Due to the assumption of spherical symmetry necessary to employ the Sunyaev-Zeldovich effect as a distance measure, it is vital to measure the SZE in a large, geometrically unbiased sample in order to obtain a reliable measurement of H_0. As indicated in Chapter 1, an x-ray selected, x-ray flux limited sample satisfies this criterion. One of the historical concerns with optically selected catalogs, from which most cluster observations are selected, is that the optical selection may create a significant bias in the catalog since this selection is intrinsically surface-brightness limited. By way of comparison, the peak x-ray surface brightness of a typical nearby ($z < 0.1$) cluster is a factor of a few $10^2 - 10^3$ larger than the brightness of the x-ray background, whereas the corresponding surface density contrast in the optical is $\sim 20 - 50$. From this it is clear that an optically selected sample will be prone to orientation biases at much higher flux levels than the corresponding x-ray sample. An x-ray selected cluster sample will also be relatively less affected by chance alignments between poor groups (what is termed "projection effects" in the literature). The corner stone of our SZE-based H_0 measurement clearly then must be an orientation-unbiased sample of (preferably x-ray selected) clusters. The pioneering first steps in this direction were taken in Myers et al. (1997). Using the x-ray cluster sample of Edge et al. (1990), Myers et al. defined an x-ray flux limited sample of 11 galaxy clusters with fluxes $f_x > 3.11 \times 10^{-11}\,\mathrm{erg\,cm^{-2}\,s^{-1}}$ (2-10 keV), galactic latitudes $\mid b \mid > 20°$, and declinations $\delta > -23°$. Edge et al. selected these clusters from the ARIEL-V and HEAO-1 surveys, and cross-checked them against

Einstein and EXOSAT data.

In recent years it has become possible to greatly improve upon this sample using results and publicly available data from the ROSAT satellite. The possibility of a larger sample based on this data is attractive for two reasons. First, a larger sample will allow random errors due to projection effects to be reduced in the sample average. Second, and most importantly, measuring the SZE in a larger sample will allow systematic effects to be searched for by subdividing the sample and studying the resultant distributions of H_0. This strategy should reveal model-based systematics like a multi-phase ICM, significant temperature structure, or small-scale substructure if they are present at a significant level. Since such modeling systematics are currently the greatest unknown in H_0 determinations from the SZE, this is the fundamental scientific consideration which moves us to seek a larger sample. Experiments in the near future (such as Caltech's CBI) will be able to measure the SZE at an unprecedentedly rapid rate, enabling larger samples to be studied, and public x-ray data on many clusters are available online via NASA's HEASARC archive (`http://legacy.gsfc.nasa.gov/docs/`).

In this chapter we discuss this sample. We first define an expanded cluster sample of 31 clusters based on the Rosat All-Sky Survey (RASS) data (§ 3.1); next we describe the available (public) ROSAT data on 22 of these objects (§ 3.2) which will form the basis of our x-ray modeling endeavors in Chapter 4. Finally (§ 3.3) we summarize redshift and temperature data from the literature on these 22 clusters.

3.1 An Expanded Cluster Sample

A fully x-ray selected sample based on RASS data is not currently available. In the absence of such a sample, we have used the x-ray Bright Abell Cluster Sample (XBACS) of Ebeling et al. (1996). Ebeling et al. analyzed the data of the Rosat All Sky Survey (RASS) to obtain a sample of 242 Abell clusters complete at the 95% level down to a flux limit of $5.0 \times 10^{-12}\,\mathrm{erg\,cm^{-2}\,s^{-1}}$ in the $(0.1 - 2.4)\,\mathrm{keV}$ band. Their cluster-selection algorithm uses the Abell catalog as a parent catalog, which will necessitate extra caution in defining our sample. This and other potential biases inherent in the XBAC catalog will be discussed below.

If we adopt twice Ebeling's stated 95% completeness flux, or $f_x > 1.0 \times 10^{-11}\,\mathrm{erg\,cm^{-2}\,s^{-1}}$, there are 95 XBAC clusters above $b = \pm 20^\circ$. In order to obtain a more managably-sized sample and avoid the least luminous clusters, which are more prone to selection biases in the optical and will exhibit smaller SZ effects, we impose a luminosity cutoff. A convenient and natural luminosity cutoff is the luminosity which results in a volume-complete, flux-limited sample out to $z = 0.1$. The luminosity distance is (Weinberg 1972)

$$d_L = cH_0^{-1} z(1+z)[1 - \frac{1}{2}(1+q_o)z + O(z^2)]. \tag{3.1}$$

We have, taking $q_o = \frac{1}{2}$ and keeping terms to $O(z^2)$,

$$d_L = cH_0^{-1} z(1 + \frac{1}{4}z). \tag{3.2}$$

Evaluated numerically at a redshift of 0.1, this is

$$d_L(z = 0.1) = 291.52\, h^{-1}\,\mathrm{Mpc}. \tag{3.3}$$

The luminosity L_o which yields a volume-complete sample out to $z = 0.1$ and down to a flux f_o is

$$L_o = 4\pi d_L^2(z = 0.1) f_o; \tag{3.4}$$

for $f_o = 1.0 \times 10^{-11}\,\mathrm{erg\,cm^{-2}\,s^{-1}}$ this gives

$$L_o = 1.13 \times 10^{44} h^{-2}\,\mathrm{erg\,s^{-1}}. \tag{3.5}$$

(Note that the *XBAC* paper expresses L assuming $h = 0.5$ so their luminosities are a factor of 4 larger than those expressed in units of h). The sample resulting from these joint selection criteria (f_o, L_o) contains 31 clusters, listed in Table 3.1[1]. The richnesses and Bautz-Morgan types were obtained from Abell (1958) and Abell et al. (1989); all other quantities are from Ebeling et al. (1996). This sample contains all 11 of the original Edge-sample clusters defined in Myers et al. (1997). Note that in this table all fluxes and luminosities are the de-absorbed, 0.1–2.4 keV XBAC fluxes. While we obtain (Chapter 4) significantly more accurate fluxes for these clusters, we use the XBAC fluxes and luminosities for our sample selection since these are the quantities used by Ebeling et al. (1996) in assessing the completeness limits of XBAC as a whole.

[1]Note that the Coma cluster is Abell 1656.

There are two possible sources of geometrical bias in the XBAC catalog: a surface-brightness selection resulting from the optical selection process of Abell (1958) and Abell et al. (1989) (henceforth ACO), and a central-concentration bias arising from the subsequent x-ray selection of Ebeling et al. (1996). The former we address below. The latter is likely to select clusters with very strongly peaked central emission. This will tend to over-represent cooling flow clusters in the sample, which will not systematically invalidate the assumption of spherical symmetry. In fact these clusters are significantly more relaxed and symmetric than most non-cooling flow clusters.

A simple diagnostic of the level of projection effects liable to exist from the optical selection can be obtained by looking at the richness distribution of the sample. Abell et al. (1989) define the richness classes, R, in terms of the number of galaxies (after a background subtraction) within a specified radius and magnitude interval; practically it amounts to a qualitative measure of the galaxy content of a given cluster. Figure 1 shows the richness distribution in the XBAC sample as a whole. It is notable that 67% of the clusters in the XBAC sample as a whole are of richness class 0 or 1, i.e., they are relatively poor clusters. Figure 2 shows the effect of introducing luminosity cutoffs of 0.5×10^{44} and $1.13 \times 10^{44}\,\mathrm{erg\,s^{-1}}h_{\frac{1}{2}}^{-2}$ to the $z < 0.1$, $F_x > 1.0 \times 10^{-11}\,\mathrm{erg\,cm^{-2}\,s^{-1}}$ subset of *XBAC* . For the higher luminosity cutoff (corresponding to the volume complete sample we have indicated above) 77% of the subsample is of Richness class 2 or greater, whereas for the *XBAC* sample as a whole only 33% of the clusters fall into this range. A comparison of the Abell and ACO surveys in their region of overlap (Scaramella et al. 1991) indicates that Abell misses 29% of $R \geq 1$ clusters relative to ACO; most of these are $R = 1$ clusters. This is consistent with the results of Van Haarlem et al. (1997) who find 30% of $R \geq 1$ clusters are missed in Monte-Carlo simulations of an optical selection designed to mimic that of Abell and ACO. In most cases, these clusters are missed due to fluctuations in the background galaxy counts resulting in the misclassification of actual clusters as poorer objects which are not included in the catalog; since this misclassification affects the poorer clusters to a greater extent, most of the missed clusters are again likely to be richness class 1 objects. Van Haarlem et al. also find that an after-the-fact x-ray selection of clusters with $L_x > 1.0 \times 10^{44}\,\mathrm{erg\,s^{-1}}$ (0.5-2.5 keV) provides a sample which, while not complete, is free from projection effects; this is a somewhat *lower* luminosity cutoff than our $L_x > 1.13 \times 10^{44}\,\mathrm{erg\,s^{-1}}$ (0.1-2.4 keV). This, together with the fact that only 23% of our sample have $R \leq 1$, argue that the sample we have defined should be free of significant orientation bias.

One can obtain a good idea of the completeness of the *XBAC* sample at high luminosities by comparing it to the sample of Edge. *XBAC* finds all of the Abell clusters found by Edge; in addition, Edge finds (excluding low galactic latitude clusters, which are not in our sample) only three other clusters (MKW3s, Virgo, and 0336+09). Of these three, Ebeling et al. explicitly excluded Virgo from their analysis, leaving $\frac{2}{46} = 4.3\%$ of clusters missed. This is much better than the 29% estimated by Scaramella et al., due to the fact that the Edge clusters are among the most luminous of x-ray clusters ($L_x \gtrsim 6.4 \times 10^{44}\,\mathrm{erg\,s^{-1}}$, 0.1-2.4 keV) and hence are very rich and unlikely to be missed in optical surveys. Furthermore, the fact that all of the Myers et al. subsample is contained in the sample we have defined is a direct indication that the luminosity selection imposed by Myers et al. ($L_x \gtrsim 1.25 \times 10^{44}\,\mathrm{erg\,cm^{-2}\,s^{-1}}$, 2-10 keV, or roughly $L_x \gtrsim 1.8 \times 10^{44}\,\mathrm{erg\,cm^{-2}\,s^{-1}}$ in the 0.1 - 2.4 keV band) would be effective at eliminating optical selection effects from our sample.

Based on these results, we estimate our sample to be 90% complete for $L_o = 1.13 \times 10^{44} h^{-2}\,\mathrm{erg\,s^{-1}}$, $f_o = 1.0 \times 10^{-11}\,\mathrm{erg\,cm^{-2}\,s^{-1}}$. This corresponds to 3 missed clusters at most. This level of incompleteness will not significantly affect H_0 measurements derived from the sample as a whole. Near-future fully x-ray selected surveys such as the ESO REFLEX survey will allow the completeness of this sample to be checked.

Code	Source	RA	Dec	z	F_x	L_x
ep-s	A2142	15:58:22.1	+27:13:58.8	0.0894	61.4	20.74
ep-s	A2029	15:10:55.0	+05:43:12.0	0.0766	61.6	15.35
ep-s	A478	04:13:26.2	+10:27:57.6	0.0882	39.1	12.95
epas	A1795	13:48:52.3	+26:35:52.8	0.0622	67.2	11.12
epas	A401	02:58:56.9	+13:34:22.8	0.0739	42.6	9.88
-p--	A2244	17:02:40.1	+34:03:46.8	0.0970	22.8	9.09
-pas	A3667	20:12:23.5	−56:48:46.8	0.0530	73.1	8.76
ep-s	A85	00:41:48.7	−09:19:04.8	0.0521	72.3	8.38
ep-s	A1651	12:59:24.0	−04:11:20.4	0.0846	27.1	8.25
epcs	A754	09:09:01.4	−09:39:18.0	0.0542	64.1	8.01
-p-s	A2597	23:25:16.6	−12:07:26.4	0.0852	25.9	7.97
-r-s	A1650	12:58:41.8	−01:45:21.6	0.0845	25.6	7.81
-r--	A3827	22:01:56.6	−59:57:14.4	0.0990	18.7	7.78
-p-s	A3112	03:17:56.4	−44:14:16.8	0.0703	36.4	7.70
-p-s	A3571	13:47:28.1	−32:51:14.4	0.0397	109.5	7.36
epc-	A1656	12:59:31.9	+27:54:10.8	0.0231	316.5	7.21
epas	A2256	17:04:02.4	+78:37:55.2	0.0581	49.0	7.05
----	A2384	21:52:16.6	−19:36:00.0	0.0940	18.2	6.82
-p-s	A780	09:18:06.7	−12:05:56.4	0.0565	48.4	6.63
ep-s	A399	02:57:49.7	+13:03:10.8	0.0722	29.0	6.45
-p-s	A3558	13:27:57.8	−31:29:16.8	0.0477	64.6	6.27
-p-s	A3266	04:31:25.4	−61:25:01.2	0.0545	48.5	6.15
-r--	A4010	23:31:14.2	−36:30:07.2	0.0962	14.1	5.55
-p--	A3921	22:49:59.8	−64:25:51.6	0.0953	14.0	5.40
-p--	A3158	03:42:43.9	−53:38:27.6	0.0590	35.7	5.31
-r--	A2426	22:14:32.4	−10:21:54.0	0.0990	12.2	5.10
-r--	A3695	20:34:46.6	−35:49:48.0	0.0889	15.1	5.07
-r-s	A2065	15:22:26.9	+27:42:39.6	0.0723	22.3	4.95
-p--	A2255	17:12:45.1	+64:03:43.2	0.0809	17.2	4.79
----	A566	07:04:22.3	+63:16:30.0	0.0980	11.3	4.62
----	A3911	22:46:20.9	−52:43:30.0	0.0960	11.8	4.61

Table 3.1: SZE cluster XBAC subsample. Columns are: F_x , $10^{-12}\,\mathrm{erg\,cm^{-2}\,s^{-1}}$, $0.1-2.4\,\mathrm{keV}$; L_x , $10^{44}\,\mathrm{erg\,s^{-1}}, h=\frac{1}{2}$. Codes are four letters indicating the current status of x-ray observations for the cluster. An "e" in the first position indicates presence of the cluster in Edge sample. An "r" in the second position indicates the existence of non-public ROSAT PSPC observations of the cluster; a "p" indicates the existence of public ROSAT data for the cluster. A "c" in the third position indicates that the cluster has been targeted for observation during the AXAF CAL cycle (this data becomes public immediately); "a" indicates that the cluster has been otherwise targeted during AXAF cycle 1. An "s" in the fourth position indicates that Markevitch et al. have obtained an ASCA temperature for the cluster.

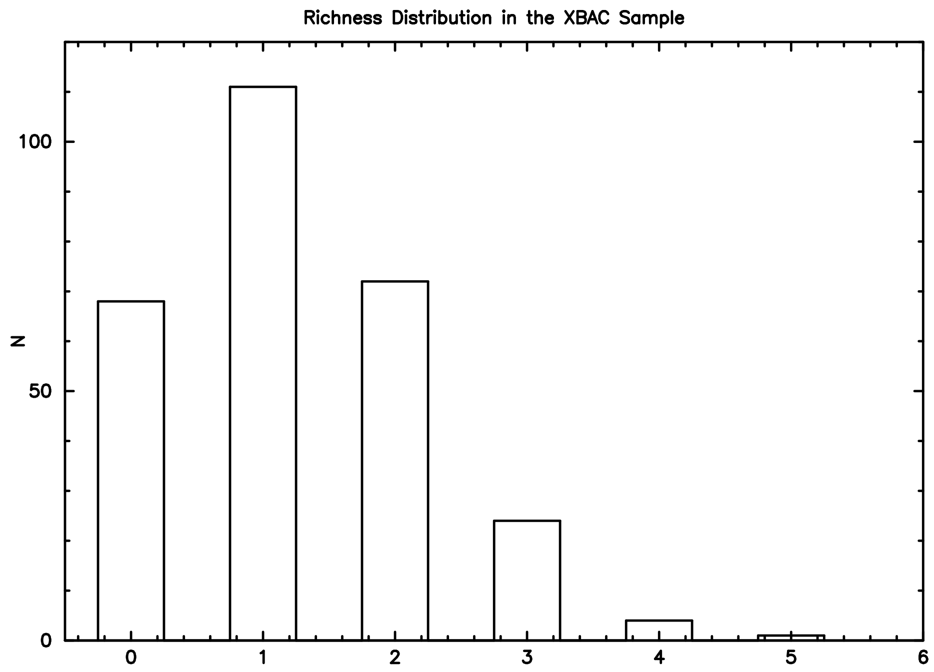

Figure 3.1: Richness distribution in the $XBAC$ sample as a whole. 67% of the sample are poor (richness 0 or 1) clusters.

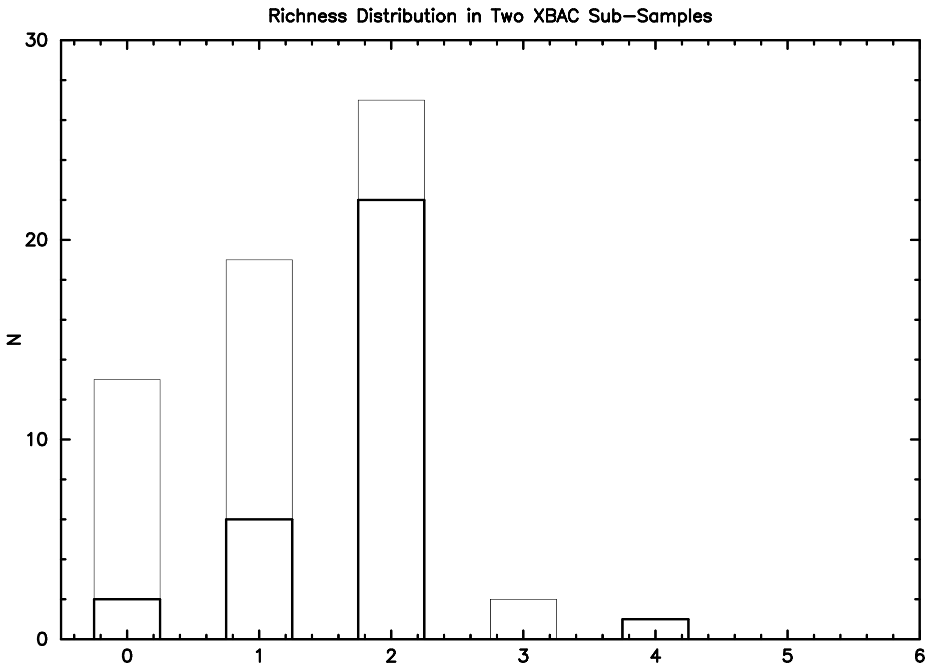

Figure 3.2: Richness distribution in two *XBAC* subsamples. The bold line is the sample defined in the text; the lighter line is a sample defined with half the luminosity cutoff of the sample defined in the text. Only 23% of the clusters in the high-cutoff sample are richness 0 or 1.

3.2 Summary of Observations

The ROSAT public data archive at NASA's Goddard Space Flight Center was searched for each cluster in the sample we defined in § 3.1. A total of 44 data sets on 22 clusters were obtained. These data sets are listed in Tables 3.2 and 3.3 Shown in these tables are the ROSAT sequence ID for each observation, the exposure time in seconds (the `LIVETIME` from the FITS file), the nominal observation offset, the observation date, and a name (the observation tag) given to the data set for easy reference. Also shown in the date column is a tag indicating the detector state at the time of the observation: C indicates PSPC C, B indicates PSPC B, and BH indicates the PSPC B detector in its high gain state. The redundancy of data on any given cluster allows us to check for systematic errors in the data reduction such as would arise due to short-term detector gain fluctuations or overall offsets between the calibration matrices employed in analyzing the B,BH, and C data.

The analysis and interpretation of these data are discussed in Chapter 4.

Cluster	Sequence ID	Observation Tag	Exposure (sec)	Offset (arcmin)	Observation Date
A85	rp800250N00	a85a	10238	4.74	01jul92 (B)
	rp800174A00	a85b	2187	5.20	20dec91 (B)
	rp800174A01	a85c	3458	5.20	11jun92 (B)
A401	rp800182N00	a401a	6735	0.22	23jan92 (B)
(incl. A399)	rp800235N00	a401b	7457	0.22	30jul92 (B)
A478	rp800193N00	a478a	21969	0.4	31aug91 (BH)
a754	rp800550N00	a754a	8156	12.13	06nov93 (B)
	rp600451N00	a754b	13495	22.34	03nov92 (B)
	rp800160N00	a754c	2266	12.13	19nov91 (B)
	rp800232N00	a754d	6358	12.13	10nov92 (B)
A780	rp800318n00	a780a	18398	12.00	08nov92 (B)
A1651	wp800353	a1651a	7435	3.41	18jul92 (B)
A1656	rp800009n00	a1656a	20345	33.04	16jun91 (BH)
	rp800006n00	a1656b	21545	9.98	16jun91 (BH)
	rp800005n00	a1656c	21140	2.23	17jun91 (BH)
	rp800013n00	a1656d	21428	15.85	18jun91 (BH)
A1795	rp700284N00	a1795a	2025	13.84	30jun91 (BH)
	rp700145A01	a1795b	1909	13.84	06jan92 (B)
	rp700145A00	a1795c	18205	13.84	01jul91 (BH)
	rp800105N00	a1795d	36273	0.58	04jan92 (B)
	rp80055N00	a1795e	25803	1.67	09jul91 (BH)

Table 3.2: Partial catalog of public ROSAT observations of clusters in the sample defined in Table 3.1. The remainder of the public observations are cataloged in Table 3.3.

Cluster	Sequence ID	Observation Tag	Exposure (sec)	Offset (arcmin)	Observation Date
A2029	rp800161N00	a2029a	3151	1.12	24jan92 (B)
	rp800249N00	a2029b	12542	0.32	10aug92 (B)
A2142	rp800415N00	a2142a	19208	15.78	21aug92 (B)
	rp150084N00	a2142c	7734	0.46	20jul90 (C)
	wp800096	a2142d	6192	0.46	25aug92 (B)
	rp800551N00	a2142e	6090	0.46	23jul93 (B)
	rp800233N00	a2142f	4939	0.46	26aug92 (B)
A2244	rp800265N00	a2244a	2963	1.82	21sep92 (B)
A2255	rp800512n00	a2255a	14555	1.64	24aug93 (B)
A2256	rp100110N00	a2256a	17032	0.18	17jun90 (C)
	rp800163N00	a2256b	10681	14.51	25nov91 (B)
	rp800340N00	a2256e	9422	22.59	25jul92 (B)
	rp800341N00	a2256f	10473	16.54	23jul92 (B)
	rp800162A00	a2256g	4246	13.35	15oct91 (B)
	rp800162A01	a2256h	4747	13.35	15mar92 (B)
	rp800339N00	a2256i	4978	13.35	22jul92 (B)
A2597	rp80012N00	a2597a	7163	1.12	27nov91 (B)
A3112	rp800302N00	a3112a	7598	4.50	17dec92 (B)
A3158	rp800310n00	a3158a	3020	19.08	26aug92 (B)
A3266	rp800552N00	a3266a	13547	2.14	19aug93 (B)
A3558	rp800076n00	a3558a	29490	1.48	17jul91 (BH)
A3571	rp800287n00	a3571a	6062	12.08	12aug92 (B)
A3667	rp800234n00	a3667a	12550	0.26	09oct92 (B)
A3921	rp800378n00	a3921c	11997	1.19	15nov92 (B)

Table 3.3: Partial catalog of public ROSAT observations in the sample defined in Table 3.1. The remainder of the public observations are cataloged in Table 3.2.

3.3 Temperatures and Redshifts

While some investigators have measured x-ray temperatures using the PSPC (e.g. Briel & Henry 1994, 1996), these efforts are hindered by the limited spectral resolution and bandpass of this instrument. We have chosen instead to use temperatures obtained from ASCA, GINGA, or EXOSAT observations, and searched the literature in order to find the most accurate and reliable ICM temperatures available. This task is made considerably easier by the fact that most of the clusters in our sample have ASCA-measured temperatures obtained by Markevitch et al. (1998). While many of these clusters also have temperatures reported in the compilation of David et al. (1993), we choose to use the Markevitch et al. results since they have been most careful about excluding contaminating components such as cooling flows, central AGN's, and bright point sources. We do not employ the suggested temperature profile of Markevitch et al. (1998) since these results are prone to be affected by any errors in the characterization of the ASCA point spread function. With the exception of Coma, we assume that the cluster gas is isothermal. In Chapter 6 we discuss the potential impact of this assumption on our SZE predictions.

One notable difference between the Markevitch et al. temperatures and those published in the compilation of David et al. is that the David et al. cooling flow cluster temperatures are systematically *lower*. It is likely that this is due to the fact that none of the temperatures in the analyses summarized by David et al. correct for the presence of cool phases in the cluster center (either by excising this emission or allowing free cool components in the spectral fit). It is also notable that the error bars quoted by David et al. are significantly smaller than those of Markevitch (sometimes smaller than 1%!). Since the literature does not reflect agreement on individual cluster temperatures at this level, we think that the potential impact of systematic errors on many of these results may be significantly underestimated. The errors on the Markevitch et al. temperatures are more likely to reflect the real uncertainty in the cluster temperatures, and these relatively large uncertainties will often turn out to be the limiting factor in our predictions of the thermal SZE decrement. More accurate cluster temperatures are highly desirable. This will have to await the accurate spectral calibration of current and future x-ray missions.

Redshifts have been obtained from the compilation of Struble & Rood (1991).

Cluster	T_e (KeV)	z
A85	6.9 ± 0.4	0.0518
A399	7.0 ± 0.4	0.0715
A401	8.0 ± 0.4	0.0748
A478	$8.4^{+0.8}_{-1.4}$	0.0900
A754	$9.5^{+0.7}_{-0.4}$	0.0528
A780	4.3 ± 0.4	0.0522
A1651	6.1 ± 0.4	0.0825
A1656	9.1 ± 0.7^{A}	0.0232
A1795	7.8 ± 1.0	0.0616
A2029	9.1 ± 1.0	0.0767
A2142	$9.7^{+1.5}_{-1.1}$	0.0899
A2244	$7.1^{+2.4\ B}_{-1.5}$	0.0980
A2255	$7.3^{+1.7\ B}_{-1.1}$	0.0800
A2256	6.6 ± 0.4	0.0601
A2597	$4.4^{+0.4}_{-0.7}$	0.0852
A3112	$5.3^{+0.7}_{-1.0}$	0.0703^{C}
A3158	$5.5^{+0.3\ B}_{-0.4}$	0.0590^{C}
A3266	8.0 ± 0.5	0.0594^{C}
A3558	5.5 ± 0.4	0.0482^{C}
A3571	6.9 ± 0.2	0.0397^{D}
A3667	7.0 ± 0.6	0.0552^{E}
A3921	6.6 ± 1.6^{F}	0.0960^{G}

^{A} Markevitch (1999)
^{B} David et al. (1993)
^{C} Abell et al. (1989)
^{D} Vettolani et al. (1990)
^{E} Sodre et al. (1992)
^{F} Ebeling et al. (1996) with our estimated error.
^{G} Dalton et al. (1994)

Table 3.4: Electron temperatures are from Markevitch et al. (1998) except as noted; redshifts are from Struble & Rood (1991) except as noted. All errors are 90% confidence limits.

Chapter 4

X-Ray Data Analysis and Interpretation

In order to determine the density of a cosmic plasma emitting thermal bremsstrahlung radiation, it is necessary to know both the x-ray flux (in some band or bands) observed at some distance $D_L(z)$, the temperature of the plasma, and the spatial distribution of the electrons and ions (see Eq. 2.8). In the previous chapter, we summarized ASCA-determined emission-weighted electron temperatures for the 22 clusters in our public ROSAT sample; in this chapter, we turn our attention to the determination of the x-ray fluxes over the PSPC bandpass and the derivation of density models for these clusters. First (§ 4.1) we describe the methods employed to analyze the spectral data on these clusters, including the calibration of the data. In this section we present fluxes and luminosities for our clusters. Second, (§ 4.2) we discuss our spatial profile analysis. Next (§ 4.3) we discuss an extensive suite of Monte-Carlo simulations which were carried out in order to quantify the random errors in our derived models due to noise in the images, and to test for potential systematic biases introduced by instrumental effects and our analysis methods. Finally (§ 4.4) we present the results of our analysis: baryonic and total masses for these 22 galaxy clusters and uncertainties in these quantities obtained by the methods of § 4.3. We also check for the effects of adopting a set of plausible alternative models not encompassed by our Monte Carlo simulations. In Appendix A we give the images and profiles resulting from this analysis.

4.1 Spectral Analysis

Modern x-ray telescopes such as the ROSAT PSPC provide images of the x-ray surface brightness, to which several corrections must be made in order to calculate a flux. Most importantly, the flux due to instrumental and cosmic backgrounds must be subtracted from the observed images. While these backgrounds are usually of fairly low surface brightness (less than 1% of the peak surface brightness of a typical cluster), they can contribute significantly to the total flux since they subtend the entire field of view. The principal backgrounds for the ROSAT PSPC are the particle background, caused by un-vetoed events from cosmic rays; solar radiation scattered by the earth's upper atmosphere; and a poorly-understood but well-modeled time variable background known as the LTE (long-term enhancement). For extended objects, or objects observed a significant distance from the center of the focal plane, it is important to account for telescope vignetting. This is simply a multiplicative factor which accounts for the variations in the effective exposure across the face of the detector; these variations arise primarily from the scattering-angle dependence of the efficiency of the mirrors used to focus the x-rays, and shadowing caused by elements of the instrument in the light path. Finally, the diffuse cosmic x-ray background, point source contaminants, and residual instrumental backgrounds must be removed from the image.

We chose to use the Extended Source Analysis Software (ESAS) described in Snowden et al. (1994) in order to accomplish these tasks. This package includes the facilities for modeling and subtracting the known ROSAT backgrounds, as well as performing the energy-dependent vignetting correction. The raw photon event and aspect files for the data described in § 3.2 were obtained from the HEASARC online archive and reduced. All data with Master Veto count rates of greater than 170 counts per second were excluded from the analysis; this removes periods of time affected by solar flares, enhanced particle background, or other highly variable, short-term count-rate enhancements. For each observation, this procedure yields a background-subtracted count rate image, an exposure image, and a raw counts image in each of the 7 Snowden bands. These bands are summarized in Table 4.1. All maps are 512 x 512 pixels, with pixels $14''.947$ on a side. None of the band 3 data products are used, since this band has very little signal and is generally unsupported under ESAS. The count-rate maps are the basic data products for our spectral analysis; they have had the modeled background subtracted and the telescope exposure (or vignetting) correction applied. While in principle the electron density can be determined from a single count rate (over the 0.5 – 2.0 keV band, for instance), we chose to use R2 and R4 — R7 separately, since this format is most straightforward to use in `XSPEC`, and provides some basic spectral information which is useful as a check on the Galactic neutral hydrogen column densities and the assumed plasma model.

For each observation of a single cluster with a single instrument (PSPC B and BH— there were no multiple observations with the PSPC C), all individual pointings were mosaicked (again using the ESAS software) to form a single count rate image for the cluster. These data form the basis for our highest signal-to-noise analyses where available. These mosaicked observations are referred to by the tags BM and BHM; a catalog of the mosaics is presented in Table 4.2.

Point source masks were derived using ESAS's `DETECT` algorithm, which employs a variable detection aperture to account for the change in the ROSAT point-spread function across the detector face. All sources detected with greater than 99% confidence in the 0.5 – 2.0 keV band, and having total count rates greater than 5×10^{-3} counts per second were masked. This is potentially important, since the variability of the point spread function and the detector vignetting are likely to bias point source masks created "by eye". Using the exposure maps calculated by ESAS, all regions with exposures less than 30% of the maximum are also masked; this removes data for which

Band Name	Energy (keV)	Centroid (keV)
R1	0.11 – 0.284	0.197
R2	0.14 – 0.284	0.212
R3	0.20 – 0.83	—
R4	0.44 – 1.01	0.725
R5	0.56 – 1.21	0.850
R6	0.73 – 1.56	1.140
R7	1.05 – 2.04	1.540

Table 4.1: Snowden PSPC energy bands, along with their approximate centroids. Since band 3 straddles an absorption edge due to carbon in the PSPC window, it is not significant to designate a centroid for this band. This band is not used in any subsequent analysis.

Mosaic	Pointings
A2142BM	A2142A,E,F
A2256BM	A2256B,E–I
A85BM	A85A–C
A401BM	A401A,B
A754BM	A754A–D
A2029BM	A2029A,B
A1795BHM	A1795A,C,E

Table 4.2: A catalog of the mosaics used in the spectral analysis.

the vignetting correction is more than a factor of ~ 3. Typically $\sim 10\%$ of the pixels are masked by this step, primarily those shadowed by the PSPC window support structure. Figure 4.1 shows the exposure map for band R6 of the A478A observation (here convolved with a $30''$ FWHM Gaussian for display purposes).

We extracted count rates from each of these images using two independent methods: by fitting a $\beta-$model (plus a Gaussian where necessary) to the azimuthal profile of each band image, and by extracting the count rate from each band image and subtracting a mean background estimated from a $\sim 5'$ annulus located $\sim 35'$ away from the cluster center. We call these the "beta" and "ring" methods respectively. The ring and beta methods generally give consistent results within errors for bands R4–R7; as an example, the ring and beta spectra for A478, A2142, and A2256 are shown for all bands in Table 4.3. The ring spectra often give meaningless results for R1 and R2; for these bands, the backgrounds are stronger, significantly more spatially variable, and the cluster signal is also weaker due to Galactic absorption. The beta spectra also correctly interpolate the cluster flux in masked regions, are less sensitive to the details of the point source masking, and allow the extrapolation of the observed spectrum to slightly larger fields of view (important, for instance, on Coma). For these reasons we use the beta spectra for all subsequent analysis.

In cases where a significant central cool component of emission is detected by Markevitch et al. (1998), we have excised the inner $150h^{-1}$ kpc of emission before extracting the spectra. This is well beyond the cooling radius for most of the clusters in our sample. Peres et al. (1998) obtain a cooling radius ($r_{cool} = 102^{+38}_{-27}h^{-1}$ kpc) for A1795, one of the strongest cooling-flow clusters in our sample; even for this cluster, there is a margin for error.

We have estimated the error on each band's count rate using the relation

$$\frac{\epsilon_N}{N} = \sqrt{\frac{2}{N}} \tag{4.1}$$

for the fractional error in the fitted number of total counts N; the fractional error in the count rate is equal to this quantity. N for each band was obtained from the raw (un-vignetting-corrected) count map. We have found this relation to hold in Monte Carlo simulations of idealized $\beta-$models with realistic signal and background levels (see § 4.3). For most observations the Poisson error is between 0.5% and 3% in bands R4–R7. Based on fits to a few initial data sets, we estimated an additional 1.5% error in addition to this Poisson error due to model residuals.

The count rates so extracted from our cleaned images were converted into `.pha` files using the `FTOOL` `ascii2pha` and analyzed using `XSPEC`. The results of this analysis are tabulated in Appendix B; the density models which result will be discussed in § 4.4.

Exposure:	A478A	A2142C	A2256A
Band		S_{ring}/S_{beta}	
R1	-0.54 ± 0.12	0.68 ± 0.31	0.72 ± 0.15
R2	5.45 ± 0.57	0.87 ± 0.09	1.00 ± 0.10
R3	—	—	—
R4	0.98 ± 0.04	1.09 ± 0.04	1.00 ± 0.03
R5	0.99 ± 0.03	1.01 ± 0.03	0.99 ± 0.03
R6	1.02 ± 0.03	0.97 ± 0.03	0.97 ± 0.03
R7	1.04 ± 0.03	1.00 ± 0.03	0.97 ± 0.03

Table 4.3: Comparison of the Ring and Beta spectra for A478, A2142, and A2256. Shown are the count rate ratios and errors in each band. The R1 flux ratio errors are dominated by the 500 count AP residual we have allowed for in the beta spectra; the other errors typically contain comparable contributions from the ring and beta count rate measurements; see the text for details on our error estimates.

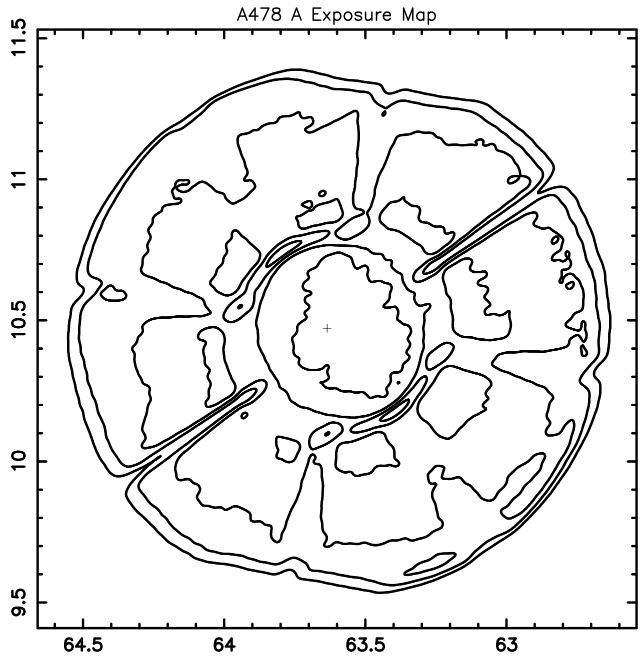

Figure 4.1: A typical PSPC exposure map, showing the effects of vignetting. Contours are at effective exposures of 4, 8, 12, 16, and 20 ksec; the maximum exposure (22.8 ksec) is denoted by "+".

4.1.1 Galactic Hydrogen Absorption, Cool Phases, and the PSPC Calibration

Our accurate extraction of the R2 and R4–R7 count rates allows us to use the absorbing column density as a free parameter in our spectral analysis. Since some concern has been raised in the literature about excess absorption over the Galactic values Allen et al. (in particular, 1993), and since it is unclear whether there is small-scale structure in the Galactic Hydrogen column density itself, this is a potentially valuable degree of freedom. Any systematic misestimation of the absorbing column density will bias our inferred x-ray luminosities, and hence H_o.

The results of this exercise are somewhat discouraging. Out of 22 clusters, 4 (A478,A754, A2256, and A3266) show absorbing column densities higher than the Galactic value, 3 (A401, A2029, and A3158) are consistent or marginally consistent with the Galactic value, and 15 are significantly lower than the Galactic value. While it would be possible for the column densities to be systematically *higher* than the Galactic column density due to extragalactic neutral hydrogen along the line of sight (e.g., associated with the cluster), no effect can make the absorbing column densities systematically *lower* than the Galactic value. Substructure in the Galactic disk, for example, should only cause a scatter in the observed column densities. To illustrate that this is not a systematic artifact of our spectral extraction, Figure 4.2 shows the observed spectrum (R1-R7) for A85BM with the best-fit Raymond-Smith model having the column density fixed at the Galactic value, and Figure 4.3 shows the fit to the R2 image used to compute the count rate. It is clear that the observed excess of counts in the R2 band is not due to systematics in the spectrum extraction. The inner $150h^{-1}$ kpc of emission has been excluded in this example.

The most significant case of absorption over the Galactic value in our sample is A478. For this cluster, the level of absorption is enough to render R1 and R2 effectively useless; nevertheless, we are able to constrain the absorbing column density using only bands R4–R7. If we exclude the central $150h^{-1}$ kpc of emission and fix the absorbing column density at the Galactic value ($14.8 \times 10^{20}\mathrm{cm}^{-2}$), the best-fit Raymond-Smith model has $\chi^2_\nu = 17.7$ for 3 D.O.F.; allowing the absorbing column density to be free and fitting for it, we obtain $21.1 \pm 1.0 \times 10^{20}\mathrm{cm}^{-2}$ with $\chi^2_\nu = 1.90$ for 2 D.O.F. We also tried modeling the spectrum with two Raymond-Smith components (one at 8.4 keV and one at a range of hotter temperatures) plus Galactic absorption; all

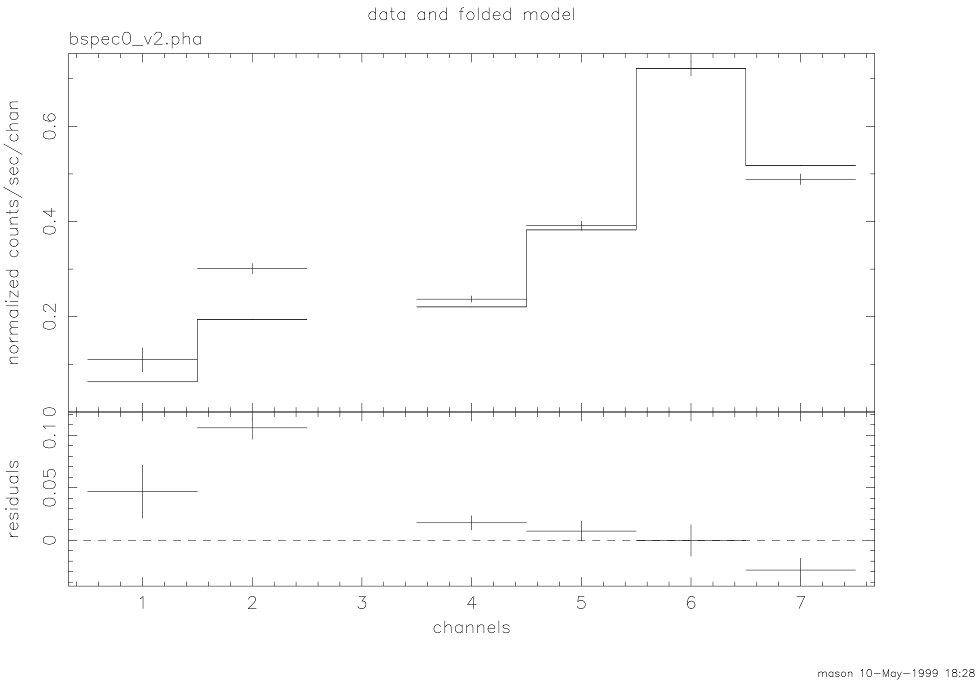

Figure 4.2: Observed spectrum for A85 BM compared to the best-fit Raymond-Smith model with Galactic absorption.

of these yielded χ^2_ν values *higher* than those given by the single-phase Galactic absorption fits. Our best results are consistent with the result of a single-phase fit to all of the cluster emission (including the cooling flow), which yields an absorbing column density of $22.5 \pm 0.7 \times 10^{20}\mathrm{cm}^{-2}$ and $\chi^2_\nu = 3.2$ for 2 D.O.F.; allowing a second, cool phase in this fit yields a lower χ^2_ν and a slightly higher column density. The column densities we determine are significantly in excess of the Galactic value. Allen et al. (1993) have measured an absorbing column density of $24.9^{+1.2}_{-0.9} \times 10^{20}\mathrm{cm}^{-2}$; if we adopt the electron temperature they have used in their analysis (6.6 keV) we achieve results consistent with theirs at the 1.5σ level. For this cluster and this cluster only, we use our best-fit column density ($21.1 \pm 1.0 \times 10^{20}\mathrm{cm}^{-2}$) instead of the Galactic column density. If the Galactic column density is used instead, the cluster luminosity is underestimated by 18%.

The fact that we consistently observe a deficit in the fitted column density relative to the Galactic expectation is equivalent to there being an excess of counts in the soft channels if we consider the Galactic hydrogen column densities, on average, to be reliable. There are two possible explanations for such an effect. One is that in most of the clusters we observe, there is a widespread cool phase. While this is not likely at radii larger than the cooling radius, a variety of astrophysical mechanisms may permit such a situation (see, for example, Gunn & Thomas 1996). In order to diagnose the significance of this, we examined in detail three of the clusters (A85, A1651, and A1656) showing particularly low column densities in our spectral fits. In two of the three cases (A1651 and A1656) fits of comparable quality to the free-Hydrogen fit are achieved if the gas is assumed to be at ~ 0.1 keV; in these cases, the contribution of the cooler phase to the observed flux is $\sim 5\%$ of the total flux. Since the cool phases (under the assumption of hydrostatic equilibrium) are highly over-represented in the x-rays, such a phase in itself contributes negligibly to the baryonic mass and hence the SZE. On the other hand, the best-fit flux for the dominant (hot) Raymond-Smith component is reduced by $\sim 5\%$ for these two clusters; this is comparable to the reduction in de-absorbed flux that we infer for a single-component fit with a free absorbing

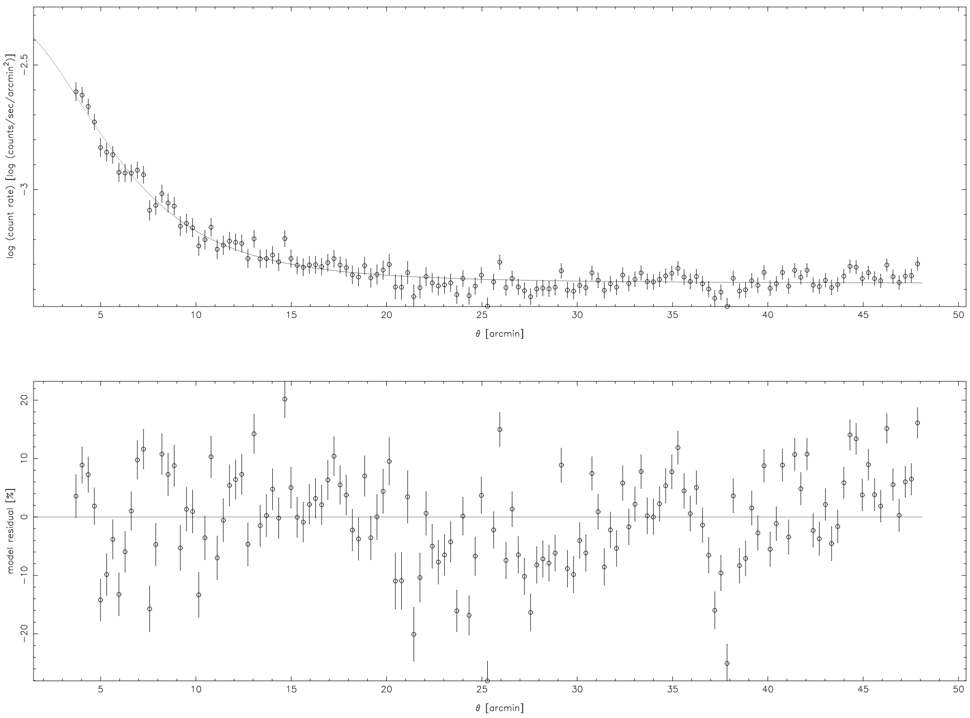

Figure 4.3: Fit to the A85 BM R2 azimuthal profile, excluding cooling flow emission.

column density for these clusters.

Another, and perhaps more likely, possibility is that there is a systematic error in the PSPC calibration. This has been recently suggested by Iwasawa et al. (1999) on the basis of a comparison of the spectral indices inferred from ASCA and ROSAT data on the AGN NGC5548. These authors find that the ROSAT spectral index is significantly steeper than the ASCA spectral index over the same energy range. This is consistent with the excess of soft counts which we observe.

If we use our best fit absorbing column densities for the sample as a whole (excluding A478), the average ratio of the de-absorbed luminosity to the de-absorbed luminosity inferred assuming Galactic absorption is 0.977 ± 0.007. We take this 2.3% error as indicative of the level of systematic error induced by the calibration error suggested by Iwasawa et al. (1999) and/or cool phases at large radius and include it in our final error budget. Errors at this level can be expected when different software is used to derive fluxes from count rates. For example, `PROS` converts the observed count rate directly into a flux using a set of models with no assessment of the goodness-of-fit across the spectrum, whereas `XSPEC` quotes the best-fit *model* flux. Thus if the total count rate in the model and the observation disagree at the 2% level, so will the inferred fluxes.

4.1.2 Estimate of the Systematic Errors

In assessing the level at which systematic errors affect our results, there are two basic issues: repeatability and the overall (non-variable) calibration uncertainty. Some degree of non-repeatability from one observation to the next may be introduced if, for instance, the PSPC gains were to change slightly and in a systematic way across the band, which would affect our spectral fits and hence our derived luminosities. The overall calibration is dependent primarily on the mirror effective areas and energy response matrices used to generate the `.rmf` and `.arf` files used to calibrate the data.

We use the following data sets to evaluate the repeatability of our measurements: A85 A–C; A401 A,B; A754 A–D; A1795 C–E; A2142 A,C; and A2256 A,F. The standard deviation in the ratio of the fluxes in the individual observations to the mean flux for each object is 2.9%. We take this to characterize the 1σ precision of our measurements.

Snowden et al. (1995) estimate the ROSAT PSPC absolute calibration uncertainty by comparing the RASS fluxes to the fluxes observed in other all-sky surveys (Wisconsin (M$^{\rm c}$Cammon et al. 1983), HEAO-1 (Garmire et al. 1992), and SAS 3 (Marshall & Clark 1984)). In the 1.5-keV band, the PSPC results agree with the HEAO-1 results to 1%, but with Wisconsin to only 7%; Snowden et al. attribute this to the Wisconsin calibration being off by this amount. In the $\frac{1}{4}$ keV band, the ROSAT fluxes appear consistently to be $\sim 10\%$ lower than the other three surveys'. We take the overall absolute calibration uncertainty to be 7%.

Adding these in quadrature along with the 2.3% error obtained in § 4.1.1 we obtain an overall systematic error estimate of 7.9%. Since the electron density is proportional to the square root of the x-ray flux, this is also the error in H_o due to the x-ray calibration.

4.1.3 Notes on Individual Clusters

Since galaxy clusters are not entirely uniform morphologically or spectrally, a few special cases are inevitable in the analysis of large data sets. Here we indicate special measures taken on the data sets of individual objects. Unless otherwise noted, the χ^2 values and significance levels are for fits with the absorbing column density fixed at the Galactic value and using bands R4–R7. Note that the clusters requiring additional soft components in the spectral fit were identified as requiring such on the basis of fits *including a* *free absorbing column density*, although (as indicated above) our final results all assume a column density fixed at Galactic.

- **A85:** The emission from an infalling group of galaxies to the south of the main cluster center was excised from the image prior to the extraction of spectra.

- **A399:** A399 and A401 lie within the same field of view separated by some $37'$. A401 was excised from the image (out to a radius of $25'$) prior to the spectrum extraction.

- **A401:** An excess soft component of emission over the best-fitting Raymond-Smith model is detected at the 3σ level. The best fitting single component model has $\chi^2_\nu = 7.8$, whereas allowing an additional soft (1 keV) component reduces this to $\chi^2_\nu = 2.7$. If we fit the spectrum to a two-phase model with a free absorbing column density, we obtain a value consistent with Galactic. We used the 2-component model and ignore the cool component obtained in the fit since it's contribution to the baryonic mass is very small. Similar results are obtained even if R2 is ignored in these fits. A399 was excised from the image out to a radius of $25'$ prior to the spectrum extraction.

- **A478:** A significant excess over the Galactic neutral hydrogen column density is observed; this is discussed in detail in § 4.1.1.

- **A1656:** The emission from an infalling group of galaxies to the south-west of the cluster was excised from the image prior to the extraction of spectra.

- **A2029:** A strongly spatially variable background is seen in both PSPC exposures of this field; the FOV also includes (just to the north of A2029) Abell 2033. Extended emission around and between these two clusters is clearly seen. Our beta-model fits to the spectra should not be significantly affected by this, but background spectrum subtractions using "blank" regions of the image should be employed with caution.

- **A3558:** A soft component of emission is required in the fit . A single-phase fit to the cluster as a whole with Galactic absorption gives $\chi^2_\nu = 11.1$ for 3 D.O.F. ; a two-component fit gives $\chi^2_\nu = 4.7$ for 2 D.O.F. and a soft component detected at the 5σ level. A3558 is at the center of the Shapley supercluster, with four other Abell clusters and several smaller clusters within a 2° radius. Significant emission over most of the field of view (particularly to the south-east) is clearly evident. Again, caution should be used in interpreting the results of background spectra obtained directly from the image.

- **A3571:** Located just over $4^\circ.3$ ($= 8.6h^{-1}$ Mpc) away from A3558, this cluster is at a similar redshift of $z \sim 0.04$ and appears also to be associated with the Shapley supercluster. There are some indications of extended emission in the field.

- **A3921:** A soft component is required in the fit.

Table 4.4 presents the 0.5–2.0 keV fluxes and (de-absorbed) luminosities which result from this analysis. Also shown are the 0.1–2.4 keV fluxes and luminosites.

Cluster	F_x $\mathrm{erg\,cm^{-2}\,s^{-1}}$ 0.5–2.0	L_x h^{-2} $\mathrm{erg\,s^{-1}}$ 0.5–2.0	F_x $\mathrm{erg\,cm^{-2}\,s^{-1}}$ 0.1–2.4	L_x h^{-2} $\mathrm{erg\,s^{-1}}$ 0.1–2.4
A85	4.49 ± 0.17	1.43 ± 0.05	6.01	2.31
A399	1.39 ± 0.05	1.10 ± 0.04	1.82	1.77
A401	2.57 ± 0.05	2.03 ± 0.08	3.35	3.28
A478	2.28 ± 0.08	3.62 ± 0.12	2.99	5.83
A754	4.22 ± 0.08	1.42 ± 0.03	5.67	2.28
A780	2.62 ± 0.11	0.89 ± 0.04	3.40	1.45
A1651	1.57 ± 0.03	1.20 ± 0.02	2.19	1.94
A1656	22.6 ± 0.2	1.38 ± 0.01	32.80	2.22
A1795	3.78 ± 0.11	1.59 ± 0.04	5.36	2.56
A2029	4.01 ± 0.14	2.76 ± 0.09	5.43	4.44
A2142	3.62 ± 0.04	3.51 ± 0.04	4.86	5.64
A2244	1.21 ± 0.04	1.32 ± 0.04	1.68	2.12
A2255	1.21 ± 0.02	0.89 ± 0.01	1.67	1.44
A2256	3.26 ± 0.04	1.44 ± 0.02	4.43	2.32
A2597	1.21 ± 0.08	1.03 ± 0.07	1.64	1.66
A3112	1.86 ± 0.03	1.07 ± 0.02	2.51	1.73
A3158	2.31 ± 0.05	0.89 ± 0.02	3.28	1.45
A3266	3.44 ± 0.04	1.17 ± 0.01	4.86	1.88
A3558	4.04 ± 0.12	1.13 ± 0.04	5.35	1.84
A3571	7.13 ± 0.09	1.34 ± 0.02	9.62	2.16
A3667	4.69 ± 0.06	1.76 ± 0.02	6.22	2.83
A3921	0.962 ± 0.06	1.04 ± 0.06	1.30	1.69

Table 4.4: Fluxes and luminosities for the clusters in our sample over the ROSAT bandpass. 0.1–2.4 keV results have fractional uncertainties comparable to those of the 0.5–2.0 keV results, but slightly larger due to the extrapolation in energy. Fluxes are as observed; luminosities are corrected for Galactic absorption (or, for A478, the best fit absorption model).

4.2 Spatial Analysis

We used the R4–R7 count rate images to determine the spatial profile of each cluster. The centroid of each image was computed in a circle centered on the visual peak of emission[1], and an azimuthal profile was constructed with 150 bins out to a radius equivalent to $1.5h^{-1}$ Mpc or $50'$, whichever was less. We found that our profile results were not sensitive to the number of bins we used. Error bars were assigned by performing an identical procedure on the co-added R4–R7 raw count images, and assigning the fractional Poisson error for each bin in the raw count profile (based on the total number of counts in that bin) to the corresponding bin in the count-rate profile.

The resulting profile was fit to a $\beta-$ model surface brightness profile:

$$I(\theta) = I_o \times (1 + \frac{\theta}{\theta_0})^{-3\beta+\frac{1}{2}}. \tag{4.2}$$

In cases where a good fit could not be obtained for a $\beta-$model, we added a Gaussian component of emission to the profile. In these fits, θ_0, β, I_o, and the central intensity and width of the Gaussian were all free parameters. A free constant background term was also included. We found that an extra Gaussian component was only needed in cases where a cooling flow was observed by Markevitch et al.

In order to check that our fitting procedure was not getting stuck in local minima, we mapped the χ^2 space (in θ_0, β with the background and Gaussian parameters fixed at the best fit values) for each cluster. This resulted in minor adjustments (at the 5% level) to the best-fit parameters for 6 clusters. For all but one cluster (A1656) the resulting value was consistent within the errors given by our simulations (§ 4.3). As an illustration of the correlation between the β–model parameters, Figure 4.4 shows the contours of constant $\Delta\chi^2$ ($\Delta\chi^2 = 1$, 2, and 3) for A2256.

For clusters containing a central cooling-flow, we also performed fits with the central $150h^{-1}$ kpc excised. In general, we find that the outer data prefer slightly steeper profiles than fits to the data as a whole. This was undertaken in order to more accurately characterize the slope of the profile in the outer parts of the cluster, since we found that the central emission

[1]The only exception to this was A754, where we varied the center used for the azimuthal average until a good $\beta-$model fit could be obtained. The resulting centroid is $\alpha = 137^\circ.314, \delta = -9^\circ.674$ (J2000). The uncertainty induced by this procedure will be accounted for in our Monte-Carlo simulations (§ 4.3)

often drives β in cooling flow clusters even for fits that include an extra Gaussian component. Since the separate parameters in these fits are not generally very well constrained, we do not attempt to map χ^2. In § 4.3 we will find that our results for the baryonic mass and SZE are not sensitive to the particular profile assumed in any case. This will not be the case for the total mass.

The results of this analysis will be presented in § 4.4.

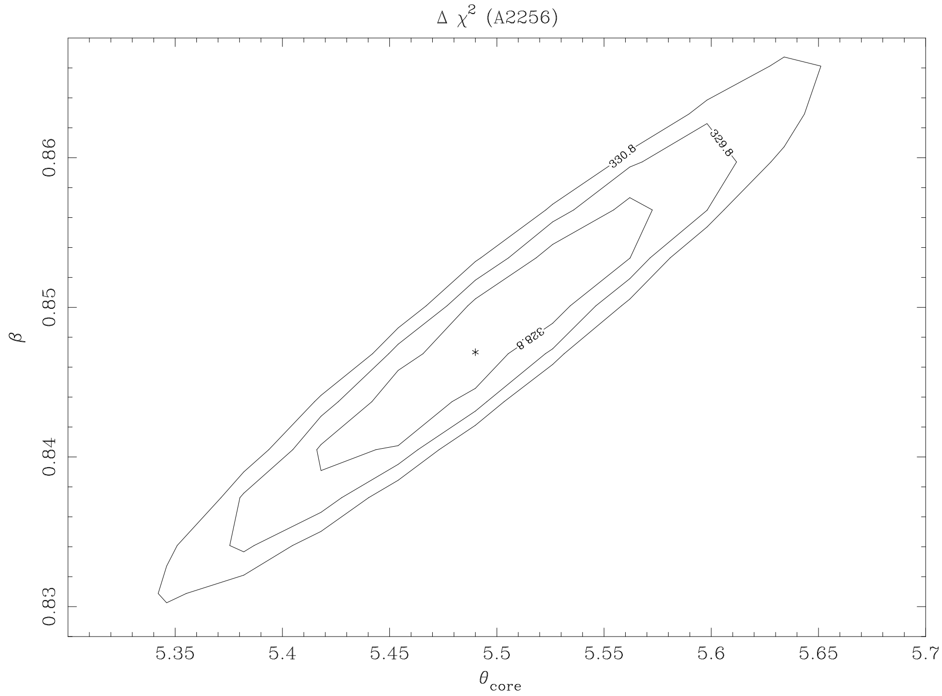

Figure 4.4: Contours of constant $\Delta\chi^2$ ($\Delta\chi^2 = 1$, 2, and 3) for a β–model fit to the azimuthal profile of A2256. The minimum of χ^2 is indicated by "*".

4.3 Assessment of Errors

In order to quantitatively assess the uncertainties and potential systematic errors in our results, we undertook an extensive suite of Monte-Carlo simulations. This is particularly important for the case at hand because the parameters of our profile fits (θ_0, β) are found to be highly correlated. Since these parameters are used (see Equation 2.15) to compute the central density, and then in turn used in conjunction with this density to infer baryonic masses and the SZ decrement, standard Gaussian propagation of uncorrelated errors will give essentially meaningless results. Furthermore, there are several potential sources of error, such as departures from the $\beta-$model and errors in the centroid used for the azimuthal profile, which will cause standard relative likelihood analyses (e.g.,$\Delta\chi^2$) applied to the cluster profiles to underestimate the parameter uncertainties.

The focus of this was two-fold: first, we sought to understand how some particular systematic effects, if present, would bias our profile fits. We accomplished this by taking an ideal $\beta-$model and corrupting it in various specific ways, adding Poisson noise[2], computing the azimuthal averages, then fitting $\beta-$models to the resulting profile. Second, we sought to understand how deviations from the idealized $\beta-$model present in the real data affected the accuracy of our results. For this, we used smoothed template maps (which will be discussed in detail below) of the actual data to generate simulated observations which were then analyzed as described in § 4.2. This generates the distribution of (θ_0, β) values which we use to state confidence intervals on our best-fit model parameters. Together with the overall flux uncertainties we obtain from our spectral analysis we can quantitatively set confidence limits on the masses, baryon fractions, and SZ decrements that result from our analysis.

For the systematic error study, we used a fiducial model with $\theta_0 = 5.0'$, $\beta = 0.720$, and a central "intensity" of 50.0 counts per pixel. This is characteristic of a short ($\sim$ 8 ksec) exposure of a merger cluster in our sample. We studied 2 specific sources of systematic error: the effects of imperfect background removal, and the effects of errors in the vignetting correction. The background removal is of some concern because, while we represent the background as a constant, the backgrounds which ESAS subtracts out are

[2]By "adding Poisson noise" we mean, throughout the discussion, creating instances of a given image of the *mean number of expected counts* which obey Poisson statistics.

clearly spatially variable and thus any residuals from this subtraction will also be spatially variable. In each case, a 2-D template image with the fiducial model was created and corrupted as appropriate. 10^4 instantiations of this map were generated including Poisson noise; these images were then azimuthally averaged and fit to $\beta-$models. For the background study, the corruption consisted of adding 10% of the actual background which ESAS subtracted from the A85 A data set to the image (scaled to an 8 ksec observation) along with a constant background of 0.05 counts/pixel, which is typical. For the vignetting studies, the template image was multiplied by a quadratic with a value of 1.0 on-axis, and having a value of 0.9 or 1.1 at the edge of the PSPC field of view. A constant background of 0.05 counts/pixel was also added to the image prior to the vignetting corruption to represent the cosmic background. In all three cases the average β–model parameters were affected by less than 0.1%. This implies not only that our *profile* parameters are insensitive to these potential sources of systematic error, but also that our (β–model-derived) *spectra* are unaffected by them at this level. The insensitivity of our derived parameters to the addition of a variable background can be understood in light of the fact that while the instrumental backgrounds are not in general constant, neither are they correlated with a β–model. The insensitivity of our results to the vignetting correction is simply due to the fact that this correction matters most in the outer wings of the azimuthal profile, which primarily drive the constant term in the fit.

We also used these simulations to quantify the error in the total number of counts inferred by fitting a $\beta-$ model to the data. We find that the fractional error in the total number of counts N is well represented by:

$$\frac{\epsilon_N}{N} = \sqrt{\frac{2}{N}} \tag{4.3}$$

for the given background levels.

To study the effects of deviations from the ideal β–model, the 0.5–2.0 keV (R4–R7) count rate images for the longest exposure on each cluster were smoothed with a $30''$ FWHM Gaussian. 10^3 simulated observations were created by multiplying the smoothed count rate image by the averaged R4–R7 exposure maps calculated by ESAS and adding Poisson noise. Each instantiation was then subjected to an automated analysis designed as much as possible to mimic our actual data reduction. Exposure and point source masks were applied to the data, and the centroid computed within a circular aperture with a radius randomly varying between $2'$ and $30'$. The center of this circle was taken to be the centroid we determined by hand (§ 4.2). The azimuthal profile was computed about this centroid and fit to a model as described in § 4.2 . For clusters on which we had chosen to perform fits to the exterior data, we also evaluated these fits using the same method.

The resulting distribution of parameters was used to evaluate the 68% confidence intervals for θ_0, β, and the baryonic and total masses for each cluster. See Chapter 2, § 2.1 for the formulae used to compute total and baryonic mass. In addition, we computed the distribution of 5.5-meter and ACBAR beam-averaged optical depths for each cluster; see Chapter 2, § 2.3 for descriptions of these experiments and the optical depth formalism. The uncertainty in the 5.5-meter beam characterization has been included in these calculations. Note that in doing so, the prefactor Ω_{Beam}^{-1} is held constant, since this factor is eventually cancelled in the ratio with the *observed* temperature decrement. Failure to do this will result in erroneously low estimates of the uncertainty, since the beam-averaged surface brightness of an extended object is less sensitive to the assumed beam width than the flux density.

In addition to all of this, there is the crucial issue of *model choice*. The Monte-Carlo technique assumes at the outset some parametric model for the cluster profile, which is then fit to multiple fake data sets. If the given parametric model is just not a good choice, the confidence intervals derived from the Monte Carlo simulations will not reflect this fact. To deal with this, we have chosen alternate models for a number of clusters. The models we analyze are tabulated in Table 4.5.

Our findings will be discussed in § 4.4.

Model	θ_0	β	θ_{cut}	Notes
A85	2.04	0.600	3.62	$N_{comp} = 2$ fit to all; center excised from spectrum.
A85.2	5.42	0.779	3.62	$N_{comp} = 1$ fit to outer; center excised from spectrum.
A399	4.33	0.742	0	$N_{comp} = 1$ fit to all; all included in spectrum.
A401	2.26	0.636	0	$N_{comp} = 1$ fit to all; all included in spectrum.
A478	1.00	0.638	2.22	$N_{comp} = 2$ fit to all; center excised from spectrum.
A478.2	1.58	0.683	2.22	$N_{comp} = 1$ fit to outer; center excised from spectrum.
A754	5.50	0.713	0	$N_{comp} = 1$ fit to all; all included in spectrum.
A780	1.64	0.629	3.60	$N_{comp} = 2$ fit to all; center excised from spectrum.
A1651	2.16	0.712	2.39	$N_{comp} = 2$ fit to all; center excised from spectrum.
A1651.2	1.86	0.690	2.39	$N_{comp} = 1$ fit to outer; center excised from spectrum.
A1656	9.32	0.670	0	$N_{comp} = 1$ fit to all; center excised from spectrum.
A1656.2	8.78	0.632	0	same — alternate profile.
A1795	2.17	0.698	3.10	$N_{comp} = 2$ fit to all; center excised from spectrum.
A1795.2	2.98	0.750	3.10	$N_{comp} = 1$ fit to outer; center excised from spectrum.
A2029	0.93	0.601	2.55	$N_{comp} = 2$ fit to all; center excised from spectrum.
A2029.2	2.09	0.667	2.55	$N_{comp} = 1$ fit to outer; center excised from spectrum.
A2142	1.60	0.635	2.22	$N_{comp} = 2$ fit to all; center excised from spectrum.
A2142.2	1.91	0.655	2.22	$N_{comp} = 1$ fit to outer; center excised from spectrum.
A2244	0.82	0.580	0	$N_{comp} = 1$ fit to all; all included in spectrum.
A2255	4.36	0.723	0	$N_{comp} = 1$ fit to all; all included in spectrum.
A2256	5.49	0.847	0	$N_{comp} = 1$ fit to all; all included in spectrum.
A2597	0.49	0.626	2.33	$N_{comp} = 2$ fit to all; center excised from spectrum.
A2597.2	1.61	0.693	2.33	$N_{comp} = 1$ fit to outer; center excised from spectrum.
A3112	0.52	0.560	2.75	$N_{comp} = 1$ fit to all; center excised from spectrum.
A3112.2	1.24	0.590	2.75	$N_{comp} = 1$ fit to outer; center excised from spectrum.
A3158	2.84	0.649	0	$N_{comp} = 1$ fit to all; all included in spectrum.
A3266	8.50	0.942	0	$N_{comp} = 1$ fit to all; all included in spectrum.
A3558	2.66	0.55	0	$N_{comp} = 1$ fit to all; all included in spectrum.
A3571	3.64	0.669	4.6	$N_{comp} = 2$ fit to all; center excised from spectrum.
A3571.2	4.35	0.702	4.6	$N_{comp} = 1$ fit to outer; center excised from spectrum.
A3667	4.29	0.589	0	$N_{comp} = 1$ fit to all; all included in spectrum.
A3921	1.33	0.541	0	$N_{comp} = 1$ fit to all; all included in spectrum.

Table 4.5: Enumeration of models employed in the analysis.

4.4 Results

The means and 68% confidence intervals for the profile parameters, baryonic masses, total masses, and mass fractions for the 22 clusters in our sample are summarized in Tables 4.6, 4.8, and 4.9. For clusters on which we had chosen to do fits to the outer data also, confidence intervals for these profile parameters are also shown (Table 4.6). As we discuss below, where possible the parameter distributions for the fits to the outer data were used to calculate the *total* mass and its associated confidence interval. The baryonic masses were calculated using the parameter distributions for the single or double component fits to all of the data, as appropriate. Tables 4.8 and 4.9 quote baryonic masses, total masses, and mass fractions within two radii: a fixed metric radius, chosen to be $500\,h^{-1}$ kpc, and a radius related to the cluster virial mass. For the latter, we chose to use the scaling relation of Mohr et al. (1999) :

$$R_{500} = 1.185\,h^{-1}\,\mathrm{Mpc}\,\times\left(\frac{T_e}{10\,\mathrm{keV}}\right)^{\frac{1}{2}}. \tag{4.4}$$

This is the radius within which the density contrast is 500, normalized by the Mohr et al. (1999) mass model for A1795. This allows us to compare physically similar regions of each cluster, as well as comparing our analysis with that of Mohr et al. For clusters in our sample, this corresponds to a metric radius of about $1\pm0.05\,h^{-1}$ Mpc. Our chosen metric radius of $500h^{-1}$ kpc also allows comparison with most of the literature, as most investigators quote results within 1 Mpc with $h = 0.5$.

In the following, we discuss in detail the results of the spatial profile analysis (§ 4.4.1), the baryonic mass and SZE predictions (§ 4.4.2), and the total mass and baryon fraction measurements (§ 4.4.3).

4.4.1 Spatial Analysis

We see in Table 4.6 that considered separately, θ_0 is typically constrained at the 10% – 25 % level, and β is determined to $\sim$ 5% or better within the context of a given model. Since the baryonic mass (and the SZE) are proportional to θ_0^3, naively using Gaussian propagation of errors to compute the error on these quantities would result in estimates of 30% to 75%. This is clearly a gross overestimate, as the baryonic masses and SZE predictions are constrained to 5% or better. We indicated previously that this is due to the fact that the parameters $(n_{eo}, \beta, \theta_0)$ are all highly correlated/degenerate. To further illustrate this point, Figure 4.7 shows the distribution of core radii and derived baryonic masses derived in our Monte Carlo fits to the outer data on A2142. In this case, the core radius varies by a factor of 6, while the calculated baryonic mass varies by only $\pm 5\%$! This underscores the fact that there are no "true" values of θ_0 and β for any given cluster, just value pairs which jointly provide more or less reasonable fits over some range of radii.

For the cooling flow clusters in our sample, we performed fits both to all of the data with a free component to represent the cooling flow, and to the outer data. We generally do not find that the β model parameters for these two methods are consistent. This reflects the fact that while the β model may be a good description of the ICM over a moderate range of radii, it is not necessarily a good description when extrapolated to the outermost regions. In fact, a comparison of the β values in Table 4.6 shows that the fits to the outer data consistently show a steeper slope than either of the fits to the profile as a whole. To examine the effect of this on the total mass estimates more carefully, we define the quantity β_{eff} as

$$\beta_{eff}(\theta) = \beta \frac{\theta^2/\theta_0^2}{1+\theta^2/\theta_0^2}, \tag{4.5}$$

or minus one third the logarithmic derivative of the density profile. This is proportional to the total mass which is inferred under the assumption of HSE at the given radius, and contains all of the profile-dependence of this mass. Table 4.7 shows the value of β_{eff} at $1\,h^{-1}$ Mpc for a representative sample of clusters with smooth, regular surface brightness profiles. We show results for three models of the cluster: a single β model fit to the entire cluster (model A)[3], a 2-component fit to the entire cluster (model B), and a single β model fit to the outer cluster data (model C). In Figures 4.5 and 4.6 we show the 2-component and 1-component fits to all of the data and the outer data (respectively) for A85, the cluster showing the largest discrepancies between the methods. There is a clear systematic tendency for the single β model fits to *underestimate* the slope of the density profile at large radii; these models will consequently underestimate the total mass also. The two-component fits to the entire cluster emission, while less affected than the single β model fits, are somewhat biased also. For this reason, we employ the fits to the outer data in deriving total masses for the cooling flow clusters in our sample. The

[3]Since the $30''$ smoothing employed in our Monte Carlo analysis biases single β model fits to cooling flow clusters, we do not quote confidence intervals for these fits.

non-cooling-flow clusters do not contain the strongly peaked central surface brightness which biases fits to the cooling flow clusters, so for these clusters, we use single β model fits to the entire cluster profile for the total mass calculation. The steepening of cluster baryon profiles at large radius has been noted before by Neumann & Arnaud (1999) and Vikhlinin et al. (1999) in the analysis of ROSAT PSPC data on nearby clusters. Navarro et al. (1995) have seen similar effects in simulations of galaxy clusters.

As our comparative model analysis illustrates (see Table 4.10), the level of precision we achieve in modeling the outer gas slope is more than sufficient for purposes of calculating the SZE. For very precise estimates of the cluster mass and its uncertainties at large radii, however, more careful analysis of the profiles may be called for. Since this involves characterizing the derivative of the observable in a region of low signal-to-noise data, it could be a challenging exercise.

		All Emission		Outer Emission	
Cluster	N_{comp}	θ_0 ($'$)	β	θ_0 ($'$)	β
A85	2	2.04 ± 0.52	0.60 ± 0.05	5.42 ± 0.38	0.779 ± 0.025
A399	1	4.33 ± 0.45	0.742 ± 0.042	—	—
A401	1	2.26 ± 0.41	0.636 ± 0.047	—	—
AA478	2	1.00 ± 0.15	0.638 ± 0.014	1.58 ± 0.20	0.683 ± 0.011
A754	1	5.50 ± 1.10	0.713 ± 0.120	—	—
A780	2	1.64 ± 0.38	0.629 ± 0.028	0.90 ± 0.33	0.640 ± 0.007
A1651	2	2.16 ± 0.36	0.712 ± 0.036	1.86 ± 0.34	0.690 ± 0.020
A1656	1	9.32 ± 0.10	0.670 ± 0.003	—	—
A1795	2	2.17 ± 0.28	0.698 ± 0.017	2.98 ± 0.20	0.750 ± 0.011
A2029	2	0.93 ± 0.09	0.601 ± 0.030	2.09 ± 0.36	0.667 ± 0.016
A2142	2	1.60 ± 0.12	0.635 ± 0.012	1.91 ± 0.60	0.655 ± 0.030
A2244	1	0.82 ± 0.14	0.580 ± 0.018	—	—
A2255	1	4.36 ± 0.12	0.723 ± 0.015	—	—
A2256	1	5.49 ± 0.21	0.847 ± 0.024	—	—
A2597	1	0.49 ± 0.03	0.626 ± 0.018	1.61 ± 0.52	0.693 ± 0.022
A3112	1	0.52 ± 0.05	0.560 ± 0.008	1.24 ± 0.49	0.590 ± 0.017
A3158	1	2.84 ± 0.16	0.649 ± 0.018	—	—
A3266	1	8.50 ± 0.27	0.942 ± 0.020	—	—
A3558	1	2.66 ± 0.07	0.55 ± 0.006	—	—
A3571	2	3.64 ± 0.18	0.669 ± 0.009	4.35 ± 0.50	0.702 ± 0.020
A3667	1	4.29 ± 0.96	0.589 ± 0.051	—	—
A3921	1	1.33 ± 0.23	0.541 ± 0.031	—	—

Table 4.6: Best-fit profiles and uncertainties for 22 clusters using 1– or 2–component fits to all cluster emission, and (where applicable) 1–component fits to the cluster emission excluding the inner 150 h^{-1} kpc.

Cluster	β_{eff}		
	A	B	C
A85	0.54	0.60 ± 0.05	0.74 ± 0.02
A478	0.61	0.64 ± 0.01	0.67 ± 0.01
A780	0.59	0.63 ± 0.03	0.63 ± 0.01
A1651	0.62	0.70 ± 0.03	0.68 ± 0.02
A1795	0.60	0.69 ± 0.01	0.73 ± 0.01
A2029	0.58	0.60 ± 0.01	0.66 ± 0.02
A2142	0.60	0.63 ± 0.01	0.65 ± 0.02

Table 4.7: β_{eff} as a function of model choice for 7 representative cooling flow clusters in our sample. β_{eff} has been evaluated at $1\,h^{-1}$ Mpc in each case. "A" is a single β model fit to all data; "B" is a two-component fit to all data; and "C" is a β model fit to the outer data only.

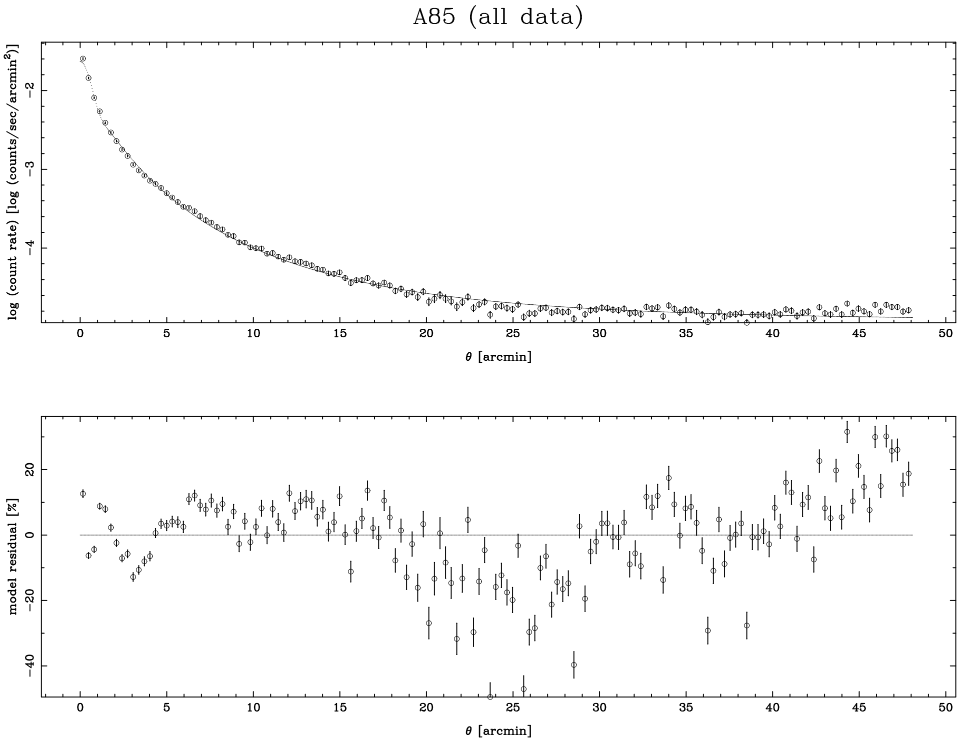

Figure 4.5: β plus Gaussian fit to the entire A85 surface brightness profile. $1\,h^{-1}$ Mpc is at $24'.2$ for this cluster.

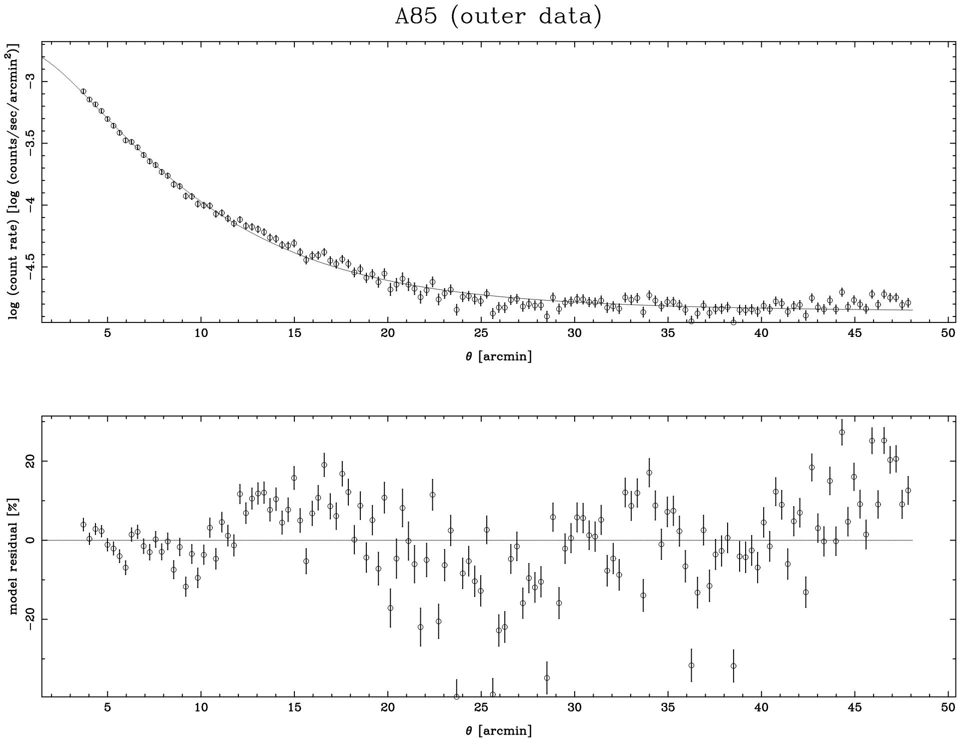

Figure 4.6: β model fit to the A85 surface brightness profile with the inner region excised.1 h^{-1} Mpc is at $24'.2$ in this figure.

4.4.2 Baryonic Masses and SZE

As indicated in the previous section, the baryonic masses in these clusters are typically constrained at the 5% level. These results do *not* depend strongly on the modeling strategy we choose for any particular cluster. This is due to the fact that the ROSAT PSPC data, insensitive as they are to temperature gradients, more or less directly constrain the density profile of the cluster gas, and thus any profile which gives a reasonable fit to the x-ray surface brightness profile will result in a similar physical density profile. The sensitivity of the baryonic masses we infer to the chosen modeling strategy is further reduced by the fact that the baryonic mass is proportional to the square root of the integral of the observable (the surface brightness profile). Consequently even moderately significant systematic tendencies in the model residuals will not strongly affect the baryonic masses we calculate. There is no evidence for such effects in our data (see the profiles in Appendix A). To illustrate the insensitivity of the baryon masses to model choice, we show (Figure 4.8) the baryonic mass profiles for three very different models of A478. These models show excellent agreement inside $1\,h^{-1}$Mpc; outside this, the models which include the inner emission tend to overestimate the mass slightly due to the effects noted in § 4.4.1. Figure 4.7, which was indicated previously, shows the total baryonic mass within $1\,h^{-1}$ Mpc as a function of core radius for 10^3 Monte Carlo fits to A2142.

Since the SZE in an isothermal cluster is proportional to the total baryonic mass times T_e, it should come as no surprise that the SZE predictions show accuracies comparable to the baryonic mass calculations. Table 4.10 shows the central optical depths for inverse Compton scattering, as well as the beam-averaged values for the 5.5-meter and ACBAR. Where alternate cluster models have been attempted (mostly for the cooling-flow clusters; see Table 4.5) we present the optical depths for these models also. In no case does the alternate model differ from the primary (adopted) model at a statistically significant level. These results have accuracies ranging from $\sim 1-10\%$. The uncertainties in the 5.5-meter optical depths are significantly larger than the ACBAR results because we have included the uncertainty in Ω_{Beam} in the former calculations. For the larger clusters (such as Coma), this dominates the error bar. The less accurate results are on clusters which either are highly irregular in shape, such as A754, or those which are large compared to the 5.5-meter beam, such as A754, A3266, and Coma. The central optical depths are typically $\sim 5\times10^{-3}$, and the switched, beam-averaged

5.5-m optical depths are $\sim 2.5 \times 10^{-3}$. For these calculations, we used the 5.5-meter beam parameters given in Table 6.2; for ACBAR, a Gaussian beam with a FWHM of $4'$ was assumed.

In analogy with Figure 4.7, we show in Figure 4.9 the predicted 5.5-m SZE as a function of θ_0 for 10^3 Monte-Carlo fits to the smoothed A2142 x-ray profile which exclude the cooling region. A similar result is found: the standard deviation of y_{sw} over a distribution of models encompassing a factor of six in core radius is only 2.3%. A careful comparison of these two figures shows that while the overall scatter is slightly larger in the SZE predictions, the scatter at a *given* value of θ_0 is somewhat less. This is because the noise in β is suppressed somewhat in the switched SZE predictions. For a fixed x-ray flux, reducing β reduces the predicted central decrement by reducing the baryonic surface mass density; at the same time, this reduction reduces the flux in the 5.5-meter REF beams, thereby increasing the switched decrement and cancelling some of the reduction due to the lesser central decrement. A similar effect will be seen when we examine hybrid isothermal/adiabatic temperature profiles in Chapter 6.

Mohr et al. (1999) have also analyzed public ROSAT data on 20 of the 22 clusters on which we present results here (they do not include A3921 or A399). Although the Mohr et al. analysis focuses on the determination of masses and mass fractions in these clusters— as opposed to the focus here which is on SZE predictions— a comparison of the baryonic masses we find with those found by Mohr et al. provides a good cross-check for possible systematic errors in either of these analyses. Figure 4.10 shows the Mohr et al. ICM masses at $500\,h^{-1}$ kpc versus the masses we find in our analysis. The overall agreement is excellent: the mean mass ratio ($M_{ICM,Mohr}/M_{ICM,this\,work}$) is 1.007 ± 0.016 (S.D. = 7%), strongly arguing against any systematic differences in our analyses. One of the most significant outliers (A478) is largely due to the fact that Mohr et al. do not correct for the excess absorption over the Galactic value; the effect of applying this correction is shown by an arrow in the figure. A754 has the least well-constrained baryonic mass by far due to the high degree of substructure in the plane of the sky, and this cluster is also labeled in the figure. However, the scatter is significantly larger than what we might expect based on our estimated precision (see § 4.1.2). Adding in quadrature our 2.9% repeatability estimate to the 2.3% uncertainty due to the interpretation of the x-ray spectrum, we find a 3.7% x-ray flux uncertainty, which translates into 1.8% in the baryonic mass. If the Mohr et al. mass for A478 is corrected for the observed excess neutral Hydrogen absorption, the standard deviation in the mass ratio goes down to 6%, which is still just over three times our estimated precision. This could be due to our differing treatment of cooling flows, different spectral extraction procedures and point-source masking, etc. In any case there is no significant systematic offset between these analyses, and the observed dispersion will average down in a reasonably-sized sample of clusters. Since these two analyses were conducted completely independently (using separate spectral extractions, count rate to flux conversions, and flux to density conversions), this comparison gives us great confidence in our results.

Finally, our best fit baryon models are summarized in Table 4.11. Due to the parameter degeneracies noted throughout this thesis, it is important to use the parameters listed in Table 4.11 and not, for instance, the distribution mean for n_{eo} from Table 4.8 together with the β and θ_0 from Table 4.6. The values for τ_0 shown in Table 4.11 are model normalizations and are *not* necessarily representative of the actual central inverse Compton optical depth which would be observed in very high resolution SZ maps.

Cluster	M_{Bary} ($10^{13}\,h^{-5/2}$ M$_\odot$)	M_{tot} ($10^{14}\,h^{-1}$ M$_\odot$)	f ($h^{-3/2}$ %)	n_{eo} ($10^{-3}\,h^{1/2}\,\mathrm{cm}^{-3}$)
A85 (500 h^{-1} kpc)	1.27 ± 0.07	$2.26^{+0.18}_{-0.23}$	5.61 ± 0.21	$11.14^{+2.54}_{-1.98}$
($R_{500} = 0.99h^{-1}$ Mpc)	3.20 ± 0.07	5.66 ± 0.27	5.67 ± 0.24	—
A399 (500 h^{-1} kpc)	1.33 ± 0.02	2.34 ± 0.10	5.71 ± 0.20	$3.24^{+0.14}_{-0.19}$
($R_{500} = 0.99h^{-1}$ Mpc)	3.51 ± 0.08	5.36 ± 0.32	6.55 ± 0.32	—
A401 (500 h^{-1} kpc)	1.67 ± 0.05	$2.64^{+0.18}_{-0.11}$	6.35 ± 0.23	$8.01^{+0.56}_{-1.02}$
($R_{500} = 1.06h^{-1}$ Mpc)	4.64 ± 0.14	$5.86^{+0.50}_{-0.32}$	$7.94^{+0.44}_{-0.62}$	—
A478 (500 h^{-1} kpc)	2.01 ± 0.03	$2.92^{+0.18}_{-0.33}$	$6.91^{+0.69}_{-0.40}$	$28.9^{+15.2}_{-3.9}$
($R_{500} = 1.08h^{-1}$ Mpc)	5.17 ± 0.25	$6.81^{+0.49}_{-0.78}$	$7.60^{+0.76}_{-0.45}$	—
A754 (500 h^{-1} kpc)	$1.56^{+0.10}_{-0.17}$	$3.09^{+0.36}_{-0.48}$	5.07 ± 0.26	$3.73^{+0.07}_{-0.1}$
($R_{500} = 1.15h^{-1}$ Mpc)	5.15 ± 0.24	$8.30^{+1.41}_{-1.82}$	$6.21^{+1.81}_{-1.23}$	—
A780 (500 h^{-1} kpc)	$0.870^{+0.014}_{-0.053}$	$1.47^{+0.09}_{-0.19}$	5.91 ± 0.36	$12.90^{+18.0}_{-2.97}$
($R_{500} = 0.77h^{-1}$ Mpc)	1.50 ± 0.05	2.35 ± 0.15	6.41 ± 0.36	—
A1651 (500 h^{-1} kpc)	1.31 ± 0.02	$2.09^{+0.10}_{-0.19}$	6.27 ± 0.28	$7.47^{+5.17}_{-0.96}$
($R_{500} = 0.92h^{-1}$ Mpc)	2.79 ± 0.07	4.29 ± 0.22	6.53 ± 0.30	—
A1656 (500 h^{-1} kpc)	1.44 ± 0.01	2.99 ± 0.14	4.82 ± 0.21	4.51 ± 0.04
($R_{500} = 1.13h^{-1}$ Mpc)	4.48 ± 0.12	7.41 ± 0.41	6.03 ± 0.28	—
A1795 (500 h^{-1} kpc)	1.34 ± 0.01	2.89 ± 0.24	4.66 ± 0.35	$11.29^{+0.61}_{-1.77}$
($R_{500} = 1.04h^{-1}$ Mpc)	3.16 ± 0.14	6.63 ± 0.61	4.77 ± 0.36	—
A2029 (500 h^{-1} kpc)	1.77 ± 0.02	3.00 ± 0.22	5.90 ± 0.38	$31.11^{+7.94}_{-6.40}$
($R_{500} = 1.13h^{-1}$ Mpc)	5.01 ± 0.21	7.48 ± 0.62	6.70 ± 0.46	—
A2142 (500 h^{-1} kpc)	2.38 ± 0.02	$3.25^{+0.32}_{-0.24}$	$7.30^{+0.49}_{-0.67}$	$15.03^{+0.92}_{-1.07}$
($R_{500} = 1.16h^{-1}$ Mpc)	7.19 ± 0.37	$8.08^{+0.95}_{-0.73}$	$8.90^{+0.64}_{-0.91}$	—

Table 4.8: Central densities, total masses, and baryon fractions for 11 clusters at $500h^{-1}$ kpc and R_{500}. Quoted densities are the mean for the distribution, *not* the value corresponding to our quoted best-fit model.

Cluster	M_{Bary} ($10^{13}\,h^{-5/2}$ M$_\odot$)	M_{tot} ($10^{14}\,h^{-1}$ M$_\odot$)	f ($h^{-3/2}$ %)	n_{eo} ($10^{-3}\,h^{1/2}$ cm^{-3})
A2244 (500 h^{-1} kpc)	1.31 ± 0.03	$2.25^{+0.48}_{-0.30}$	$5.84^{+0.73}_{-1.16}$	$17.73^{+1.95}_{-2.65}$
($R_{500} = 0.99h^{-1}$ Mpc)	3.33 ± 0.37	$4.51^{+1.04}_{-0.73}$	$7.39^{+0.97}_{-1.49}$	—
A2255 (500 h^{-1} kpc)	$1.23 + 0.01$	$2.27^{+0.34}_{-0.22}$	$5.41^{+0.48}_{-0.73}$	2.52 ± 0.03
($R_{500} = 1.01h^{1}$ Mpc)	3.54 ± 0.26	$5.51^{+0.90}_{-0.65}$	$6.43^{+0.58}_{-0.89}$	—
A2256 (500 h^{-1} kpc)	1.62 ± 0.01	$2.44 + 0.10$	6.61 ± 0.24	$4.08^{+0.09}_{-0.06}$
($R_{500} = 0.96h^{-1}$ Mpc)	3.79 ± 0.08	5.53 ± 0.27	6.83 ± 0.30	—
A2597 (500 h^{-1} kpc)	0.902 ± 0.025	$1.52^{+0.10}_{-0.16}$	$5.96^{+0.56}_{-0.34}$	$45.13^{+2.81}_{-4.75}$
($R_{500} = 0.78h^{-1}$ Mpc)	1.53 ± 0.07	$2.60^{+0.19}_{-0.29}$	$5.91^{+0.57}_{-0.36}$	—
A3112 (500 h^{-1} kpc)	0.974 ± 0.017	$1.64^{+0.14}_{-0.20}$	$5.95^{+0.66}_{-0.46}$	$38.38^{+2.30}_{-2.90}$
($R_{500} = 0.86h^{-1}$ Mpc)	2.03 ± 0.13	$2.96^{+0.29}_{-0.39}$	$6.84^{+0.78}_{-0.56}$	—
A3158 (500 h^{-1} kpc)	1.16 ± 0.02	$1.65^{+0.07}_{-0.09}$	$7.06^{+0.26}_{-0.21}$	5.54 ± 0.24
($R_{500} = 0.88h^{-1}$ Mpc)	2.50 ± 0.06	$3.38^{+0.17}_{-0.19}$	$7.38^{+0.35}_{-0.31}$	—
A3266 (500 h^{-1} kpc)	1.54 ± 0.01	2.55 ± 0.10	6.06 ± 0.22	2.49 ± 0.05
($R_{500} = 1.06h^{-1}$ Mpc)	4.69 ± 0.10	7.72 ± 0.37	6.08 ± 0.23	—
A3558 (500 h^{-1} kpc)	1.12 ± 0.02	1.60 ± 0.08	7.00 ± 0.32	5.71 ± 0.14
($R_{500} = 0.88h^{-1}$ Mpc)	2.63 ± 0.10	2.89 ± 0.15	9.12 ± 0.42	—
A3571 (500 h^{-1} kpc)	1.42 ± 0.01	2.42 ± 0.05	5.86 ± 0.10	$8.59^{+0.17}_{-0.24}$
($R_{500} = 0.98h^{-1}$ Mpc)	3.33 ± 0.04	5.15 ± 0.16	6.48 ± 0.17	—
A3667 (500 h^{-1} kpc)	1.54 ± 0.05	2.00 ± 0.13	7.73 ± 0.39	4.00 ± 0.57
($R_{500} = 0.99h^{-1}$ Mpc)	4.61 ± 0.21	4.35 ± 0.45	10.58 ± 0.79	—
A3921 (500 h^{-1} kpc)	1.11 ± 0.05	1.82 ± 0.30	6.11 ± 0.92	$6.25^{+0.92}_{-0.70}$
($R_{500} = 0.94h^{-1}$ Mpc)	2.90 ± 0.34	3.50 ± 0.65	8.30 ± 1.32	—

Table 4.9: Central densities, total masses, and baryon fractions for 11 clusters at $500h^{-1}$ kpc and R_{500}.

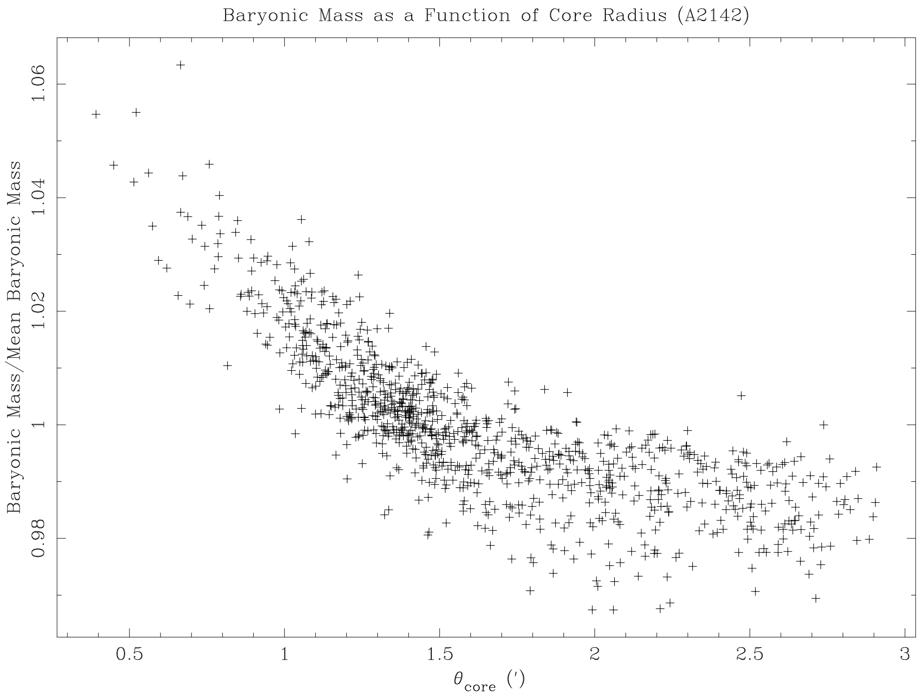

Figure 4.7: Baryonic Mass within $500h^{-1}$ kpc as a function of core radius for fits to A2142 excluding the inner $150h^{-1}$ kpc. The standard deviation of this distribution is 1.3%.

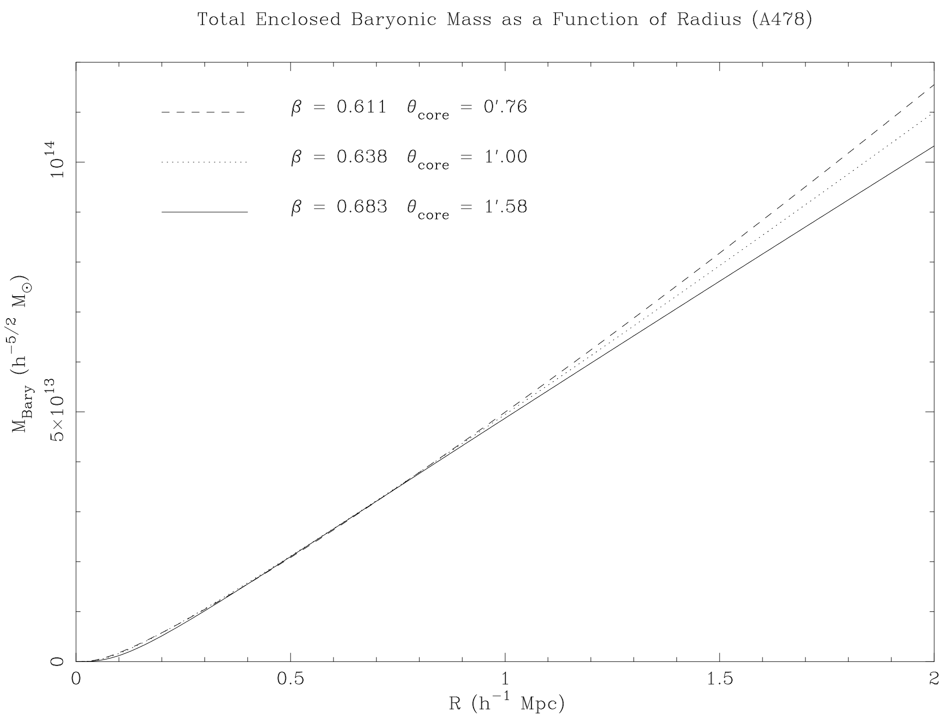

Figure 4.8: Baryon Mass as a function of radius for three different models of A478, illustrating the insensitivity of the inferred baryonic mass upon the chosen model. The central densities for these models were chosen to give the observed x-ray emission measure from $150\,h^{-1}$ kpc to $1.5\,h^{-1}$ Mpc.

Cluster		5.5-meter		ACBAR
	τ_o $(10^{-3}\,h^{-1/2})$	τ_{beam} $(10^{-3}\,h^{-1/2})$	τ_{sw} $(10^{-3}\,h^{-1/2})$	τ_{beam} $(10^{-3}\,h^{-1/2})$
A85	6.60 ± 0.48	3.81 ± 0.22	2.88 ± 0.23	4.94 ± 0.12
(A85.2)	4.72 ± 0.14	3.45 ± 0.09	2.76 ± 0.13	—
A399	4.34 ± 0.28	3.08 ± 0.17	2.50 ± 0.13	3.77 ± 0.05
A401	6.96 ± 0.55	4.15 ± 0.24	3.17 ± 0.18	5.34 ± 0.13
A478	12.93 ± 1.17	4.39 ± 0.20	3.68 ± 0.15	6.59 ± 0.12
(A478.2)	—	4.22 ± 0.22	3.61 ± 0.17	—
A754	5.20 ± 0.37	4.16 ± 0.27	3.02 ± 0.31	4.77 ± 0.09
A780	$5.49^{+1.18}_{-0.54}$	2.62 ± 0.13	2.11 ± 0.11	3.61 ± 0.05
A1651	$5.75^{+0.80}_{-0.51}$	2.84 ± 0.15	2.44 ± 0.11	$3.98^{+0.20}_{-0.09}$
(A1651.2)	6.06 ± 0.84	2.88 ± 0.12	2.47 ± 0.11	4.07 ± 0.23
A1656	5.22 ± 0.36	4.77 ± 0.30	2.76 ± 0.16	5.07 ± 0.02
(A1656.2)	—	4.56 ± 0.30	2.64 ± 0.15	5.06 ± 0.02
A1795	6.88 ± 0.54	3.49 ± 0.17	2.95 ± 0.13	$4.84^{+0.08}_{-0.12}$
(A1795.2)	5.94 ± 0.29	3.37 ± 0.11	2.88 ± 0.10	—
A2029	12.13 ± 1.31	4.37 ± 0.20	3.52 ± 0.14	6.34 ± 0.10
(A2029.2)	8.09 ± 1.51	4.09 ± 0.19	3.37 ± 0.17	—
A2142	11.11 ± 0.09	5.28 ± 0.26	4.28 ± 0.18	7.33 ± 0.06
(A2142.2)	—	5.19 ± 0.30	4.25 ± 0.22	—
A2244	8.16 ± 0.64	2.93 ± 0.15	2.30 ± 0.11	4.20 ± 0.07
A2255	3.89 ± 0.27	2.81 ± 0.15	2.23 ± 0.11	3.40 ± 0.03
A2256	5.13 ± 0.36	3.77 ± 0.20	3.19 ± 0.16	4.54 ± 0.03
A2597	9.86 ± 0.75	2.05 ± 0.10	1.74 ± 0.09	3.26 ± 0.09
A3112	9.04 ± 0.65	2.62 ± 0.13	2.06 ± 0.10	3.82 ± 0.06
(A3112.2)	$6.32^{+2.11}_{-1.34}$	2.58 ± 0.13	2.05 ± 0.14	—
A3158	4.88 ± 0.34	3.11 ± 0.16	2.43 ± 0.12	3.95 ± 0.43
A3266	4.30 ± 0.30	3.56 ± 0.20	2.89 ± 0.16	4.03 ± 0.03
A3558	5.07 ± 0.36	3.59 ± 0.20	2.39 ± 0.13	4.31 ± 0.08
A3571	6.46 ± 0.47	4.52 ± 0.25	3.49 ± 0.17	5.54 ± 0.10
(A3571.2)	6.01 ± 0.29	4.39 ± 0.16	3.41 ± 0.14	—
A3667	5.60 ± 0.46	4.52 ± 0.28	2.95 ± 0.17	5.18 ± 0.17
A3921	5.75 ± 0.41	3.06 ± 0.16	2.18 ± 0.12	3.98 ± 0.04

Table 4.10: Central and beam-averaged optical depths for 22 clusters. The 5.5-meter beam-averaged optical depths include the uncertainties due to the main beam determination. All quoted τ values are the means of the observed distributions, *not* the values corresponding to our best-fit models. The models are defined in Table 4.5.

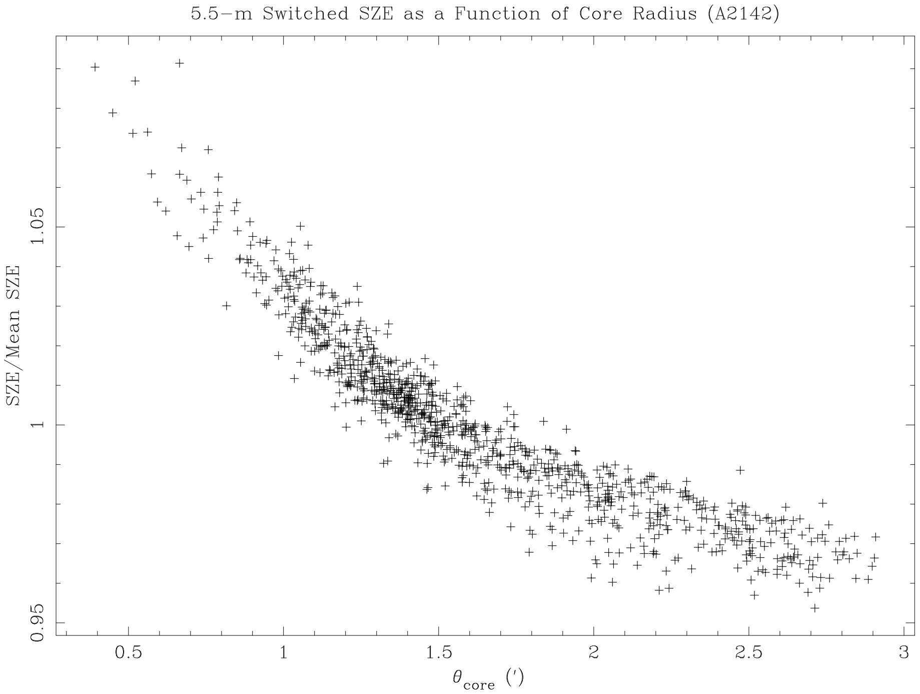

Figure 4.9: Switched 5.5-m SZE as a function of core radius for fits to A2142 excluding the inner $150h^{-1}$ kpc. The standard deviation in this distribution (which excludes the uncertainty in Ω_{Beam} for the 5.5-m) is 2.3%.

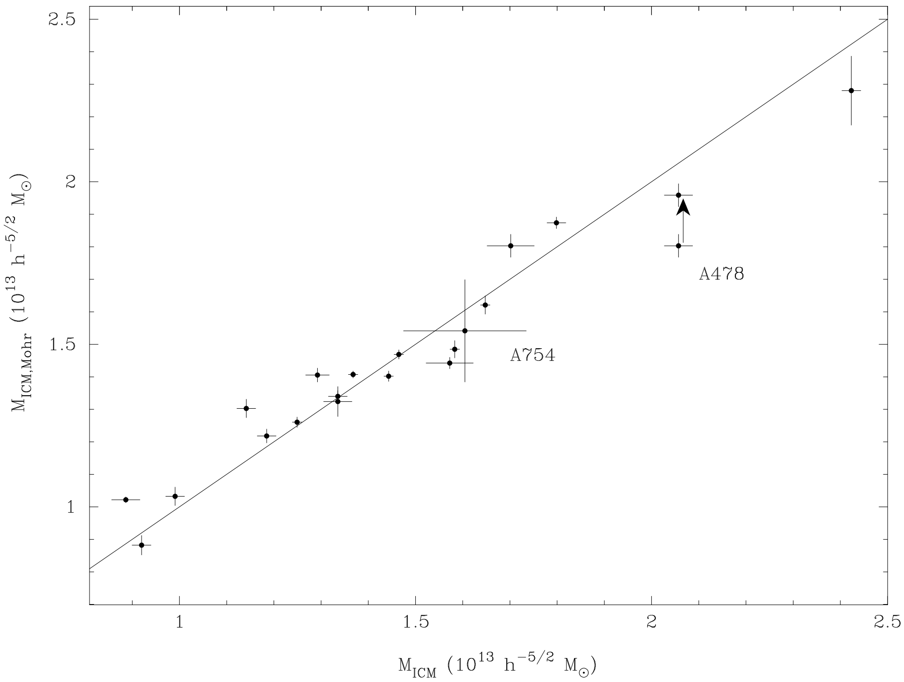

Figure 4.10: A comparison of the ICM masses obtained by Mohr et al. (1999) and in this analysis for 20 of our 22 clusters. Masses are evaluated at $500\,h^{-1}$ kpc. The arrow shows the effect of correcting the Mohr et al. mass for the observed excess neutral hydrogen absorption.

Cluster	θ_0 ($'$)	R_0 (h^{-1} kpc)	β	n_{eo} ($10^{-3}\,h^{1/2}\,\mathrm{cm}^{-3}$)	τ_o ($10^{-3}\,h^{-1/2}$)
A85	2.04	84.4	0.600	10.44	6.59
A399	4.33	239	0.742	3.23	4.34
A401	2.26	130.	0.636	7.90	7.05
A478	1.00	67.5	0.638	27.81	12.84
A754	5.50	232	0.713	3.81	5.20
A780	1.64	68.3	0.629	11.30	5.38
A1651	2.16	135	0.712	7.14	5.70
A1656	9.32	181	0.670	4.52	5.23
A1795	2.17	105	0.698	10.70	6.81
A2029	0.930	54.7	0.601	29.35	11.99
A2142	1.60	108	0.635	14.95	11.10
A2244	0.820	59.5	0.580	17.30	8.13
A2255	4.36	266	0.723	2.53	3.89
A2256	5.49	260	0.847	4.08	5.13
A2597	0.49	31.7	0.626	44.64	9.90
A3112	0.52	28.3	0.56	38.12	9.02
A3158	2.84	132	0.649	5.52	4.88
A3266	8.50	398	0.942	2.49	4.30
A3558	2.66	103	0.55	5.71	5.07
A3571	3.64	118	0.669	8.57	6.46
A3667	4.29	188	0.589	3.92	5.68
A3921	1.33	94.9	0.541	6.18	5.20

Table 4.11: Summary of best-fit models and the central densities and optical depths for these models.

4.4.3 Total Masses and Baryon Fractions

The total masses and baryon fractions we find for these 22 clusters are tabulated in Tables 4.8 and 4.9. The mean baryon fraction within $500\,h^{-1}$ kpc is found to be $(6.09 \pm 0.17)\,h^{-3/2}\,\%$ (s.d. $= 0.78\,h^{-3/2}\,\%$); within R_{500}, it is $(7.02 \pm 0.28)\,h^{-3/2}\,\%$ (s.d. $= 1.32\,h^{-3/2}\,\%$). For $h = 0.5$, these are $(17.3 \pm 0.47)\%$ and $(19.8 \pm 0.8)\%$ respectively. These are consistent with the $10\% - 20\%$ baryon fractions observed (inside $1\,h^{-1}$ Mpc with $h = 0.5$) by White & Fabian (1995) in analyses of Einstein IPC data on galaxy clusters. Our results are also in good agreement with those of Mohr et al. (1999), who find baryon fractions of $\sim 21\%$ within R_{500} for an analysis of the 44 clusters in the Edge sample with ROSAT PSPC data. For $h \sim 0.7$ our data are also in agreement with gas mass fractions determined by Grego (1998) on the basis of interferometric observations of more distant clusters. In a sample of 14 clusters, they find a gas mass fraction of $7.1^{+1.0}_{-1.1}\,h^{-1}\,\%$ within R_{500} (at 68% confidence).

As we emphasized in § 4.4.1, the total masses and baryonic mass fractions that result from our analysis are somewhat less robust than the baryon masses and SZE predictions due to clear systematic effects in the profile modeling. This is evident in a comparison of Figure 4.11 and Figure 4.8, which show the baryon fraction and baryonic mass as a function of radius for 3 models of A478. We have tried to account for the systematic biases by deriving total masses from fits to the outer data only for those clusters for which the bias is most severe. In addition, the total mass calculation, unlike the baryonic mass calculation, depends on the validity of our assumptions of isothermality and hydrostatic equilibrium on the scales of interest. Departures from the assumed situation (e.g., large-scale adiabatic inflows, declining temperature gradients, or magnetic pressure) will tend to cause isothermal hydrostatic models to underestimate the total mass. Evrard et al. (1996) find that isothermal β model estimates of the total mass in numerically simulated clusters on scales of $R_{500} - R_{2000}$ are unbiased and accurate to $\sim 15\%$ on average, suggesting that the strategy we adopt is not likely to be seriously in error; only future observations, however, will really allow the cluster physics at these large radii to be unambiguously understood.

We will discuss the significance of these findings in Chapter 7.

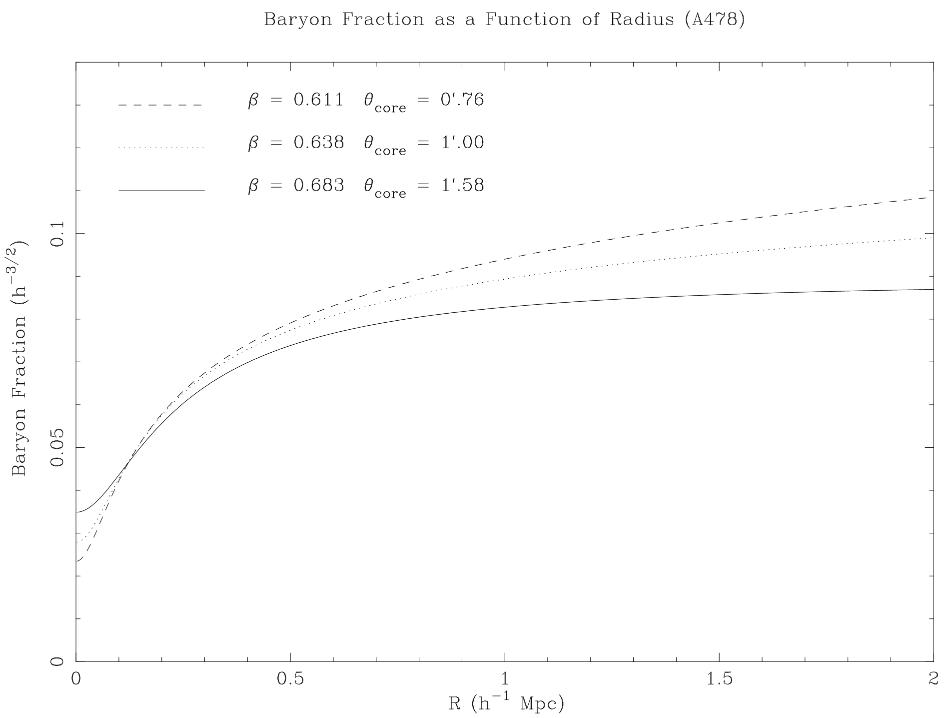

Figure 4.11: Baryon Fraction as a function of radius for three different models of A85, illustrating the sensitivity to model choice. The central densities for these models were chosen to give the observed x-ray emission measure from $150\,h^{-1}$ kpc to $1.5\,h^{-1}$ Mpc.

Chapter 5

Absolute Calibration

Absolute flux density calibration is an important issue for all astronomical observations. Most absolute calibration efforts have occurred at lower frequencies ($\lesssim$ 10 GHz) since it is easier to measure the far-field properties of antennas in this regime, or to use feed systems of calculable gain. See, for example, Conway et al. (1963), Kellermann (1964), Kellermann et al. (1969), Baars et al. (1977) and references therein. Most of these flux density scales are based upon measurements of the supernova remnant Cassiopeia A (Cas A) with horn-type or dipole antennas. At higher frequencies this endeavor is substantially more difficult, and investigators have often used flux densities extrapolated from low frequencies or computed from theoretical models of celestial sources. One exception is the work of Wrixon et al. (1971) who measured the brightness temperature of Jupiter at frequencies between 20.5 and 33.5 GHz with a 20 foot antenna at the Hat Creek observatory; this telescope was calibrated with a far-field transmission/reception measurement. This measurement was the basis of the calibration used for the SZE measurements of Myers et al. (1997) , but given the relatively large (5.5%) uncertainty in Wrixon's T_J it is desirable to improve upon this. This paper presents an *absolute* measurement with an accuracy of 3% of the flux density of Cas A at 32 GHz, a calibrator commonly used at all frequencies and the second brightest extra-solar source in the sky in our observing band.

While absolute calibration is an important consideration for many different types of experiments, our calibration efforts were undertaken with the particular intent of supporting the intrinsic CMB and Sunyaev-Zeldovich programs at the Owens Valley Radio Observatory (OVRO) and other similar observations. Absolute calibration is a particular concern for Sunyaev-Zeldovich studies since the error in the quantity of interest (H_o) is proportional to twice the calibration error. It is of great importance that the calibrations of intrinsic CMB anisotropy experiments be as accurate as possible in order to place more stringent limits on the parameters of cosmology. Several published CMB experiments use Cas A as their primary calibrator, such as the Saskatoon experiment (Netterfield et al., 1996) and CAT (Scott et al., 1996). These experiments typically have calibration uncertainties $\gtrsim 10\%$. It is important to reduce these uncertainties as much as possible and to use a single flux density scale at or near 32 GHz. This affects a number of experiments including the RING5M (Leitch et al. 1999), MAT (Torbet et al. 1999; Miller et al. 1999), QMAP (Devlin et al. 1998), CBI (Readhead et al. 1999), DASI (White et al. 1999) and the VSA (Jones & Scott 1998).

The 1.5-m telescope used in the present observations was originally designed and constructed by JPL as part of the Deep Space Network (DSN) program. The telescope has a parabolic primary reflector with an off-axis secondary and a dual feed horn, and a Dicke-switching receiver at the Cassegrain focus. To establish absolute gain standards for DSN, the National Institute of Standards and Technology (NIST) was employed to measure the aperture efficiency of the 1.5-m antenna; these measurements are discussed in § 5.1. OVRO obtained the instrument in 1993, and our current calibration program commenced in 1996, with efforts focused on characterizing the receiver and reworking the telescope control code. Most of the useful astronomical observations were taken during the spring of 1998 (from early March through the end of May).

We selected Cassiopeia A ($\alpha = 23^{\rm h}23^{\rm m}26^{\rm s}.920$, $\delta = +58^\circ 49' 07''.50$, J2000) as our primary calibration source because of its brightness and accessibility from the latitude of the observatory. Observations of other calibrator sources relative to Cas A were carried out in the fall of 1998, as well as during epochs previous to our absolute measurements, allowing the determination of absolute flux densities for these sources as well.

In the following, we first present a brief description of the NIST calibration measurements (§ 5.1) and our own characterization of the instrument (§ 5.2); following this is a summary of observations taken at OVRO in the spring of 1998 (§ 5.3), and a detailed discussion of our error budget (§ 5.4). Next we describe observations of 3C48, 3C147, 3C286, Jupiter, Mars, Saturn and other sources on the OVRO 5.5-meter telescope relative to Cas A, employing our absolute value for S_{cas} (§ 5.5). Finally we summarize our findings and compare them to the results of other flux density scales (§ 5.6).

5.1 Antenna Characterization: NIST Measurements

Flux density, S_ν, is related to the spectral power, P_ν, by

$$P_\nu = A_{eff}(\nu) \times S_\nu, \tag{5.1}$$

where $A_{eff}(\nu)$ is the *effective area* of the telescope. A_{eff} is always less than the geometrical area of the telescope for a well-designed system due to effects such as diffraction at the edge of the dish, surface irregularities, scattering off of the secondary support structure (not a problem for unblocked apertures such as this one), and slight impedance mismatches. The most difficult aspect of most absolute flux density measurements at high frequency is the accurate assessment of A_{eff}.

It can be shown from elementary thermodynamic considerations (e.g. Rohlfs & Wilson 1996; Krauss 1986) that

$$\Omega_{Ant} \times A_{eff} = \lambda^2 \tag{5.2}$$

where λ is the wavelength of the incident radiation and

$$\Omega_{Ant} = \iint d\phi \, d(\cos\theta) P_{Ant}(\theta, \phi). \tag{5.3}$$

Here $P_{Ant}(\theta, \phi)$ is the response function of the antenna normalized to one at the maximum. If we define the *gain*, g, of a telescope in a given direction as the ratio of P_{Ant} in that direction to the mean value of P_{Ant} on the sphere, then it can be shown that

$$g|_{max} = \frac{4\pi}{\Omega_{Ant}}. \tag{5.4}$$

Since g is a ratio, it is often expressed in decibels (dBi, or decibels above the isotropic level implied by the spherical average).

It is convenient to express spectral power in terms of the *antenna temperature* T_{Ant}, defined as the temperature a beam-filling blackbody would need to have (in the Rayleigh-Jeans limit) in order to produce the observed spectral power. The antenna system may then be characterized by the Kelvin per flux density unit *sensitivity*, Γ:

$$\Gamma = \frac{\lambda^2}{8\pi k} \times g|_{max}. \tag{5.5}$$

Numerically, this is

$$\Gamma = 0.362 \times \frac{A_{eff}}{\text{meters}^2}\frac{\text{mK}}{\text{Jy}}. \tag{5.6}$$

In the far-field of a given antenna, these properties (Γ , A_{eff}, Ω_{Ant}) are independent of distance. The far-field is conventionally defined to be the distance at which the phase variation (across the aperture of the antenna) of an electric field originating at a point at distance r_{ff} is less than $22^\circ.5$; this criterion yields a beam pattern which is, to a good approximation, independent of the distance of the illuminating source from the antenna. For a flat aperture the given phase constraint results in $r_{\mathit{ff}} > 2D^2/\lambda$.

Since for many telescopes the far-field is inconveniently far away, the direct measurement of far-field antenna characteristics often requires measurements to be made over long distances outside of a controlled laboratory setting. In this context, bore sighting, ground reflections and atmospheric attenuation are all difficult issues to deal with. Extensive work has consequently been done at NIST and elsewhere to develop near-field techniques to measure the far-field power pattern and gain of antennas; this work and the theory behind it is summarized in Baird et al. (1988), Lo & Lee (1993), Newell et al. (1988), and Rahmat-Samii (1993). The technique employs a measurement of the near-field electric field of the antenna; the resulting field distribution (after correcting for the probe antenna characteristics) is related to the far-field electric field by a Fourier transform. Ranged measurements are used to fit out mutual coupling terms due to imperfect impedance matching between the target and probe antennas (Lo & Lee 1993; Francis et al. 1990); the probe gains themselves are determined using a three-antenna technique (Lo & Lee 1993). In May of 1990, our telescope was characterized at NIST's near field test range in Boulder, Colorado (National Institute of Standards and Technology 1990). The compactness of the antenna permitted this procedure to be carried out without disassembling the instrument for shipping, greatly reducing uncertainties which may otherwise arise due to the relative displacement of the various optical components of the system; for more discussion of this point, see § 5.4. NIST assigns a 1.4% (1σ) systematic error to this measurement in the calibration report; this uncertainty is dominated by the determination of the probe antenna gain and normalization amplitude. As discussed in § 5.2, the 1.5-meter is outfitted with a Dicke-switching receiver with two horns. The gains of these horns were separately measured; we designate them the ANT and REF horns. The NIST

ν (GHz)	g (dBi)	g (10^5)	A_{eff} (m^2)	η_A	G (mK/Jy)
31.8 (ANT)	52.54 ± 0.06	1.795	1.270	71.9%	0.460 ± 0.006
32.0 (ANT)	53.04 ± 0.06	2.014	1.407	79.6%	0.509 ± 0.007
32.0 (REF)	52.96 ± 0.06	1.977	1.381	78.1%	0.500 ± 0.007
32.3 (ANT)	53.32 ± 0.06	2.148	1.472	83.3%	0.533 ± 0.007

Table 5.1: NIST antenna gain measurements

gains, however, are referred to the *back* of the feed horns. This implies that the stated gains include the effects of ohmic losses in the feeds, whereas our calibration procedure effectively removes these (by measuring antenna temperatures referred to the front of the feeds). This is something that we will have to account for in our final systematic error budget.

The ANT beam gain was measured at 31.8, 32.0 and 32.3 GHz ; the REF beam gain was only measured at 32.0 GHz. These measurements are summarized in Table 5.1. Note that the measured gains at the band edges differ by 13.6%; while the nominal receiver bandpass is 3 GHz, it is clear that the extrapolation of the observed gains to 30.5 and 33.5 GHz will introduce a very large uncertainty. Furthermore, the REF beam was only characterized at the band center. For these reasons an additional filter was introduced into the signal path, reducing our system bandpass to 500 MHz centered on 32.0 GHz (see § 5.2). We therefore adopt the mean of the ANT and REF beam gains at 32.0 GHz, $g = (1.995 \pm 0.028) \times 10^5$ (53.00 ± 0.06 dBi), corresponding to $\Omega_{Ant} = (6.298 \pm 0.088) \times 10^{-5}$ Sr, $A_{eff} = (1.394 \pm 0.020)\,\mathrm{meters}^2$ and $\Gamma = (0.505 \pm 0.007)\frac{\mathrm{mK}}{\mathrm{Jy}}$. Assuming a geometrical area of $1.77\,\mathrm{meters}^2$, this yields an aperture efficiency of $(78.8 \pm 1.1)\%$. The average of the ANT and REF gains is the appropriate quantity to use in the context of our double-differenced FLUX procedure (see § 5.3).

NIST also measured the beam patterns of both ANT and REF beams; the beams were found to be well-described by Gaussians of $25'.8 \pm 0'.6$ FWHM, corresponding to $\sigma = 10'.96 \pm 0'.25$. Integrating a Gaussian of this width out to the radius of the first measured nulls in the real beam pattern (at $\pm 24'.0$), we compute $\Omega_{Beam} = (5.80 \pm 0.26) \times 10^{-5}$ Sr and a beam efficiency of

$$\begin{aligned} \eta_{Beam} &= \frac{\Omega_{main}}{\Omega_{Ant}} \\ &= 87.0 \pm 4.8\%. \end{aligned}$$

The beam throw was measured to be $1^\circ.00 \pm 0^\circ.01$, with a $0^\circ.02 \pm 0^\circ.1$

($= EL_{ANT} - EL_{REF}$) elevation offset. The relatively high beam and aperture efficiencies demonstrate the efficacy of the clear-aperture design and small, stiff primary dish.

It is likely that the 1.8% difference between the ANT and the REF gains is due to a slight impedance mismatch on the REF side of the signal chain; NIST measured the return loss on the REF horn to be several dB lower than that on the ANT horn. This could be due to differential isolation in the Dicke switch.

5.2 Receiver Characterization and Antenna Temperature Calibration

5.2.1 Receiver and Backend

The receiver is a standard Dicke-switching two-horn receiver. Celestial signals enter the receiver via these two scalar feeds (uncooled) and pass into the 15 K dewar where right circular polarization is selected. A cross-guide coupler before the Dicke-switch permits the injection of a calibration (cal) signal. The Dicke-switch itself operated at 1 kHz during observations, providing alternating 0.5 msec "integrations" against each feed. The switched signal is amplified by a HEMT (+28 dB of gain), the last component in the 15 K dewar. The 15 K cryogenic stage displayed remarkable stability from fall 1996 through spring 1998. The 15 K dewar is enclosed in a dewar which is maintained at ~ 70 K. On entering this stage, the RF passes first through an Avantek amplifier (second stage, +22 dB) and then through a double-sideband mixer, which converts the signal down to a 0 to 1.5 GHz IF. Before leaving the dewar, the IF is amplified and passed through a 1.5 GHz low-pass filter. A block diagram of the receiver is shown in Figure 5.1.

The IF signal is piped via coaxial cable to a climate-controlled trailer where the detection and post-detection signal processing is carried out. For the reasons detailed in § 5.1, detection of the full band power is undesirable, so this signal was passed through a 250 MHz low-pass filter, giving a system bandpass of 500 MHz on the sky; the resulting signal is split, half going to a diode detector, which feeds a Lock-in-Amplifier (LIA) for the detection of switched power, and half going to an HP 437B power meter for detection of total power. In order to boost the IF signal well above the lowest levels that the LIA was capable of detecting, another IF amplifier (+17 dB of gain) was inserted in the signal chain after the coaxial cable and before the final low-pass filter. Figures 5.2 and 5.3 show the broad and narrow-band detection setups used in observations. Only the narrow-band configuration was employed for absolute calibration measurements; we record the broad band setup for historical completeness, and since our pointing observations were derived with this setup (which gives a higher signal to noise ratio).

The linearities of the power meter power head and diode detector were assessed by measuring the cal signal increment with an ambient-temperature microwave absorber placed in front of the feed-horns and varying the attenuation prior to the powerhead and detector. As an example, Figure 5.4 shows the cal diode signal (as a total power increment) as a fraction of the system power at a range of power levels. Power levels in the back end were chosen to put the detector in the middle of its optimally linear regime ($\sim -29\,\mathrm{dBm}$). Consequently the diode detector's departures from linearity over the dynamic range encountered in observations is less than 0.1%; the power head's deviation is less than 0.2%. These elements are thus not significant sources of nonlinearity. The receiver on the other hand is somewhat nonlinear, which is discussed in § 5.2.3.

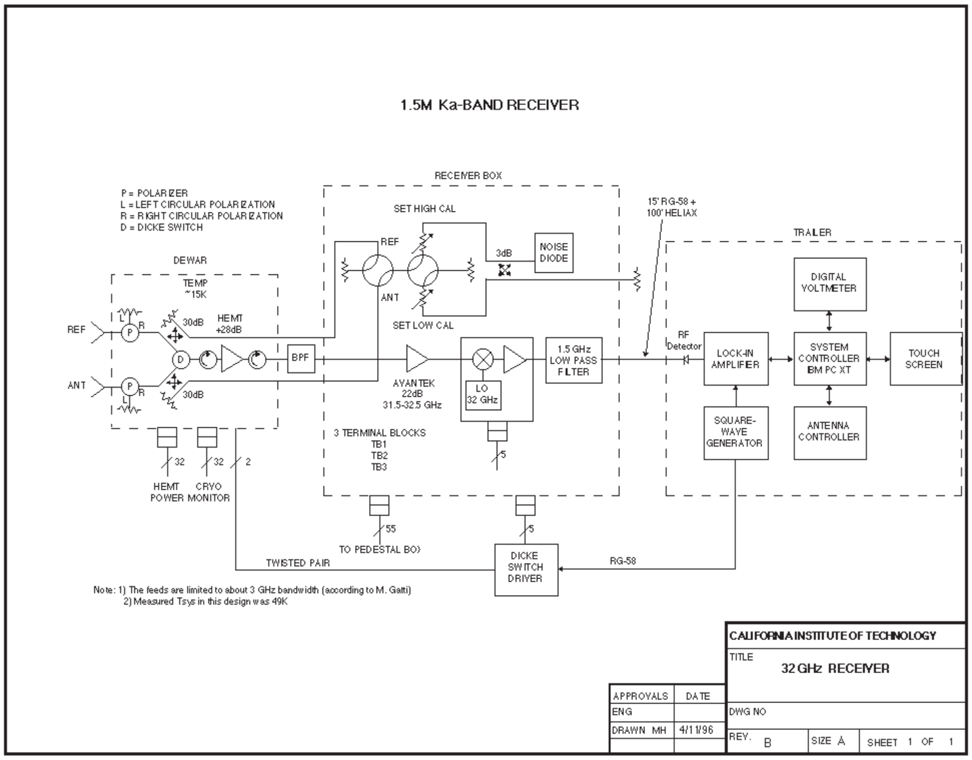

Figure 5.1: A block diagram of the 1.5-m Ka-band receiver, along with the IF detection and control schemes employed by JPL. The receiver itself remains unaltered; our methods for detection and control are considerably improved (see text).

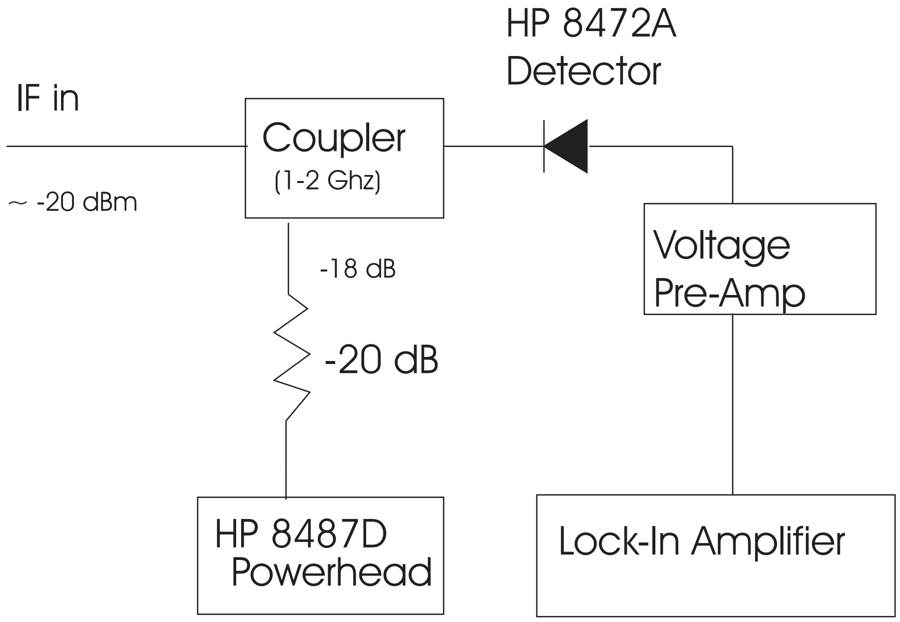

Figure 5.2: A block diagram of our initial (broadband) IF detection setup. Note that since the coupler is only effective over 1-2 GHz, the overall 0-1.5 GHz coupling turns out to be somewhat less than -10 dB ($\sim$ -18 dB)

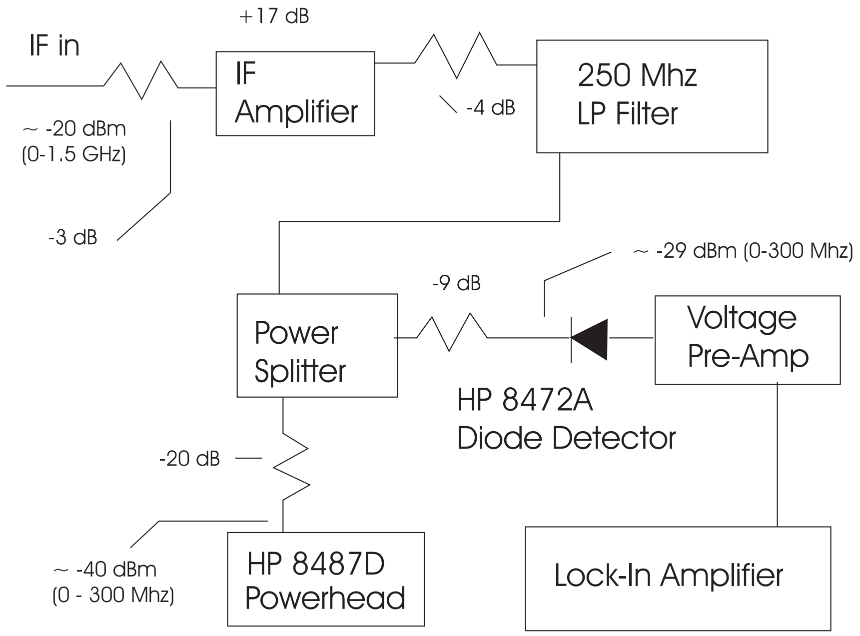

Figure 5.3: A block diagram of the final narrow-band IF detection setup used in calibration observations.

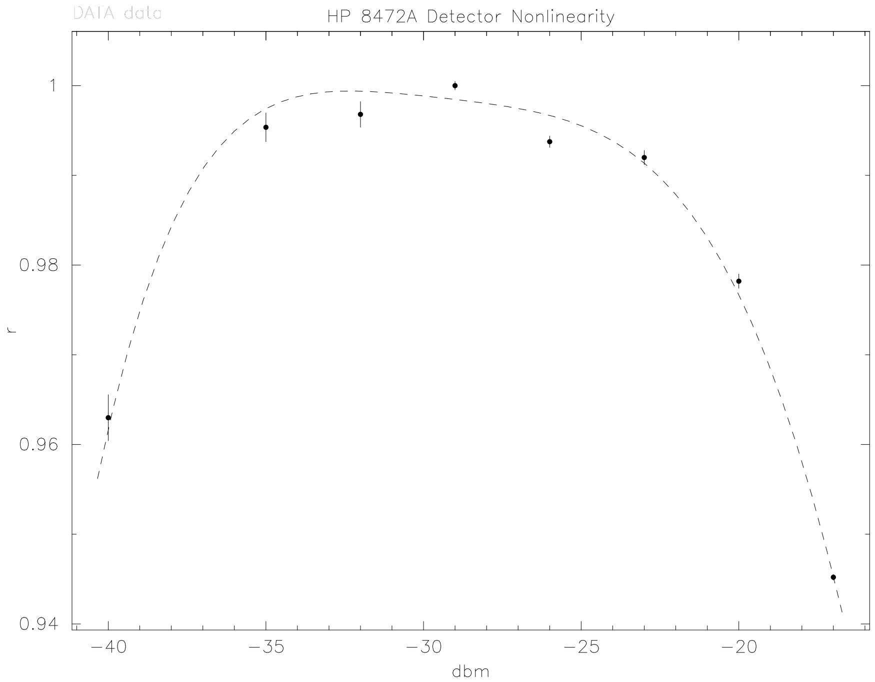

Figure 5.4: Measurement of the diode linearity. The CAL diode switched power is shown as a function of total power at the detector; the switched power is normalized to 1 at -29 dBm. Note the fairly significant departure from square-law behavior up to ~ -25 dBm. The detector total power level during calibration observations was ~ -29 dBm.

5.2.2 Dicke Switch Isolation

Measurements with a Dicke-switching receiver must in general be corrected for the finite isolation of the Dicke switch. Let ξ be the isolation of the Dicke switch, defined as the fraction of incident power leaked from the input port to the second output port in the direction of circulation; we take ξ to be the same in either direction of circulation. The difference of two successive measurements of *total* power from the first output port in the direction of circulation with the cal on and off is then

$$P_{cal} = (1 - \xi) \times P_{cal,true}. \tag{5.7}$$

A *switched* observation of the CAL diode, on the other hand, yields

$$P_{cal,sw} = (1 - 2\xi) \times P_{cal,true}. \tag{5.8}$$

Since celestial signals are attenuated by the same factor, this cancels out when we calibrate the data, and the switched power observations thus care about $P_{cal,true}$. Consequently, the observed CAL diode temperatures must be multiplied by $(1 - \xi)^{-1} \sim (1 + \xi)$ to yield the correct brightness temperature.

The Dicke switch isolation was measured by locking the switch onto the ANT feed while repeatedly firing the cal signal into the REF feed. In 112 pairs of on/off averages of the system power, a mean fractional increase in the system temperature of $(5.7 \pm 1.3) \times 10^{-4}$ was observed. These tests were conducted against an external cold load for stability. Assuming $T_{RX} = 55\,\mathrm{K} + 77\,\mathrm{K} = 132\,\mathrm{K}$ and $T_{cal} = 14.34\,\mathrm{K}$ (see below) , this implies a leakage of $0.54 \pm 0.11\%$ of the cal signal. This is equivalent to an isolation of -22.7 ± 0.9 dB. Any effects such as losses or a finite duty cycle in the Dicke switch do not affect our results as they will affect celestial observations and observations of our calibration loads in the same fashion (see below).

Although the receiver design incorporates several mechanical waveguide switches which permit some degree of control over the magnitude of the cal diode signal, these switches were not exercised *at any point* during or between our calibration measurements and observations. This precaution was deemed necessary due to the possibility that the switches might not toggle between two precisely defined impedance states, which would cause the apparent cal signal brightness to change. The receiver does not have any variable attenuators, which would have to be calibrated at a number of settings.

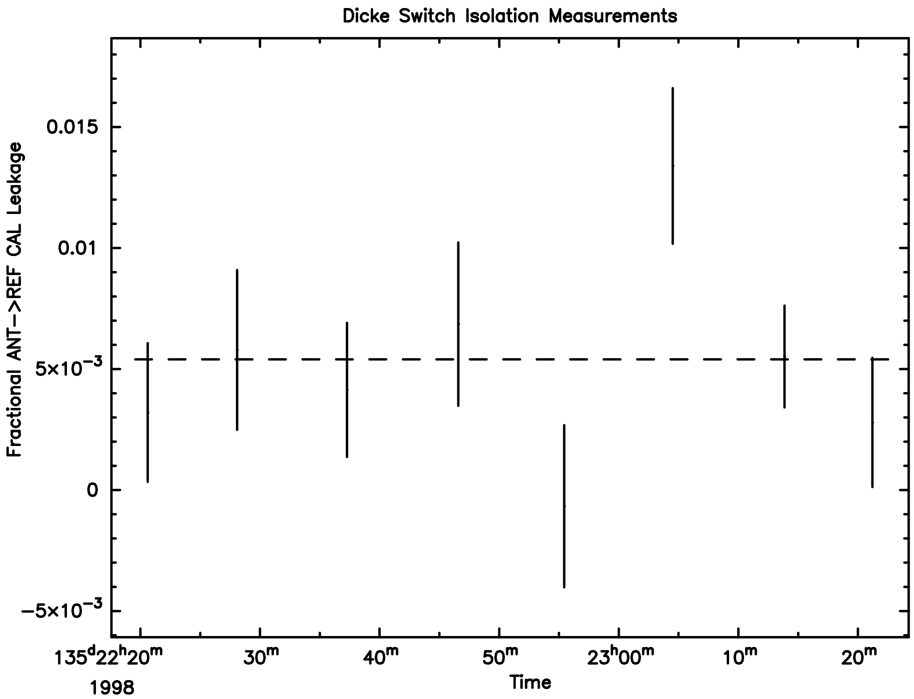

Figure 5.5: Dicke Switch Isolation Measurements. Successive CAL ON/OFF measurements were referenced onto each other and differenced. Significant gain variations over the course of the measurements give rise to the observed fluctuations. The mean departure from perfect isolation is $\xi = (5.4 \pm 1.1) \times 10^{-3}$.

5.2.3 Power Calibration

Although the NIST calibration allows the accurate computation of flux densities given T_{Ant}, the task of determining T_{Ant} from observed quantities (milliVolts) is not trivial. This issue is more important in the context of an absolute measurement, since for experiments which use an external flux density reference the sensitivity (K/Jy) and the receiver gain (mV/K) are not determined independently: the overall gain (mV/Jy, or some equivalent quantity) is obtained directly. Consequently, great care was taken in designing a power (T_{Ant}) calibration scheme. This task is made somewhat easier by the fact that we measure the antenna temperature in units of the cal signal, whose derived magnitude is not highly sensitive to slight errors in our brightness temperature references (two microwave absorbers at known thermodynamic temperatures– see § 5.4, and below).

To measure the receiver temperature T_{RX} of our system and the effective brightness temperature T_{cal} of our cal signal, we use the standard hot-cold load scheme. Our hot load is an ambient temperature microwave absorber and our cold load is an absorber immersed in liquid nitrogen. The increment in total power is measured against each of these loads providing a measurement of T_{cal}, T_{RX} and the receiver nonlinearity. The loads themselves are our ultimate temperature references. In terms of the temperatures of the hot and cold loads, the receiver temperature T_{RX} is given by

$$T_{RX} = \frac{T_{hot} - y\,T_{cold}}{y - 1} \tag{5.9}$$

where y is the observed ratio of total power against the hot load to total power against the cold load. Once T_{RX} is known, the effective brightness temperature of the cal diode may be determined by observing the total power against either of the hot or cold loads with the cal diode on and off. For observations against the cold load, we find

$$T_{cal} = \frac{y_{cal} - 1}{y - 1}\,(T_{hot} - T_{cold}) \tag{5.10}$$

where y_{cal} is the ratio of the total power observed with the cal diode on to total power observed with the cal diode off. If T_{cal} is derived from observations against the hot load, we find

$$T_{cal} = \frac{y_{cal} - 1}{y - 1}\,y\,(T_{hot} - T_{cold}). \tag{5.11}$$

Since observations at lower power levels are less affected by increased system noise and nonlinearity (see below), we derive T_{cal} from observations against the cold load.

The microwave absorber employed for each load was a 3-inch thick sheet of ECCOSORB CV[1]. Tests at liquid nitrogen temperature indicate that the absorber had an optical depth $\tau > 7.4$. At ambient temperatures, the optical depth is expected to be higher (Hemmati et al. 1985) , but this measurement is more difficult due to the increased system noise. The cold load was assumed to have a thermodynamic temperature equal to the boiling point of liquid nitrogen (76.3 K at atmospheric pressures characteristic of the Owens Valley). The front-face temperature of the hot load was measured with a hand-held infrared thermometer; this thermometer was calibrated (using ECCOSORB-CV) against a platinum resistance thermometer with a specified accuracy at room temperature of $\pm 0.02\,\mathrm{K}$. While in principle this calibration may have been necessary to relate the thermodynamic temperature to the effective infrared brightness temperature over the IR thermometer's bandpass (i.e., to correct for the unknown and presumably finite IR emissivity of ECCOSORB-CV) we found that both thermometers measured the same temperatures to $\sim 0.1\mathrm{K}$. Assuming that $\tau \geq 7.4$ for our absorber, the thermodynamic and brightness temperatures for both loads are identical to better than 0.1%. Given our measured optical depth, temperature gradients across the hot load do not significantly affect our measurements provided we measure the temperature of the front face of the absorber.

The manufacturer's specifications indicate that reflections from the absorber at 32 GHz are suppressed by 50 dB. The cold load cooler is constructed of a cross-linked polyethylene foam, which possesses good thermal properties and has a very low optical depth at microwave frequencies ($\tau \sim 7 \times 10^{-3}$). Laboratory measurements of the cooler show that it evinces a brightness temperature ~ 0.7 K higher than a cone of absorber dipped in liquid nitrogen. This measured brightness temperature excess is also consistent with the expected brightness temperature of a 300 K emitter with an optical depth of $\tau = 7 \times 10^{-3}$. We correct the cold load brightness temperature for this emission. In spite of the simplicity of the cone-load arrangement, these loads were not used for daily T_{RX} and T_{cal} measurements due to their lack of long-term emission stability. One potential concern which arises in the usage of a liquid-nitrogen-filled cooler is the impedance mismatch at the box-nitrogen

[1]ECCOSORB is a registered trademark of Emerson and Cuming Microwave Products.

interface; if there is significant power being emitted out of the horns (presumably of order T_{RX}), then some fraction of this power would be reflected back into the system, artificially increasing the measured receiver temperature. To the end of calibrating the first OVRO SZE experiment, Herbig et al. (1994) constructed a cold load box of the same cross-linked polyethelyene foam with an impedance-matching network on one side. This network consisted of a hexagonal pattern of (liquid-nitrogen-filled) holes on the inside of the cooler wall which provides a refractive index intermediate to that between free space and liquid nitrogen. No significant difference in power was observed between the matched and unmatched sides of the cold load. This together with the good agreement between the measured and theoretically computed box emission, show that neither internal reflections nor other excess emission mechanisms contribute significantly to our cold load measurement. For a more detailed discussion on the effects of excess emission on our T_{ant} calibration, see § 5.4.

In the taking of T_{RX} measurements, a $\sim 5\%$ receiver nonlinearity is seen (a compression of the cal signal at the hot load total power levels relative to what is seen at cold load power levels). Most likely this is due to a slight compression of the second or third stage amplifiers. We correct our measurements for nonlinearity by assuming that our system response P_{obs} to an input power P_{true} is described by

$$P_{obs} = g \times (1 + bP_{obs}) \times P_{true}, \tag{5.12}$$

where g is the receiver gain and b characterizes the nonlinearity in the system. For small excursions from perfect linearity as observed this should be a good description. This is the same description employed by Leitch et al. (1999) with good results on the OVRO 5.5-m Ka-band system, as well as the 40-m Ku-band system.

We measure b on an observation-by-observation basis by equating the cal signal increments observed against the hot and cold loads and solving for b. It is not significant to quote a mean value for b since this depends on g at the time of the observation which is significantly time variable. Application of this correction to each data point reduced the mean T_{cal} by 2%, and T_{RX} by 8%.

To measure the effectiveness of a nonlinearity correction based on Eq. 5.12, it is convenient to compare the cal diode increments observed against hot and cold loads to the increment observed against the sky at zenith. For all the data taken in the 14 T_{cal} measurements, prior to the application of the non-linearity correction the ratios of the raw cal increment observed against the hot load to the raw cal increment observed at zenith, and the equivalent quantity for the cold load, are 0.95 ± 0.01 and 0.99 ± 0.01 respectively. After the application of a nonlinearity correction derived separately for each observation, this ratio (for both loads) is 1.00 ± 0.02. Since no information about the cal signal increment at zenith was employed in the derivation of b, this is an independent indication that our simple model is a good description of the system non-linearity over the whole range of powers relevant to our observations.

Using this arrangement we measured T_{RX} and T_{cal} on 14 separate occasions during the period 10 May 1998 through 15 May 1998; after correcting for receiver nonlinearity and the Dicke-switch isolation, as well as applying a slight correction[2] for deviations from the Rayleigh-Jeans law, we find $T_{RX} = 54.8 \pm 0.9$ K and $T_{cal} = 14.34 \pm 0.07$ K (measurement error only).

5.3 Observations

The radiometry procedures used in observations on the 1.5-m telescope are the same as those used on the other single-dish radio telescopes at OVRO. The two fundamental procedures are FLUX and CAL measurements. A FLUX measurement is a double switched measurement in which the source is alternately placed in the REF and ANT beams; two integrations of switched power are executed in each position. This cancels out constant and linear power backgrounds in the measurement, such as those caused by the atmosphere, receiver noise and ground pickup. A CAL procedure consists of two integrations of switched power with the cal diode signal being injected into one of the receiver arms, bracketed by two integrations of switched power with the cal signal off. For more detail on these procedures refer to Readhead et al. (1989), Myers et al. (1997), and Leitch (1998). It is additionally possible to record (singly) switched power; this procedure is known as an AVERAGE. By doing a set of AVERAGEs around the nominal pointing center of some source , it is possible to derive the pointing offsets; this is known as a POINT procedure. Generally four AVERAGEs were done spaced at $\pm 0^{\circ}.27$ in azimuth and elevation around the source.

[2]This correction amounted to a 0.4% adjustment of our measured hot load temperatures, and a 0.8% adjustment of our assumed cold load temperature.

In March 1998 two days of pointing data were taken on bright celestial sources (Cas A, the Crab and Venus). These observations consisted of a cycle of POINT, FLUX, and CAL procedures executed repeatedly against the source in long tracks. From these data a pointing model was derived which reduced the rms pointing offset from 15'.4 to 2'.2 (0'.85 on Cas A) in addition to removing overall systematic pointing offsets. This is the pointing model which was used in subsequent observations. Due to the weather conditions in May reliable pointing tests were not possible, but for a small stiff dish such as this that presents no problem, as all of the pointing errors are likely to be constant offsets.

On 22 April 1998, observations of Cas A consisting of alternate pointings on the ANT and REF beam positions were taken in order to confirm the NIST-measured beam throw. We found, relative to these fixed offsets, an azimuth separation of $0'.04 \pm 0'.12$, and a zenith angle separation of $0'.70 \pm 0'.26$. We take this to be consistent with the nominal $(\Delta \mathrm{AZ}, \Delta \mathrm{EL}) = (-1^\circ.0 \pm 0^\circ.01, 0^\circ.0 \pm 0^\circ.1)$ offsets. Given our 25'.8 FWHM main beam, the neglect of the 0'.7 ANT/REF zenith angle offset amounts to a potential 0.3% systematic error in our FLUX measurements.

During the period 10 May 1998 – 16 May 1998, observations of Cas A were conducted when the weather permitted. These observations consisted of FLUXes (10 second integrations in each segment, with 15 second idle times to allow the telescope to acquire the position) interleaved at 10 minute intervals with CAL's (10 second integrations, 5 second idles). The pointing model described above was employed. Full tracks on the source were used in order to average out variations in atmospheric opacity or residual ground spillover over the course of a track.

The data were calibrated by scaling the observed FLUXes by the ratio of observed CAL's to the measured cal diode temperature ($T_{cal} = 14.34 \pm 0.07$K). Since the CAL and FLUX measurements were taken at the same power level no nonlinearity correction is necessary. If the standard deviation of any individual CAL or FLUX procedure is more than four times the average standard deviation observed in the entire data set, that datum is rejected. Similar 5σ edits were performed on the CAL and FLUX means. These edits remove a negligible fraction of the data but eliminate grossly discrepant data points caused by atmospheric interference or rare instrumental glitches.

Since the atmosphere has a significant opacity to microwave radiation, it is necessary to apply a correction for atmospheric attenuation. The observed flux density of a source as a function of zenith angle is

$$S\,(ZA) = S_o\,e^{-\tau\,\sec\,(ZA)}; \tag{5.13}$$

at 32 GHz, the optical depth τ is typically less than 0.1 when observations are conducted. Opacity corrections were determined by a straight-line fit of the natural logarithm source flux densities to sec(ZA), and the data multiplied by $e^{+\tau\,\sec(ZA)}$. Data at $ZA > 70°$ were excluded from the analysis. The 10 May 1998-16 May 1998 data set as a whole has a mean optical depth $\tau = 0.071$. Figure 5.6 shows the raw FLUX data uncalibrated for atmospheric attenuation. The straight-line fit in this figure corresponds to $\tau = 0.071$.

The weighted mean of the calibrated data yields $S_{cas} = 194.0 \pm 0.4$ Jy (measurement error only). The fully calibrated data are plotted versus ZA in Figure 5.7. The solid line shows the mean for all of the FLUXes, and the dashed lines show our 1σ error bars (see § 5.4). For clarity, the data have been binned into 100 equal bins in ZA. These data show evidence for some contamination at the ~ 3 Jy level; this is likely due to ground spillover which was not entirely eliminated by our double-differencing. An effect of similar magnitude is seen in the data plotted against parallactic angle (Fig. 5.8). Exclusion of the data at $ZA > 50°$ (data of notably lower quality) leaves the mean unaffected to $< 0.02\%$. The overall gradient in the FLUXes as a function of parallactic angle is well-correlated with ambient temperature and we therefore suspect that it is due to imperfect temperature control of the cal diode; this was confirmed in calibration observations taken in October and December of 1998. Since the T_{cal} measurements themselves were taken at a wide range of ambient temperatures, this is not likely to bias our result. The fact that the FLUXes as a function of ZA are roughly consistent with a constant value ($\chi^2_\nu = 1.62$ for 89 degrees of freedom) is an indication that the parallactic angle variations average out over the course of a track. In any case both of these effects are well within our calculated 1σ systematic error limits, which we describe in the next section.

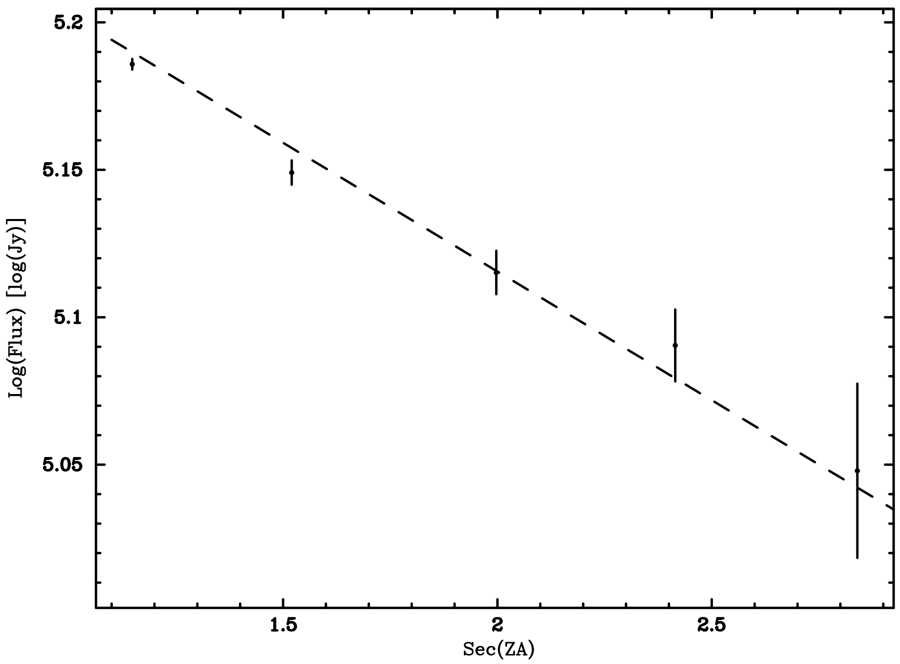

Figure 5.6: 10may98 - 16may98 FLUX observations of Cas A, uncalibrated for atmospheric attenuation. The best straight-line fit of the natural log of the source flux density to sec(ZA) is shown as a dashed line; this line corresponds to $\tau = 0.071$. The increased error bars at high airmass are due to both the increased atmospheric noise at high airmass and to a $\sim 1.6\%$ gradient in the FLUX as a function of parallactic angle.

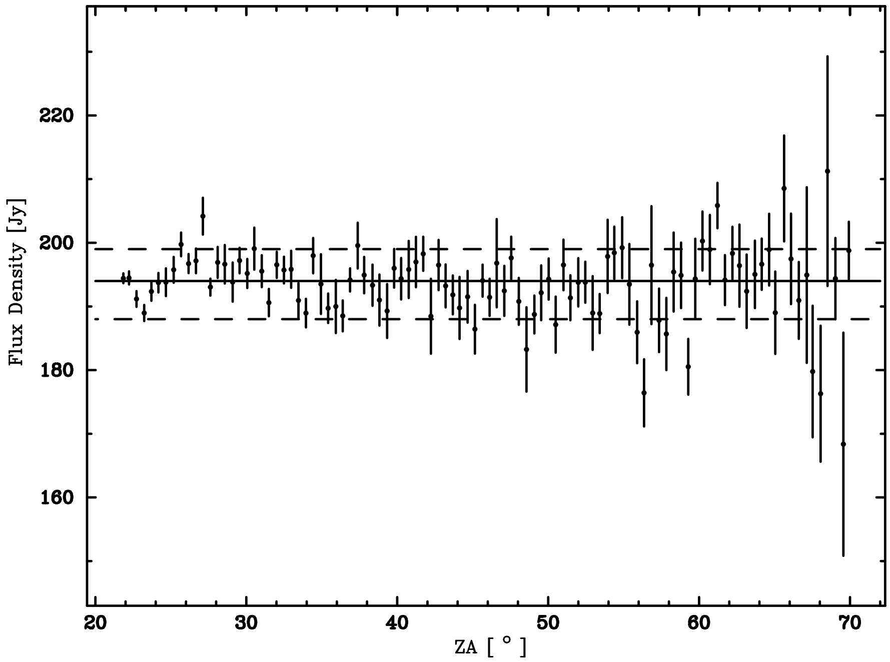

Figure 5.7: 10may98 - 16may98 FLUX observations of Cas A versus zenith angle, calibrated for atmospheric attenuation. The feature at $ZA \sim 28$ is most likely residual ground spillover (~ 1.5mK). The solid line is the average of all FLUXes; the dashed lines indicate the range of values included at the 68% confidence level using our estimated systematic errors ($S_{cas} = 194^{+5}_{-6}$ Jy).

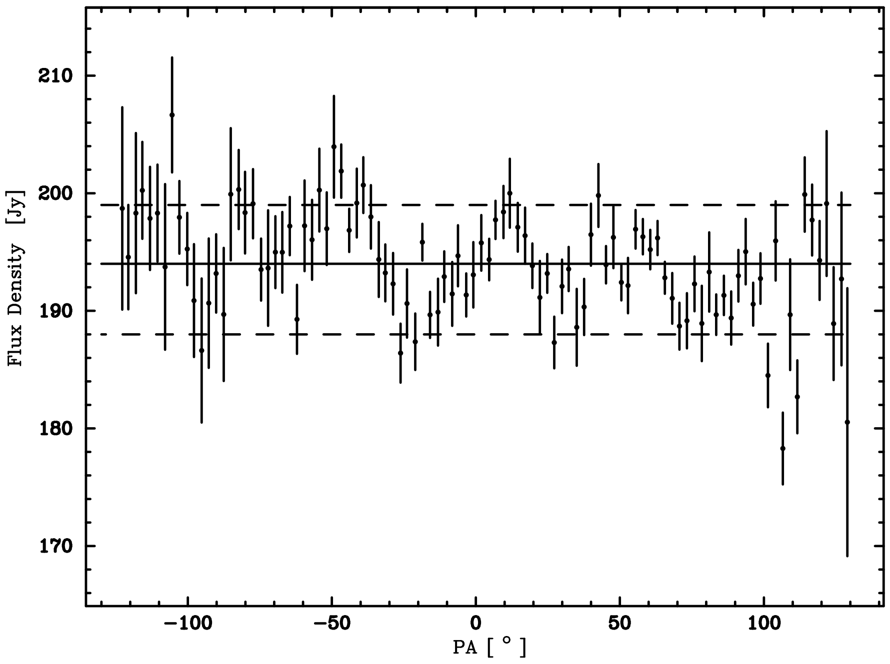

Figure 5.8: 10may98 - 16may98 FLUX observations of Cas A versus parallactic angle, calibrated for atmospheric attenuation. The slight overall gradient is due to an ambient temperature effect discussed in the text.

5.4 Systematic Error Budget

In this section we present our estimate of the contributions of various systematic effects to our measurement. We consider these effects in order of their importance.

The dominant source of uncertainty for our measurement is the NIST gain measurement error (1.4%). Short of recalibrating the telescope, there is little that can be done to reduce this. The fact that the NIST-measured beam characteristics were within $\sim 2\%$ of the predictions of the optical model is a good indication that NIST's error bars are reasonable. The physical configuration of the telescope was not altered during the NIST calibrations (Francis 1998). Due to the different reference planes for the NIST gain measurement and our HOT/COLD load calibration, there is an additional uncertainty which we estimate to be about 2.3% due to ohmic losses in the feeds. This would have the effect of making the NIST gain artificially low, hence affects our flux density only in the negative direction.

Based on the rms of the flux densities derived from individual days' observations we estimate that τ contributes no more than a 1.0% potential error to our measurement.

Since the observed ground spillover and T_{cal} effects noted in § 5.3 will average out to some extent over a track (and as T_{cal} measurements are taken at different ambient temperatures), we take these to contribute independent systematic errors at the level of half the observed maximum departure from the mean. Since the observed fluctuations are ~ 3 Jy in each case, this results in two contributions of 0.8% to our systematic error budget.

Since Cas A is located very close to the Galactic plane ($l = 111^\circ.74, b = -2^\circ.128$), there is the possibility that our measurements are contaminated by foreground sources, such as bright HII regions associated with young stellar systems, as well as by flat spectrum background radio galaxies present at all galactic latitudes. Unfortunately Cas A is the second brightest extrasolar source in the sky at our observing frequency, with the consequence that radio surveys of this region of the sky tend to be heavily contaminated due to the telescope sidelobes; on the other hand, the high overall flux density of Cas A reduces the fractional significance of interloping sources. The primary concern for observations with our dual-feed system is that a contaminating point source may pass through the scan pattern of one of the reference beams. Since the reference beams move on the sky relative to the nominal pointing center (Cas A), such an event introduces a characteristic hour angle dependence into our data. Based on the data we have collected, we place an upper limit of 16 Jy on the magnitude of possible point source contamination in the reference beams. We should indicate that while some of the individual features in Figure 5.8 are consistent with the signature of a single point source, all of them *jointly* are not. In particular, the feature centered at $PA = -20°$ is consistent with a contaminating point source of about 16 Jy, but the double feature (including the feature centered at $PA = 33°$) is *not* well represented by two point sources. We conclude therefore that most of the signal observed is residual ground spillover. Using a model which realistically accounts for the motion of the reference beams during a scan, a 16 Jy source placed at the *center* of one of our reference beams would bias the average flux density we infer for Cas A by 1.08 Jy (0.6%). We adopt this as a 1σ upper limit on possible point source confusion. Since there are only a handful of sources in the whole sky at 32 GHz with flux densities greater than a few Jy, this is likely to overestimate the level of point source contamination.

The accuracy of our pointing algorithm was determined using a Monte-Carlo simulation with realistic signal-to-noise statistics. The pointing error is dominated by the model residuals, which could be improved by more pointing in good weather. The overall pointing error is estimated to contribute a 0.7% systematic error to our result, of which 0.5% comes from the pointing model residuals.

While determining the cal diode brightness temperature, T_{cal}, is one of the most crucial aspects of our experiment, we have been able to do so very precisely, so this error is one of the least significant contributors to our error budget. This is largely due to the fact that T_{cal} is relatively insensitive to errors in the load temperatures. Using Equation 5.10, which takes into account the implicit load-temperature dependence of our system temperature determination, we find that the error in T_{cal} induced by an error in the expected cold load temperature T_{cold} is

$$\epsilon(T_{cal}) = -\frac{y_{cal} - 1}{y - 1} \times \epsilon(T_{cold}) \tag{5.14}$$

and the corresponding error due to the hot load (see Eq 5.11) is

$$\epsilon(T_{cal}) = \frac{y_{cal} - 1}{y - 1}\, y \times \epsilon(T_{hot}) \tag{5.15}$$

With the observed values of $y \sim 2.71$ and $y_{cal} \sim 1.11$, this yields about 0.6% of error in T_{cal} per degree K of error in either of the hot or cold loads.

Adopting $\epsilon(T_{hot}) = 0.5\,\mathrm{K}$ and $\epsilon(T_{cold}) = 0.7\,\mathrm{K}$ and adding these errors in quadrature, we obtain a 0.5% error in T_{cal}.

Even though there is a fairly significant nonlinearity in our receiver system, it affects our T_{ant} calibration at only the 2% level and so even relatively larger errors in the characterization of the nonlinearity affect us at the $\lesssim 0.4\%$ level. Systematic errors in T_{hot} or T_{cold} do not significantly affect this characterization since the nonlinearity measurements depend only on the observed cal signal *increment* against each of these loads.

In general the gain and source spectrum may vary across the band, and this may be a significant source of error for observations with a wide bandpass. For a source with a flux density $S(\nu)$ observed on a system with a frequency-dependent effective area $A_{eff}(\nu)$, the band-averaged spectral power is

$$\overline{P_{obs}} = \frac{1}{\Delta\nu}\int_{\nu_o-\Delta\nu/2}^{\nu_o+\Delta\nu/2} d\nu\, S(\nu)\, A_{eff}(\nu), \tag{5.16}$$

where ν_o is the band center and $\Delta\nu$ the total bandpass. If both $A_{eff}(\nu)$ and $S(\nu)$ can be reasonably approximated as power laws over this interval, then the band-averaged spectral power can be shown to be

$$\overline{P_{obs}} = A(\nu_o) \times S(\nu_o) + O\left(\frac{\Delta\nu}{\nu_o}\right)^2. \tag{5.17}$$

Variations in these quantities thus induce errors proportional to the fractional bandpass $\Delta\nu/\nu_o$ squared in the flux densities and brightness temperatures one infers under the assumption that one is measuring $S_\nu(\nu_o)$ instead of the band averaged flux density. For our narrow (2%) bandpass, this introduces errors at less than the 0.1% level and may be safely neglected.

Another potential concern for the accuracy of measurements made with dual-feed systems is that the sidelobes of one beam will be present at a significant level in the other beam, reducing the average gain of a doubly-switched measurement. Since the secondary is illuminated asymmetrically, the sidelobes of one beam in the direction of the other tend to be highly suppressed. The NIST measurements indicate that the sidelobes of one beam are suppressed by $\gtrsim 35$ dB near the maximum of the other beam (National Institute of Standards and Technology 1990); in contrast, the nearest sidelobes on the other side are at -20 dB. This is therefore not a concern for our system.

Our systematic error budget is summarized in Table 5.2. Adopting our measured value of $S_{cas} = 194.0 \pm 0.4$ Jy and the above calculation of our systematic error $\binom{+2.4\%}{-3.2\%}$ we have $S_{cas,1998} = 194^{+5}_{-6}$ Jy at 32.0 GHz.

Source	Sense	Fractional Magnitude
Nonlinearity	$\pm$	0.2%
T_{cal} (systematic)	$\pm$	0.5%
T_{cal} (meas.)	$\pm$	0.5%
Point Source Confusion	$+$	0.6%
Pointing	$+$	0.7%
Unsubtracted Ground Spillover	$\pm$	0.8%
T_{cal} Variations	$\pm$	0.8%
Atmospheric Opacity	$\pm$	1.0%
Antenna Calibration	$\pm$	1.4%
Ohmic Losses in Feeds	$-$	2.3%
Total		$+2.4\%$ -3.2%

Table 5.2: Total systematic error budget for 1.5-m absolute flux density measurement of Cas A.

Epoch	Dates	HEMT ID
1	21dec94 – 23dec94	NRAO A-12
2	03feb95 – 07feb95	NRAO A-12
3	20apr95 – 05may95	NRAO A-12
4	29nov97 – 09dec97	NRAO A-23
5	22oct98 – 28oct98	MAO-5

Table 5.3: Epoch definitions for 5.5-meter source observations reported in this section, along with the HEMT in place in the receiver during the observations. See Table 5.4 for the receiver band characteristics for each HEMT.

5.5 5.5-meter Observations and Leveraged - Flux Density Scale

While Cas A is a useful calibrator for experiments with very large beams ($\theta_{FWHM} \gtrsim \theta_{casA} \sim 5'$), it is not so useful for instruments with smaller beams, or for experiments at southern latitudes. It is therefore desirable to apply our absolute flux density measurement to a set of calibrators of smaller angular extent at a wide range of declinations. To this end, we have analyzed five epochs of observations of a set of calibrators (the choice of which is discussed below) relative to contemporaneous observations of Cas A. These observations were taken with the OVRO 5.5-meter telescope outfitted with a 32 GHz Dicke-switching receiver system with a ~ 6 GHz bandpass at 32 GHz. The primary beam of this instrument has two beams with a FWHM of 7'.35 and a separation of 22'.17. Using these observations plus our absolute value for S_{cas} we can establish an absolute flux density scale at our observing frequency for the set of sources we observed.

The epochs of observation were chosen from archival OVRO data with the criteria that the source observations consist of observations of any of our sources close to observations of Cas A, that the observations occur over a reasonably wide range of hour angles and that the observing conditions be sufficient to obtain a reasonable signal-to-noise on the source(s) over the observation as a whole. The data we selected fall into five epochs from December 1994 to October 1998; these epochs, together with the serial number of the HEMT present in the receiver at the time of the observations (see discussion below) are shown in Table 5.3.

Our choice of sources was dictated by the requirement that the calibrators be bright, relatively small in angular extent, and (for the most part)

HEMT ID	ν_1 (GHz)	$\Delta\nu$ (GHz)
NRAO A-12	31.9	6.05
NRAO A-23	31.5	6.62
MAO-5	31.9 ± 0.3	6.6 ± 0.6

Table 5.4: Bandpass characteristics of the 5.5-meter receiver with the three HEMTs used in observations.

non-variable. The sources we chose are NGC7027, 3C48, 3C84, 3C84, 3C147, 3C218, 3C273, 3C286, 3C345, 3C353, Jupiter, Saturn and Mars. The sources 3C48, 3C147 and 3C286 are quasars with steep spectra, and are regularly observed at the VLA as primary flux calibrators. The latter sources, and in particular Jupiter and Mars, are frequently used calibrators at centimeter wavelengths. The possible variability of some of these sources will be discussed below.

Since Cas A is comparable in size to the 5.5-meter primary beam, it is necessary to correct the observed flux densities for the effect of the convolution of the sky brightness with the telescope beam pattern. The details of this procedure are discussed by Leitch (1998) and Leitch et al. (1999). In brief, a high-resolution map of Cas A made at 32 GHz on the Effelsberg telescope Morsi (1997) was used as a brightness template in a Monte Carlo simulation, incorporating uncertainties in the 5.5-meter beam pattern and pointing model, to determine the ratio f of the total flux density of Cas A to the flux density observed with the 5.5-meter on Cas A . The 68% confidence interval of the resulting distribution is $f = 1.18^{+0.02}_{-0.01}$. This is the factor by which the 5.5-meter observed S_{cas} values must be multiplied to obtain the total flux density of Cas A, as would be observed by a telescope with a primary beam much larger than the extent of Cas A itself. This allows us to relate the 5.5-meter observations of alternate calibrator sources *relative* to Cas A to our *absolute* measurement of Cas A with the 1.5-meter telescope.

Given the wide bandpass of the 5.5-meter receiver system the variation of the source spectra across the observed band and the bandpass of the observing band itself must be accounted for. Leitch (1998) has extensively characterized the band properties of the 5.5-meter receiver from 1994 – 1997. Over this time period, two different HEMT's were employed in the receiver, and the receiver in each of these states has been fully characterized separately. In May of 1998, A-23 suffered a catastrophic failure and was replaced with the MAP non-flight HEMT MAO5. A full characterization of the receiver with

MAO5 in place has not been undertaken, but the data we have in hand are in reasonable agreement with the bandpass of A23. From these, we estimate $\delta\nu = (6.6 \pm 0.6)$ GHz , $\nu_{cent} = (31.9 \pm 0.3)$ GHz for the receiver with MAO5. Our adopted band characterizations are summarized in Table 5.4.

The strategy we choose is to interpolate the broadband 5.5-meter measurements of our calibrator sources (relative to Cas A) onto a 32.0 GHz value using our narrow-band measurement of S_{cas} at this frequency and spectral information culled from the literature, or, for the case of Cas A, obtained from measurements at OVRO. For 3C48, 3C147 and 3C286 we compute effective spectral indices over the 5.5-meter bandpass from the spectral fitting formulae given by Kellermann et al. (1969), with a standard power law of the form

$$S(\nu) = S(\nu_o) \times \left(\frac{\nu}{\nu_o}\right)^{\alpha}. \tag{5.18}$$

Our effective spectral indices for these sources are shown in Table 5.5. Although the formal errors in these spectral indices given the uncertainties quoted in Kellermann's fitting formulae are of order 0.01, we adopt error bars of 0.1 in order to allow for the extrapolation to 32 GHz and the possibility of secular evolution of the spectra at high frequency. For NGC 7027, a planetary nebula, we assume $\alpha = -0.1 \pm 0.1$; and for the other 3C sources , we assume that $\alpha = -0.8 \pm 0.1$. Kellermann finds from low frequency ($\nu < 15$ GHz) observations of Cas A that the spectrum is well described by a single power law with $\alpha_{cas} = -0.765 \pm 0.005$. Rather than extrapolate this low frequency result to 32 GHz, we use the 14.5 and 31.7 GHz RING5M measurements of Cas A (Leitch et al. 1999) to compute a spectral index which is more representative of the actual spectrum at our frequency. The RING5M measurements result in $S_{cas,14.5} = 313.6 \pm 8.9$Jy and $S_{cas,31.7} = 164.2 \pm 5.4$Jy, implying $\alpha_{cas} = -0.827 \pm 0.056$. This result is slightly steeper than the result of Kellermann at lower frequencies, but still consistent with a single power law over the entire range up to 31.7 GHz. These measurements are also in good agreement with the results of recent observations of Cas A with the BIMA array (Wright et al. 1999). In this analysis, Wright et al. have combined BIMA data at 28 and 83 GHz with 1 and 5 GHz VLA maps of Cas A to examine spectral index variations of the various "knots" of emission seen in Cas A at high resolution maps. The spectra of these structures are generally well described by power laws with $-0.81 \lesssim \alpha \lesssim -0.77$, up to and including the 83 GHz data. Since a single dish radio telescope is likely to measure slightly different spectral indices due to the dependence of the spec-

Source	Spectral Index
Cas A	-0.827 ± 0.056
NGC 7027	-0.1 ± 0.1
3C48	-1.18 ± 0.1
3C147	-1.21 ± 0.1
3C286	-0.82 ± 0.1
Jupiter	$+2.24 \pm 0.1$
Saturn	$+2.0 \pm 0.1$
Mars	$+2.0 \pm 0.1$

Table 5.5: Spectral indices used for the interpolation from wide-band flux measurements to 32.0 GHz flux densities. For all other sources, we assumed $\alpha = -0.8 \pm 0.1$. See the text for details on how the indices and uncertainties were estimated.

tral indices on spatial scale, we take this as merely suggestive, and adopt the value of α_{cas} computed above to interpolate our 5.5-meter measurements onto 32.0 GHz flux densities for all of our sources. We approximate the spectrum of Jupiter across our band using the model of Trafton (1965) as presented in the context of the Wrixon et al. (1971) measurements. Using this model, and assuming a constant power-law slope across our band, we compute an effective spectral index of $\alpha = 2.24$ from 28.5 to 40.0 GHz, which we use in relating our band-averaged flux densities to 32.0 GHz flux densities; we estimate a 1σ error of 0.1 in this quantity. For the other planets we assume a thermal ($\alpha = 2$) spectrum, with the same uncertainty. This strategy should do a good job of accounting for the effects of the overall shape of the spectrum on the average brightness temperature from 29 to 35 GHz, but may not get the actual 32.0 GHz brightness temperature for sources with very narrow features in the spectrum (like Mars).

It is well known that the flux density of Cas A is slowly decreasing as a function of time. Baars et al. (1977) gives an expression for the fractional annual decrease in Cas A's flux density:

$$\frac{\delta S}{S} = [(0.0097 \pm 0.0004) - (0.0030 \pm 0.0004) \log \nu_{\mathrm{GHz}}]\,\mathrm{yr}^{-1}; \tag{5.19}$$

where Δt is the time interval in years. $S_{cas,t}$ is then

$$S_{cas,t} = S_{cas,t_o} \times (1 - \frac{\delta S}{S})^{\Delta t}. \tag{5.20}$$

At $\nu = 32\,\mathrm{GHz}$, this yields a $(0.52 \pm 0.07)\%$ decrease in S_{cas} per year. This functional form for the secular variation has found some support at 15 GHz in the work of O'Sullivan and Green (1999). We take $\frac{\delta S}{S} = 0.52 \pm 0.15\,\mathrm{yr}^{-1}$. Using this expression we can compare observations taken at differing epochs to our absolute measurement of Cas A (epoch May 1998). For the epochs we are examining, this is at most a 2% correction. A misestimation of the variability of Cas A will increase the variance of the flux ratios we observe for a given source, and hence be automatically accounted for in the final error budget of each source.

For these observations, scans on these calibrators were interleaved with observations of Cas A over a wide range of hour angles, allowing an accurate determination of the atmospheric opacity and frequent relative calibration using Cas A. Table 5.6 shows the average observed flux ratios of our sources for all epochs. Where the epoch-to-epoch scatter in the observed ratios exceeds the mean error bar for a given source, the epoch-to-epoch scatter is adopted as the error in the ratio. This strategy automatically incorporates into our final error bar any systematic errors which may not be manifest in the errors estimated for a given epoch's observations, such as source variability and any errors in the characterization of Cas A's secular behavior. For each source "X" with spectral index α_x , measured relative to a calibrator "C" (with associated flux density $S_{c,32}$ and spectral index α_c) with a rectangular bandpass $\delta\nu$ centered at a frequency ν_1, the narrow-band flux ratio referenced to an epoch t_o, $R_{32.0,t_o}$, can be shown to be

$$R_{x,32.0,t_o} = R_{x,obs,t} \times (1 - \frac{\delta S}{S})^{(-\Delta t)} \times \frac{\alpha_x + 1}{\alpha_c + 1} \times \frac{\nu\left(\frac{\nu}{32}\right)^{\alpha_c}\Big|_{\nu_1-\delta\nu/2}^{\nu_1+\delta\nu/2}}{\nu\left(\frac{\nu}{32}\right)^{\alpha_x}\Big|_{\nu_1-\delta\nu/2}^{\nu_1+\delta\nu/2}}, \tag{5.21}$$

where the values of Δt , ν_1 and $\delta\nu$ used are those appropriate to the epoch of observation. These are the ratios we quote in Table 5.6. While the data have been corrected for atmospheric attenuation using a mean optical depth $\tau = 0.049$, these corrections are relatively unimportant for our measurements since any errors in τ will tend to cancel in the ratio. The flux ratios quoted have also been corrected for the form factor indicated above, and the error bars include a 1.7% systematic error due to the determination of this form factor. Planetary flux densities have been expressed in K/Jy using the relation

$$\frac{T}{S_{cas}} = \frac{\lambda^2 R}{2k\,\delta\Omega}, \tag{5.22}$$

where T is the brightness temperature of the planet, $\delta\Omega$ is the solid an-

Source	Epochs	Mean Flux Ratio	$S_\nu(32)$ or $T(32)$
NGC7027	1-3	$(2.76 \pm 0.02) \times 10^{-2}$	5.45 ± 0.20 Jy
3C48	2,5	$(4.37 \pm 0.40) \times 10^{-3}$	0.861 ± 0.085 Jy
3C84	4,5	$(6.22 \pm 0.03) \times 10^{-2}$	12.33 ± 0.45 Jy
3C147	1-5	$(7.29 \pm 0.28) \times 10^{-3}$	1.436 ± 0.076 Jy
3C218	2,3	$(9.55 \pm 0.28) \times 10^{-3}$	1.880 ± 0.062 Jy
3C273	4,5	$(2.14 \pm 0.02) \times 10^{-2}$	42.4 ± 1.6 Jy
3C286	2-5	$(9.83 \pm 0.42) \times 10^{-3}$	1.95 ± 0.11 Jy
3C345	5	$(5.10 \pm 0.11) \times 10^{-2}$	10.11 ± 0.43 Jy
3C353	2,3	$(1.92 \pm 0.02) \times 10^{-2}$	3.80 ± 0.43 Jy
Jupiter	2-5	0.800 ± 0.030	$155.1^{+6.8}_{-5.7}$ K
Mars	2,3	0.990 ± 0.028	$196.0^{+7.5}_{-7.6}$ K
Saturn	4,5	0.726 ± 0.019	$140.8^{+4.4}_{-4.9}$ K

Table 5.6: Observed ratios of calibrator sources relative to Cas A. Planets' relative flux densities are expressed in units of K/Jy. All flux densities have been corrected to epoch May 1998 on an epoch-by-epoch basis, and interpolated onto narrow-band flux ratios using Equation 5.21.

gle of the planet at the time of the observation (determined from standard ephemerides), R is the observed ratio of the planetary flux to the flux of Cas A, and k is Boltzmann's constant. For this calculation, we used the value of λ appropriate to each epoch of observation.

With these flux ratios in hand, it is then straightforward to obtain the flux density at 32.0 GHz $S_{x,32}$ of the source "X" :

$$S_{x,32} = R_{x,32,t_o} \times S_{c,32,t_o}. \tag{5.23}$$

For the case at hand, $S_{c,32,t_o} = 194^{+5}_{-6}$ Jy. These results are also shown in Table 5.6.

Since in general a Gaussian distribution of spectral indices does not give rise to a Gaussian distribution of flux densities, Equations 5.21 and 5.23 were jointly evaluated 10^6 times for each source "X" with independently varying R, α_c , α_x , $S_{c,32}$, ν_1 and $\delta\nu$ values drawn from the (assumed Gaussian) populations implied by the error estimates we have quoted above. For R, we have used *each epoch's* observed flux ratio together with the error bar inferred from the scatter internal to those data. For sources not bright enough to point on, we also included the effects of the residuals in the 5.5-meter pointing model ($0'.45$ rms — an average over all epochs). The error bars quoted in Table 5.6 are the 68% confidence intervals inferred from this simulation. For the 3C sources and NGC7027, the error intervals inferred are virtually unchanged relative to those which are obtained by ignoring finite bandpass effects. This is due to the fact that these sources have spectral indices very similar to that of Cas A.

Figure 5.9 shows the *relative* flux ratio for the five most-observed sources in our sample as a function of epoch. While there is some indication that epochs 4 and 5 may be slightly lower than other epochs, it is difficult to disentangle this effect from the intrinsically large scatter of the data. In particular Jupiter, the brightest of these five sources, shows no departure from the mean greater than 2% in four epochs of observation; NGC7027, the second brightest, shows less than this. The data points for these two brightest sources are shown connected by bold lines in the figure; they are consistent with a constant value of 1.0. For Jupiter, the uncertainties in the source spectra and band characterization have been included in each epoch's error bar; these uncertainties dominate the uncertainty in the epoch 5 flux ratio.

Some of these sources are at least slightly variable, and the variability of some of them is not known. Based on our observations and existing data, we designate the planets, plus NGC7027, 3C48, 3C147, and 3C286 as useful calibrators at 32.0 GHz. There are indications that 3C147 may be slightly variable. For convenience, we summarize our findings for these sources in Table 5.7. Our brightness temperature for Mars has been corrected from a mean heliocentric radius of 1.658 AU for the epochs of observation to a fiducial heliocentric radius of 1.524 AU using an $r^{0.25}$ law (Epstein 1971) to facilitate comparison with other measurements. In this table we have adopted the more precise Leitch (1998) values for S_{3C286}/S_{cas} and T_{Jup}/S_{cas}.

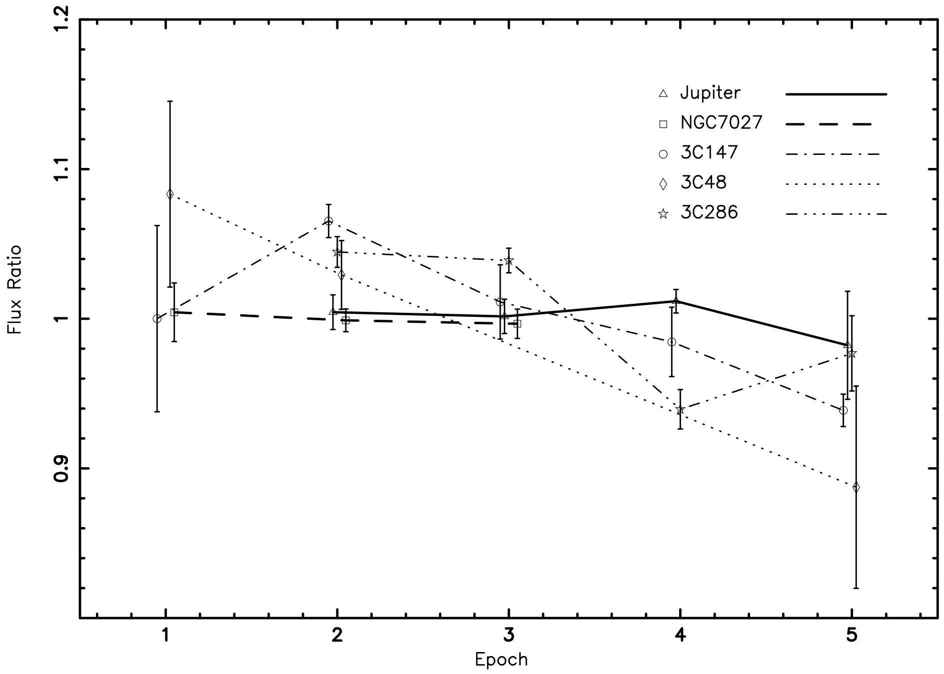

Figure 5.9: Flux ratios for the best potential calibrator sources in our sample, relative to Cas A. The flux ratio for epoch of each source has been divided by the mean flux ratio for that source; Jupiter has been corrected for the bandpass characteristics quoted in Table 5.4. All sources been corrected for the secular evolution of Cas A.

Source	S_ν (Jy) or T (K)
Cas A	$(194^{+5}_{-6}\,\mathrm{Jy})^A$
NGC7027	$5.45 \pm 0.20\,\mathrm{Jy}$
3C48	$0.861 \pm 0.085\,\mathrm{Jy}$
3C147	$1.436 \pm 0.076\,\mathrm{Jy}$
3C286	$2.02 \pm 0.07\,\mathrm{Jy}$
Jupiter	152^{+4}_{-5} K
Saturn	141^{+4}_{-5} K
Mars	200 ± 8 K^B

^{A} 32.0 GHz flux density standard

^{B} T_{mars} corrected to 1.524 AU heliocentric radius.

Table 5.7: Final absolute calibration results.

5.6 Discussion and Conclusion

We have presented an accurate measurement of the 32 GHz flux density of Cas A, $S_{cas,1998} = 194^{+5}_{-6}$ Jy . This is the first direct measurement of S_{cas} above 16 GHz. This measurement provides a firm foundation for calibrating experiments in the vicinity of 32 GHz. The resulting flux scale has an uncertainty of $\sim 3\%$, a significant improvement over other flux density scales at this frequency, most of which contain uncertainties $> 6\%$.

By way of comparison, the RING5M program conducted at OVRO recently derived S_{cas} relative to observations of DR21 on the OVRO 5.5-m telescope at 32 GHz (Leitch et al., 1999). Using Dent's (1972) flux density for DR21, and applying the form factor for the OVRO 5.5-m beam derived from a 32 GHz map of Cas A made with the Effelsburg telescope (see § 5.5), they find $S_{cas,1996} = 195.8^{+6.4}_{-5.7}$ Jy, corresponding to $S_{cas,1998} = 193.8^{+6.4}_{-5.7}$ Jy. This is in agreement with the result reported in this paper.

Until the RING5M calibration work, the OVRO Ka-band flux density scale was based on the Wrixon et al. (1971) absolute measurement of Jupiter, $T_J = 144 \pm 8$ K. This implies $S_{cas,1996} = 185.5 \pm 10.3$ Jy, consistent with both this absolute measurement and the analysis relative to DR21 (although the latter is not completely independent of it), but with an associated error of 5.5%, or nearly twice that in our measurement of Cas A. The Kellermann scale implies $S_{cas,1994} = 186.5 \pm 3.7$, including only formal errors in the Kellermann scale, but with a much larger error associated with the extrapolation to 32 GHz and the secular correction. The Saskatoon experiment (Netterfield et al. 1997) estimated an uncertainty of 13% in this value.

We have also presented absolute flux densities for a standard set of centimeter-wavelength calibrator sources, including Jupiter and Mars. These measurements should facilitate the calibration of experiments at a wide range of angular scales and terrestrial latitudes. These measurements have 1σ accuracies ranging from 3.1% (for 3C147) to 10% (for 3C48). Our measurement for 3C286 is in good agreement with that of Leitch (1998), who finds $S_{3C286}(32\,\mathrm{GHz}) = 2.02 \pm 0.07$. Our inferred brightness temperature for Jupiter ($T_J = 152^{+4}_{-5}$ K) is in excellent agreement with both Wrixon's $T_J = 144 \pm 8$ K, and the RING5M (Leitch 1998) value of 152 ± 5 K. We emphasize that the Leitch value of T_J is independent of our quoted value insofar as the calibrations of these experiments were independent. Our measurement of $T_{Mars} = 200 \pm 8\,\mathrm{K}$ is consistent with the results of Hobbs & Knapp (1971), who find $T_{Mars} = 207 \pm 13$ K at 9.55 mm, and with Ulich (1981) who finds $T_{Mars} = 194 \pm 8$ K at 9.5 mm. All of these results are referred to a standard solar distance of 1.524 AU. The compilations of microwave observations of Mars given by Epstein (1971) and Efanov et al. (1971) are also in good agreement with our measurement near $\lambda = 1$ cm; our results are significantly more precise than any of the 1 cm measurements reported in these compilations. Our measurements of these sources offer an excellent basis for the calibration of current and future experiments in the vicinity of 32 GHz.

Chapter 6

5.5-m SZE Observations

The ultimate aim of this thesis is to obtain a more accurate measurement of the Hubble Constant from the SZE. In this chapter we address this goal directly with the x-ray models presented in Chapter 4, the 32 GHz absolute calibration of Chapter 5, and observations of the SZE with the OVRO 5.5-meter telescope. First (§ 6.1) we describe the observing techniques employed in our observations, give a brief description of the instrument (§ 6.2), and elaborate on the concept of equivalent temperature introduced in Chapter 2 (§ 6.3). Next (§ 6.4) we present a review and recalibration of the results of Herbig et al. (1995) and Myers et al. (1997). In § 6.5 we present the results of recent observations at OVRO. Finally (§ 6.6), we discuss the interpretation of these observations, yielding measurements of the Hubble constant from the sample using the density models of Chapter 4 and the electron temperatures presented in Chapter 3, as well as direct measures of the baryon surface mass density. In this section we address the potential impact of departures from isothermality on our inferred value for H_0. Throughout, we use the terminology introduced in Chapter 2 for the description of single-dish switched observations of the thermal SZE.

6.1 Observing Strategy

As the brief review of Chapter 1 indicates, it is only the recent availability of low-noise, broad-bandwidth HEMT amplifiers which has made accurate observations of the SZE by ground-based observers feasible. Even with the improvements brought about by these devices, the challenges are substantial.

This is due to the fact that the signal we seek to measure ($\sim 300\,\mu$K) is comparable to or smaller than many contaminating signals which are present. In response to this, several observational techniques have been developed. Table 6.1 indicates the primary noise sources with which we must contend, along with the strategies adopted to compensate. For the most part, these strategies involve successive levels of differencing applied to the data in order to remove constant offsets, gradients, and higher terms which do not originate as true sky signals.

The OVRO 5.5-meter telescope as configured for SZ and CMB observations possesses two feed horns which give rise to two beams separated by $22'.2$ in azimuth on the sky. The first level of switching consists of alternate 1-ms integrations against the two corresponding patches of sky. Typically the source of interest is placed in one beam (the "ON" beam) while the other (or "REF") beam observes a nominally blank batch of sky $22'$ away in azimuth. Differencing these two integrations removes foregrounds that are constant both spatially and temporally (on the appropriate scales) while leaving the signal of astronomical interest. Thus while receiver noise is to some extent the dominant component of the system noise at any given point in time, it tends to be stable in time and is effectively removed by this process. This is somewhat less effective for atmospheric noise, a point which we discuss further below. This form of switching is called Dicke switching, after R. Dicke who invented it as a means of compensating for low frequency gain instabilities in early radio-astronomical receivers.

In order to diagnose the level at which atmospheric noise remains in our single-differenced power measurements, we will compare the noise statistics observed against the sky to those observed against temperature-stable internal waveguide terminations (see § 6.2). For a thermal-noise limited receiver with a system temperature T_{sys}, the standard deviation (SD) in a series of switched power measurements, each $\tau_S = \tau_{on} + \tau_{ref}$ in duration, can be shown to be

$$\sigma_S = \frac{2\,T_{sys}}{\sqrt{\Delta\nu\,\tau_S}}, \tag{6.1}$$

where $\Delta\nu$ is the system bandpass. A well-designed system should approach this limit in the absence of atmospheric noise. Figure 6.1 shows the distribution of the SD's in singly-differenced measurements of the atmosphere (light line) and of the internal cold loads (dark line), both relative the thermal expectation given by Eq. 6.1; the thermal expectation was computed directly from the observed total power (minus the contribution of a post-detector DC bias) with the correct value of τ_S for each individual measurement. The data shown in this figure are from October 1996 to March of 1997, and the only forms of data editing which have been performed are 4 σ outlier edits and the removal of periods where the radiometry was saturated. The long tail of the atmospheric SD distribution indicates a significant degree of high-frequency atmospheric noise (due, e.g., to cloudlets drifting through the divergent telescope beams) present after the Dicke switching. The dark line characterizes the instrument performance; the fact that the mean SD against the internal cold loads is $\sim 30\%$ higher than the thermal expectation may be indicative of a low-level oscillation in the HEMT. Successively more stringent filters (such as those we discuss in § 6.5.1) reduce the high-SD tail due to atmospheric noise, but only by filtering out 97% of the sky data do we achieve an SD distribution comparable to the instrumental distribution. This implies that for results significantly better than those achieved at OVRO on the 5.5-meter, a better site— rather than a better instrument— is paramount.

In addition to Dicke switching, the telescope is nodded in azimuth on 40 – 60 second timescales in such a manner that three patches of sky are observed in successive Dicke-switched integrations. This double-differencing procedure is known as a FLUX measurement, and is discussed in detail by Readhead et al. (1989), Myers et al. (1997), and Leitch (1998). While most of the ~ 3 K of atmospheric and ground-pickup gradients are cancelled by the double-differencing in the FLUX, $\sim 300\,\mu$K of differential ground pickup typically remains. Blank fields are observed to subtract this. These fields are selected to lie a fixed distance in Right Ascension ahead of and behind the target, and the fields are sequentially observed for a duration of time equal to the spacing in Right Ascension. In this way each field is observed over the same range of azimuth and zenith angle, and ground-based signals can be cancelled. The three fields we designate LEAD, MAIN, and TRAIL (or L/M/T); for more details on this technique see also Myers et al. (1997) and Herbig (1994).

The most significant astrophysical foregrounds at 32 GHz are discrete radio sources (Tegmark & Efstathiou 1996). We identify potentially contaminating sources from low-frequency surveys and perform observations of them at 18.5 GHz with the OVRO 40-meter which are (insofar as possible) contemporaneous with our 5.5-meter observations. More details on our procedures can be found in § 6.5.2 and Myers et al. (1997).

Finally, there are low-level gain fluctuations in the 5.5-meter receiver and electronics. To allow for this, there are four internal noise sources (or cal

Source	Level	Strategy
System Noise	~ 31 K	Dicke Switching
Atmosphere (D.C.)	~ 12 K	Dicke Switching
Ground Pickup (D.C.)	~ 6 K	Dicke Switching
Gradients	~ 3 K	FLUX
Residual Ground Signal	$\sim 300\,\mu$K	L/M/T
Discrete Source Contamination	$\lesssim 60\,\mu$K	40-m obs.
System Gain Fluctuations	$\sim 3\%$	cal diodes

Table 6.1: The potential sources of systematic error and noise in our SZE measurements, and the strategies for eliminating them.

diodes) whose outputs have shown remarkable stability over the years. The stability of the cal diodes allows us to correct for slight changes in the system gain on timescales shorter than we can feasibly calibrate off of external flux density references. By way of comparison, the raw CAL flux densities show a scatter of 2.8% over the entire 1996 – 1997 observing season; this is primarily an indication of the stability of the system gain, which is already quite good. The ratio of the observed flux density of an independent source and the CAL flux densities will cancel any such variations, leaving only real variations in the CAL diode brightness temperature and the atmospheric opacity. The standard deviation, over the same period of time, of the flux density of Cas A is 0.9%. Since this is comparable to the level of fluctuations in the atmospheric opacity observed historically at OVRO, we can only conclude that the cal diodes' effective brightness temperatures are stable to something better than 1%.

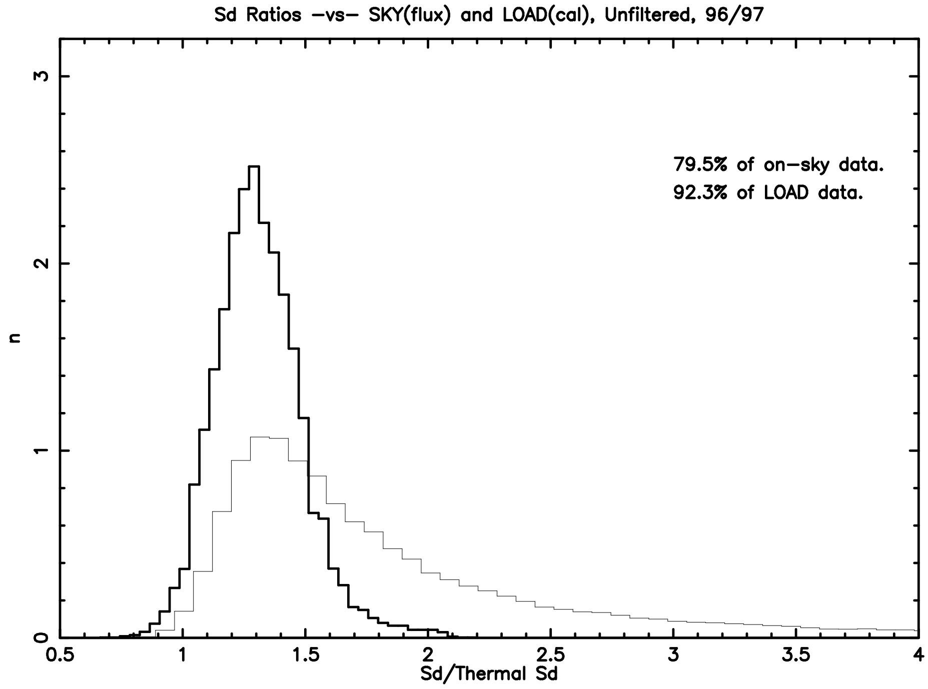

Figure 6.1: Standard deviation in switched power observed in measurements against the atmosphere (light line) and temperature-controlled internal waveguide loads (dark line). The normalization of these curves is such that the integral under each is unity.

6.2 The 5.5-meter Telescope

The observations were conducted with the OVRO 5.5-meter telescope outfitted with a 32 GHz receiver system. The characteristics of this telescope and receiver system have been exhaustively discussed by Leitch (1998) and Herbig (1994); the characterization of Leitch (1998) is the instrument calibration which underlies our analysis[1], and to which we refer the interested reader for details beyond the brief summary given here.

The telescope consists of a 5.5-meter parabolic dish on an altitude–azimuth mount with a dual-horn Dicke-switching receiver at the Cassegrain focus. At 32 GHz, this configuration results in a primary beam FWHM of $7'.35$ and a beam throw of $22'.16$ in azimuth. The Cassegrain mounting of the receiver is essential in reducing ground spillover to a reliably subtractible level. At the start of the 5.5-meter's scientific lifetime at OVRO, great pains were taken to reduce the level of ground spillover even further by replacing the 4-legged secondary support structure which was initially in place on the telescope with a 3-legged support structure. The final configuration also sports reflective baffles which redirect stray ground radiation to infinity and beyond. An excellent account of these improvements is given by Herbig (1994).

The heart of the receiver is a GaAs HEMT amplifier, which provides 26 dB of gain together with the low noise temperature and broad bandwidth essential to achieving the sensitivity necessary for accurate measurements of the SZE. A Dicke switch provides continuously alternating 1-msec "integrations" against either feed horn; both the Dicke switch and the HEMT are enclosed in a dewar which is maintained at ~ 15 K under normal observing conditions. System calibration is facilitated by four broadband noise sources or cal diodes; cross-guide couplers prior to the Dicke switch provide for the injection of these signals into either side of the signal chain. At one time, two circulating ferrite switches (identical to the Dicke switch except that their state is not continuously changed) before the cross-guide couplers permitted two internal, temperature-controlled waveguide terminations to be switched into the signal path instead of the feed-horns; this provides greater stability for the cal diode measurements, and is a useful degree of freedom for diagnostic testing (e.g., system noise measurements and studies of the noise

[1] Although as per the discussion of § 6.3 the only aspect of the instrument calibration which actually affects our scientific results is the beam characterization.

statistics of our measurements). In October of 1997 one of these circulators was removed for use as the Dicke switch in the new 40-meter Ka-band receiver, so after the receiver was brought back up on October 20, 1997 this capability was no longer available.

Regular system temperature measurements through the period of observation provided a monitor on the system performance beyond that given by the data itself. These measurements showed receiver temperatures of $\sim 31 \pm 2$ K. Although we also obtain measurements of T_{Cal} from these procedures which are consistent with the values derived from external calibrators, the T_{Cal} values we quote here are derived from contemporaneous observations of celestial calibrators.

6.3 Equivalent Temperature Calibration

Radio-astronomical signals are typically expressed in units of the *antenna temperature*, T_{Ant}, which is the signal which would be produced by a blackbody at temperature T_{Ant} that entirely fills the telescope beam-pattern. When observing point sources, this may be straightforwardly converted into flux units by dividing by the telescope *sensitivity*, Γ. When observing extended sources, the quantity of interest is typically the surface brightness, which is most appropriately expressed as a temperature. Most extended sources typically do not subtend the entire beam-pattern of the telescope, however, and consequently we define the *equivalent brightness temperature* as

$$T_{eq} = \frac{\Omega_{Ant}}{\Omega_{Beam}} T_{Ant}. \tag{6.2}$$

This is the thermodynamic temperature which a perfect blackbody exactly filling the main beam of the telescope would have to possess in order to reproduce the observed signal. This is a more appropriate unit than the antenna temperature for expressing signals due to extended objects such as SZ clusters.

We consider the case where all observed signals are measured in units of the power ,P_{Cal}, due to an internal noise calibration diode (or cal diode). While the antenna temperature of this diode must itself then be measured relative to some external flux reference, which introduces some additional error into our final result, the added stability offered by this procedure more than compensates. Let the antenna temperature of the cal diode be T_{Cal}, and the observed powers in instrumental units of the cal diode and a source "X" be P_{Cal} and P_X, respectively. Then the antenna temperature of the source is given by

$$T_{Ant,X} = \left(\frac{P_X}{P_{Cal}}\right) T_{Cal}. \tag{6.3}$$

T_{Cal} itself is determined from observations of a calibration source "src" with an assumed flux density S_{src}. The antenna temperature of the calibration source is

$$T_{Ant,src} = \left(\frac{P_{src}}{P_{Cal}}\right) T_{Cal} \tag{6.4}$$

$$= \frac{1}{2k_B} A_{eff}\, S_{src}. \tag{6.5}$$

Equating Eqs. 6.4 and 6.5 and using $\Omega_{Ant} A_{eff} = \lambda^2$, we find

$$T_{Cal} = \left(\frac{P_{Cal}}{P_{src}}\right) \frac{\lambda^2}{2k_B} \frac{1}{\Omega_{Ant}} S_{src}. \tag{6.6}$$

While Ω_{Ant} must be determined by an independent procedure, in practice we will see that this does not matter[2]. Substituting Eq. 6.6 into Eq. 6.3, we find the antenna temperature of the source "X" to be

$$T_{Ant,X} = \left(\frac{P_X}{P_{Cal}}\right) \left(\frac{P_{Cal}}{P_{src}}\right) \frac{\lambda^2}{2k_B} \frac{1}{\Omega_{Ant}} S_{src}. \tag{6.7}$$

Using Eq. 6.2, we obtain the equivalent brightness temperature for the source "X":

$$T_{eq,X} = \left(\frac{P_X}{P_{Cal}}\right) \left(\frac{P_{Cal}}{P_{src}}\right) \frac{\lambda^2}{2k_B} \frac{1}{\Omega_{Beam}} S_{src}. \tag{6.8}$$

From this it is apparent that the actual telescope calibration (i.e., the measurement of Ω_{Ant} or, equivalently, A_{eff}) is not important as long as the calibration is done consistently. Furthermore, Ω_{Beam} itself is only a fiducial quantity for our case. This may be seen by noting that the quantity of interest is the *ratio* of $T_{eq,X}$ to a predicted equivalent temperature $T_{pred,X}$ given by (see Chapter 2, § 2.3.2)

$$T_{pred,X} = \frac{1}{\Omega_{Beam}} \int d\Omega\, R_N(\hat{\Omega})\, T(\hat{\Omega}). \tag{6.9}$$

[2] Typically one measures T_{Cal} directly via a hot/cold load procedure, and uses Eq. 6.6 to solve for Ω_{Ant}.

Hence uncertainties in the beam area enter into our final results only as an uncertainty in the form of the normalized telescope response $R_N(\hat{\Omega})$.

Equations 6.8 and 6.9 illustrate all of the fundamental sources of uncertainty in our H_0 measurement. These are, in descending order of importance, uncertainties in the source model $T(\hat{\Omega})$, noise in the measurement of P_X/P_{src}, the uncertainty in the radio flux scale S_{src}, uncertainty in the determination of $R_N(\hat{\Omega})$ over the region where the integral receives support, and (typically negligible) noise in the measurement of P_{Cal}/P_{src}. For a nearby cluster such as Coma the uncertainty in the beam characterization is usually larger than that of the radio flux scale, and in many clusters the measurement error is more significant than the model uncertainties.

We base our calibration on the measurement, presented in Ch. 5, of the flux density of Cas A: $S_{cas} = 194^{+5}_{-6}$ Jy. Using the Leitch (1998) value for the ratio (in K/Jy) of the brightness temperature of Jupiter to the observed flux density of Cas A, and allowing for the form factor 1.18 ± 0.017 determined for Cas A in that work, we derive $T_J = 152 \pm 5$ K, which we will use to recalibrate the Myers et al. (1997) results; that work assumed $T_J = 144 \pm 8$ K. Our calibration of the new SZE data (§ 6.5) will be based directly on Cas A.

Table 6.2 presents the values we adopt for the 5.5-meter sensitivity , beam solid angle, main-beam solid angle, beam width, beam efficiency, and aperture efficiency; also shown are the main-beam solid angles assumed by Myers et al. (1997) and Herbig (1994), the brightness temperatures for Jupiter upon which these calibrations are based, and the conversion factor f by which the cited SZE results must be multiplied to reference them onto the calibration of the current work. We discuss the calibration of the Coma data in § 6.4.1.

	This work	Myers et al.	Herbig et al.
Γ (K/Jy)	$(4.10 \pm 0.15) \times 10^{-3}$	—	—
Ω_{Beam} (Sr)	$(7.92 \pm 0.28) \times 10^{-6}$	—	—
Ω_{Main} (Sr)	$(5.21 \pm 0.03) \times 10^{-6}$	$(5.12 \pm 0.14) \times 10^{-6}$	$(5.16 \pm 0.15) \times 10^{-6}$
FWHM (′)	7.35 ± 0.25	—	—
η_{Beam}	0.658 ± 0.024	—	—
$\eta_{Ap.}$	0.476 ± 0.017	—	—
T_J (K)	152 ± 5	144 ± 8	—^{A}
f	1.0	1.037	1.112

^{A} Calibrated with $S_{DR21} = 18.24 \pm 0.55$; see § 6.4.1

Table 6.2: Summary of telescope parameters we adopt, as well as those necessary to reference previous observations onto this calibration scale and the factor f which accomplishes this.

6.4 Summary of Previous Observations

6.4.1 Coma

The OVRO 5.5-meter was first used for SZE observations by Herbig et al. (1995), who measured the SZ decrement of the Coma cluster. Referring the observed antenna temperature difference to the main beam of the telescope, and including a 34.7μK correction for discrete source contamination, Herbig et al. find $\Delta T_{obs} = -302 \pm 48 \mu K$. These results have been extrapolated to zero-frequency by multiplying the actual observed equivalent temperature difference by 1.054; this yields the equivalent temperature difference which would be observed on the cluster in the Rayleigh-Jeans (R-J) limit:

$$\frac{\Delta T_{eq,sw}}{T_{cmb}} = -2\, y_{sw}. \tag{6.10}$$

The main beam area assumed was $\Omega_{Beam} = (5.16 \pm 0.15) \times 10^{-6}$ Sr, and the data were calibrated relative to DR21 assuming $S_{DR21} = 18.24 \pm 0.55$ Jy at 32.0 GHz (Klein & Gulkis 1978). From the stated R-J equivalent temperature, we calculate $y_{sw} = (5.54 \pm 0.88) \times 10^{-5}$. Note that the uncertainty in this value includes the uncertainty in the beam-area determination, but not the flux-scale uncertainty.

We recalibrate this observation by referencing it onto the Myers et al. (1997) flux density scale using DR21, and using Jupiter to tie this with our current scale. The Coma data are calibrated assuming $S_{DR21} = 18.24 \pm 0.55$ Jy; comparing this to the average flux density obtained by Myers et al. of $S_{DR21} = 19.4 \pm 1.1$ Jy , this results in a correction of 12.3% to the Coma calibration. Both of the error bars in these flux densities are dominated by overall uncertainties in the flux density scale. Allowing for the main beam area assumed in translating the original result to an equivalent temperature, we derive an overall multiplicative correction $f = 1.112$. The resulting observed Compton y-parameter, fully referenced onto the present calibration, is $y_{sw} = (6.16 \pm 0.98) \times 10^{-5}$. Using Equation 2.55 and $kT_e = 9.1$, keV, we compute $\chi_{rel} = 1.035$, yielding a corrected switched Compton y-parameter of $y_{sw} = 6.38 \pm 1.01$.

6.4.2 A478, A2142, and A2256

A478, A2142, and A2256 were observed by Myers et al. (1997) from July 1993 to March 1994 resulting in observed decrements of $-375 \pm 28, -437 \pm$

25, and $-243 \pm 29\,\mu$K respectively; these temperature are again referred to the main beam, and have been corrected for point-source contamination. These data were calibrated using a brightness temperature of $T_J = 144 \pm 8$ K for Jupiter (Wrixon et al. 1971). Including the correction for the main beam area, we find an overall correction of $f = 1.037$ for the Myers et al. data. The stated decrements yield switched, beam-averaged Compton y-parameters of $(7.25{\pm}0.54){\times}10^{-5}$, $(8.44{\pm}0.48){\times}10^{-5}$, and $(4.70{\pm}0.56){\times}10^{-5}$, respectively. Applying the relativistic corrections ($\chi_{rel} = 1.033$, 1.037 , and 1.026) together with our calibration correction, we find Compton y-values of $(7.77 \pm 0.58) \times 10^{-5}$, $(9.10 \pm 0.52) \times 10^{-5}$, and $(5.00 \pm 0.60) \times 10^{-5}$.

6.5 New Observations

From September of 1996 through February 1999, SZE observations were conducted on the OVRO 5.5-meter telescope. The goal of these observations was to significantly extend the coverage of the 11-cluster SZE survey begun by Myers et al. (1997). Clusters targeted for observation included A85, A399, A401, A754, A1651, and A2029. Unfortunately, two years of consistently sub-standard observing conditions (including an El Niño year, 1997-98), one season of repeated failures in the aging 5.5-meter drive systems (1998-99), and the relatively greater challenge of measuring the SZE in the less luminous clusters made this slow going, and we obtained reliable results only on a small fraction of the clusters we attempted. We report here the results of measurements on A399 and A1651, taken from October 1996 through March 1997, and A401, taken from October 1997 through March 1998. Of these, A401 and A1651 may require some further confirmation.

We list the LEAD, MAIN, and TRAIL coordinates employed for A399, A401, and A1651 in Table 6.3.

6.5.1 Data Reduction

While the 5.5-meter telescope operates essentially continuously during the observing season, only a small fraction of the data collected are actually useful for measuring the SZE due to the strongly atmosphere-limited nature of our observations. Reliable and robust filtering techniques are therefore indispensable in interpreting the data we collect. We adopt the data filtering and weighting procedures developed by Myers et al. (1997), which have also

Source	RA	Dec.
A399L26	02:31:52.05	+13:02:46.20
A399	02:57:52.05	+13:02:46.20
A399T26	03:23:52.05	+13:02:46.20
A401L17	02:42:21.0	+13:34:39.13
A401	02:58:57.0	+13:34:39.13
A401T17	03:15:33.0	+13:34:39.13
A1651L20	12:38:51.5	−04:11:31.00
A1651	12:59:21.5	−04:11:31.00
A1651T20	13:19:51.5	−04:11:31.00

Table 6.3: Field positions used in observations of A399, A401, and A1651. All coordinates are epoch J2000.

been used with good results by Leitch (1998). Here we summarize these procedures as applied to the data sets at hand; a more detailed exposition of the methods can be found in these references.

In order to avoid biasing the results, our filtering and weighting algorithms use the standard deviations in the individual data points and the scatter amongst them— rather than their actual values— to eliminate or down weight stretches of low-quality data. The only exceptions to this are an initial sun/moon rejection and a final 4 σ outlier edit that removes a negligible fraction of the data. In the order that we apply them, our filters are:

- **Sun/Moon rejection:** In order to eliminate data potentially affected by solar or lunar emission in the telescope sidelobes, all scans within 30° of either of these sources are eliminated.

- **Cal referencing:** Raw power differences are converted into antenna temperature differences by referencing them onto the observed cal diode powers. In practice, each data point is referenced onto an average of all of the cal measurements within a time window of 1 hour centered on the data point; if any of the cal values show fluctuations greater than 10% from the mean, that datum is rejected. This initial filtering tends to reject periods of very bad data (e.g., when the radiometry was saturated due to rainy weather). The A401 were data were collected after the REF side load switch was removed, and so are somewhat more sensitive to such conditions.

- **Mean SD:** The mean of the standard deviations of the nearest $10-25$ FLUX measurements within a time window of 2 hours centered on each data point is computed, and if this is greater than twice the expected thermal SD, that datum is rejected. This is the workhorse of filters, which eliminates stretches of data strongly to moderately affected by the atmosphere.

- **Thermal SD:** Although the Mean SD filtering eliminates periods of bad data, it will not catch individual data points affected by either atmospheric fluctuations, interference, or instrumental glitches. The thermal SD filter catches these by removing individual data whose SD's are greater than 2.5 times the thermal expectation.

- **Switched Difference:** By differencing the FLUX segments which observed the *same* patches of sky, the sky signal can be cancelled leaving only time variations in the atmosphere or other non-celestial signals. All data for which this quantity, averaged in a $7-10$ point buffer centered on each data point, is greater than 7.5 times thermal are rejected. This rejects a small fraction of grossly discrepant data.

- **Outlier Rejection:** A $4-\sigma$ outlier rejection is performed on the final, fully referenced LEAD-MAIN-TRAIL data. The rejection is done iteratively, by rejecting the most discrepant data point and then recalculating the standard deviation for the data set as a whole, in order to avoid biasing the results. This typically results in the rejection of fewer than 5 in ~ 1000 data points.

Note that while most of these filters reject data on the basis of variability of the data on times scales between that of a single FLUX segment (~ 15 seconds — the Mean SD filter) and four times that (the Switched Difference filter), atmospheric emission can cause signals which vary on timescales much greater than this. In order to reduce the influence of such signals on our data, we weight the data based on the scatter of the data values in a 2-hour buffer; our results are insensitive to the choice of the length of this buffer for buffer lengths between 45 minutes (about the length of one scan) and 2 hours. Each data point j is assigned a weight

$$w_j = \frac{1}{\sigma_j^2 + \sigma_{sc,j}^2} \tag{6.11}$$

where σ_j is the standard deviation of that datum and $\sigma_{sc,j}$ is the standard deviation in the data values computed in a 2 hour buffer centered on the datum. This down-weighting effectively rejects $\sim 30\%$ of the data on average, which is slightly less than the Mean SD filtering rejects, but more than is rejected by any of the other filters. Tables 6.4 , 6.5, and 6.6 summarize the edits and weighting applied to the data for A399, A401, and A1651. The "Fraction Rejected" shown in these tables is the fraction of the *remaining* data rejected at each stage. Also listed are data points lost due to failed LEAD-MAIN-TRAIL referencing, which occurs when any of the three points in the matched scans are either flagged or missing. The latter is typically due to occasional encoder or drive problems with the telescope. Table 6.7 summarizes this by showing the fraction f of data accepted by our filters the total integration time τ (including ANT and REF data on the LEAD, MAIN and TRAIL fields), along with f' and $\tau\,'$ which incorporate the effects of the post-filter data weighting.

Data were calibrated relative to the supernova remnant Cas A, which was observed every 1-2 days throughout our SZ program. Chapter 5 has presented an absolute flux density measurement for this object; however, its finite extent relative to the 5.5-meter beam implies that the observed flux density will be less than this. Using the Leitch (1998) form-factor for Cas A described in § 5.5 and our measurement $S_{cas} = 194^{+5}_{-6}$ Jy (epoch spring 1998), we find

$$S_{cas,5.5-m} = 164.4 \pm 5.0\,\mathrm{Jy}. \tag{6.12}$$

This is the value we use to calibrate the 1997 – 1998 SZE observations; 1996/97 data were calibrated by a value 0.5% higher than this to allow for the estimated secular variation of Cas A; see § 5.5. Calibration is performed by referencing observations of Cas A onto (fully referenced, filtered, and weighted) cluster observations occurring within 2 days of each other; the mean equivalent temperature of Cas A is then computed for the season as a whole using the L-M-T weighting and a fiducial value for T_{Cal}. Using our adopted sensitivity $\Gamma = 4.10$ mK/Jy and $\eta_{Beam} = 65.8\%$, a fiducial value for S_{cas} is calculated. This, in comparison with Eq. 6.12, is used to calculate the true T_{Cal} over this period. For A399, this results in $T_{Cal} = 0.375$ K; for A1651, $T_{Cal} = 0.381$ K; and for A401, $T_{Cal} = 0.346$ K. The 10% difference between the 1996/97 value for T_{Cal} and that for 1997/98 is not surprising given that there were several major changes to the receiver in the intervening period, including the disconnection of one cal diode and the replacement of the main Dicke switch with the former REF-side load switch. There is no evidence of T_{Cal} fluctuations within any individual season beyond the $\sim 1\%$ level mentioned previously. As a cross check on our calibration, DR 21 was also observed regularly. The ratio S_{DR21}/S_{cas}, with S_{DR21} corrected to the peak flux density as per the prescription of Leitch (1998), is consistent with the flux density ratio Leitch observes to within 0.2%.

All data are corrected for receiver nonlinearity (Herbig 1994; Leitch 1998). In practice, our results are identical whether or not we make this correction. This is due to the fact that calibrator and SZ observations are taken in the same manner, and will therefore contain only a common nonlinearity factor. This is true even for the 1996/97 data, for which CAL procedures were executed against the somewhat higher background power given by the internal waveguide loads.

Table 6.9 summarizes our final referenced results for A399, A401, and A1651. In this table, MLT is the fully referenced (MAIN $-$ (LEAD $+$ TRAIL) /2) result for the cluster; LTD is the difference between the LEAD and TRAIL fields; LTA is the average of the LEAD and TRAIL fields; ML is the difference between the MAIN and LEAD fields; and MT is the difference between the MAIN and TRAIL fields.

Since A399 and A401 lie at a relative separation of only $37'$, it is necessary to correct the measurements of each of these clusters for the signal of the other which occurs in the REF beam of the telescope for some hour angles. Based on the individual SZE measurements and the cluster models of Chapter 4, we estimate $+22 \pm 6\,\mu$K and $+10 \pm 2\,\mu$K contaminating signals for the A399 and A401 observations respectively. These corrections have been applied to the data in Table 6.9.

Figures 6.2 through 6.7 show the fully calibrated and corrected data as a function of parallactic angle. The even numbered tables show the field (LEAD/MAIN/TRAIL) data, with the MAIN field shown as a filled circle and the LEAD and TRAIL fields as empty circles. The odd-numbered figures show the referenced results, with MLT shown as filled circles and LTD as empty circles.

Filter	Start	Rejected	Fraction Rejected
Sun	10741	0	0
Moon	10741	1970	18.3 %
Cal Ref.	8771	955	10.9%
Mean SD	7816	3255	41.6%
Thermal SD	4561	131	2.9%
SWD	4430	3	0.1%
LMT Ref.	4427	989	22.3%
LMT Outlier	1146	3	0.3%
Weighting	1143	—	32.2%

Table 6.4: A399 data edits.

Filter	Start	Rejected	Fraction Rejected
Sun	12256	0	0
Moon	12256	1755	14.3%
Cal Ref.	10501	1749	16.6%
Mean SD	8752	3496	39.9%
Thermal SD	5256	201	3.8%
SWD	5055	4	0.1%
LMT Ref.	5051	1016	20.1%
LMT Outlier	1345	4	0.3%
Weighting	1341	—	34.9%

Table 6.5: A401 data edits.

Filter	Start	Rejected	Fraction Rejected
Sun	12592	2158	17.1%
Moon	10434	2348	22.5%
Cal Ref.	8086	287	3.5%
Mean SD	7799	3493	44.8%
Thermal SD	4305	328	7.6%
SWD	3977	0	0
LMT Ref.	3977	1007	25.3%
LMT Outlier	990	3	0.3%
Weighting	987	—	36.9 %

Table 6.6: A1651 data edits.

Cluster	f	τ (hrs)	f'	τ' (hrs)
A399	31.9%	58.7	21.5%	39.8
A401	32.8%	66.0	21.3%	42.8
A1651	23.5%	39.5	14.8%	24.9

Table 6.7: Summary of the overall fraction f of data accepted by our filters and the corresponding total integration time for our result, along with the effective fraction f' and integration time τ' after weighting.

	A399	A401	A1651
MLT (μK)	-140 ± 20	-316 ± 20	-242 ± 30
LTD (μK)	15 ± 21	120 ± 23	-92 ± 36
LTA (μK)	126 ± 14	160 ± 14	-46 ± 22
ML (μK)	-142 ± 21	-391 ± 22	-217 ± 32
MT (μK)	-164 ± 22	-268 ± 21	-287 ± 36

Table 6.8: Observed SZE results on A399, A401, and A1651.

	A399	A401	A1651
MLT (μK)	-187 ± 21	-348 ± 23	-247 ± 30
LTD (μK)	12 ± 21	133 ± 24	-83 ± 36
LTA (μK)	127 ± 14	154 ± 16	-39 ± 22
ML (μK)	-187 ± 22	-430 ± 23	-227 ± 32
MT (μK)	-213 ± 23	-295 ± 21	-287 ± 36

Table 6.9: SZE results on A399, A401, and A1651, including point source corrections and (for A399 and A401) corrections for emission from the neighboring cluster.

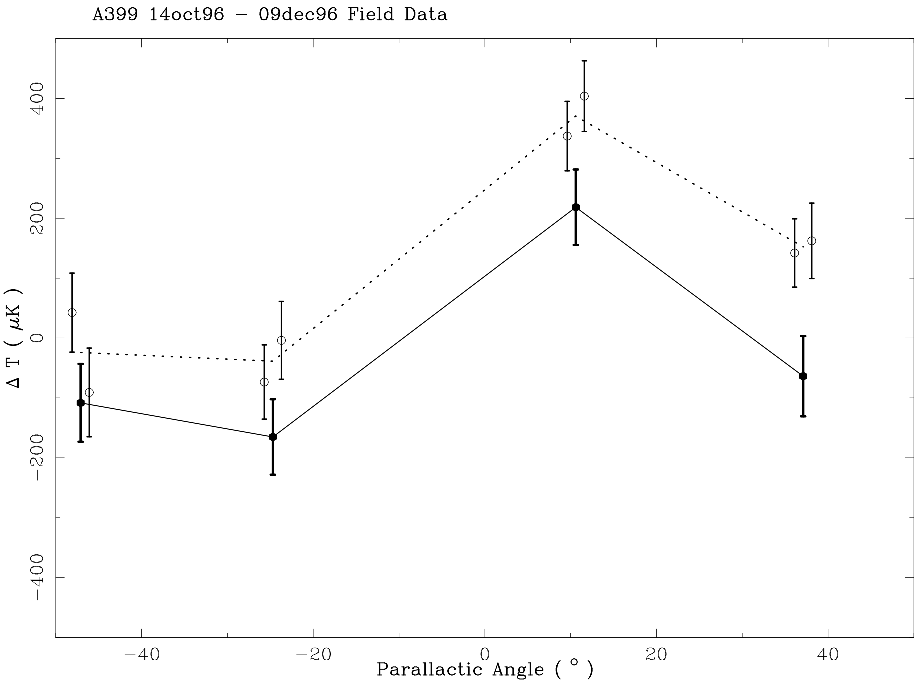

Figure 6.2: L/M/T SZ data for A399.

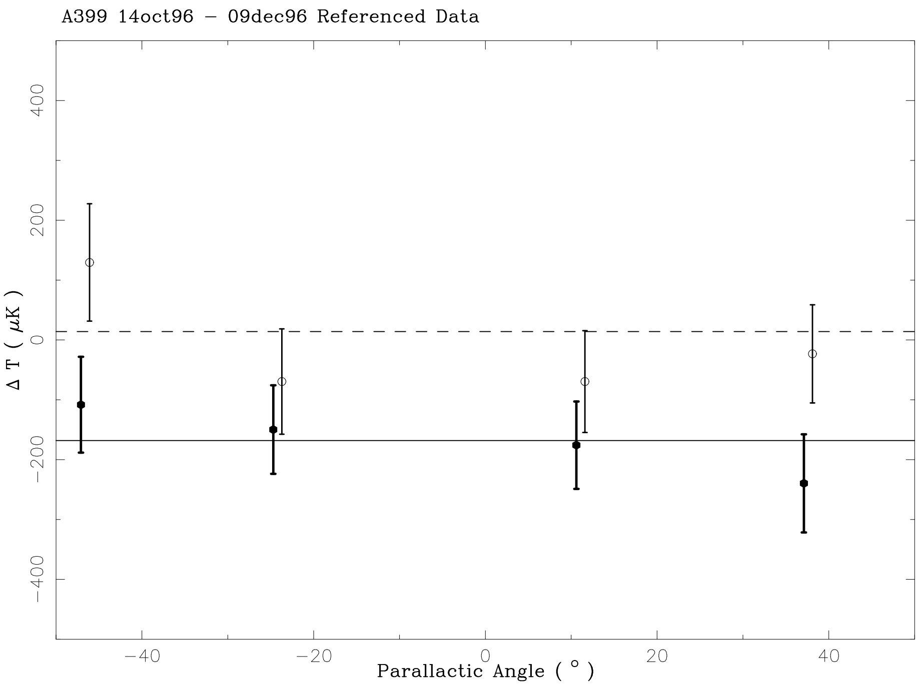

Figure 6.3: Referenced SZ data for A399.

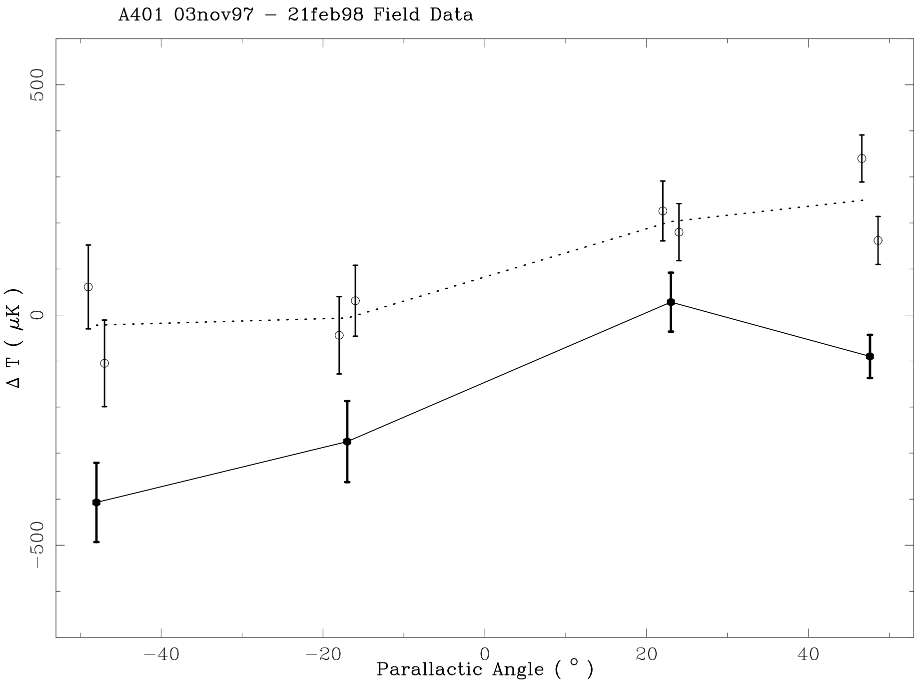

Figure 6.4: L/M/T SZ data for A401.

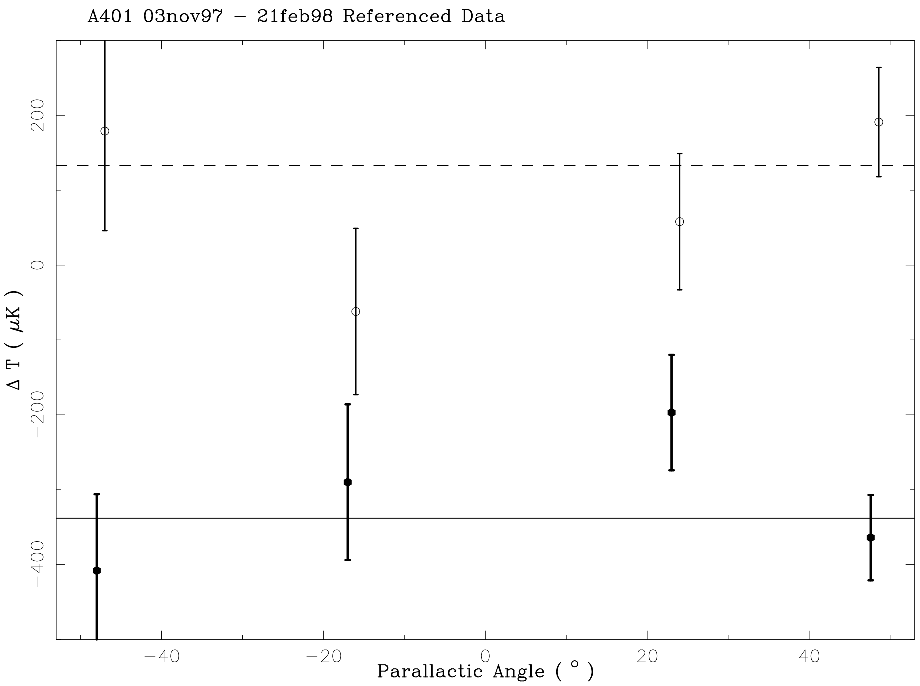

Figure 6.5: Referenced SZ data for A401.

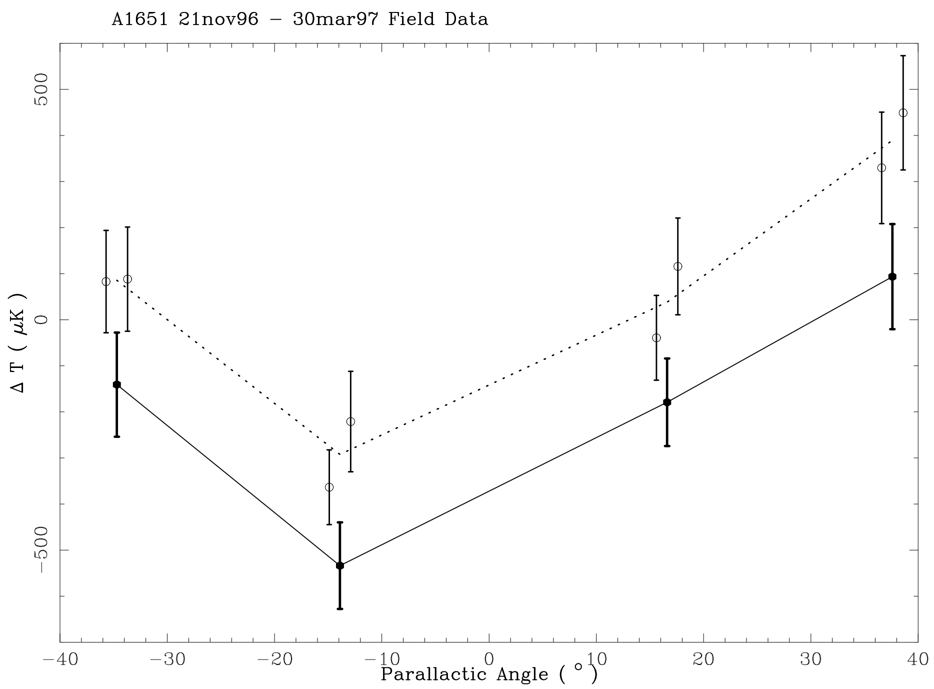

Figure 6.6: L/M/T SZ data for A1651.

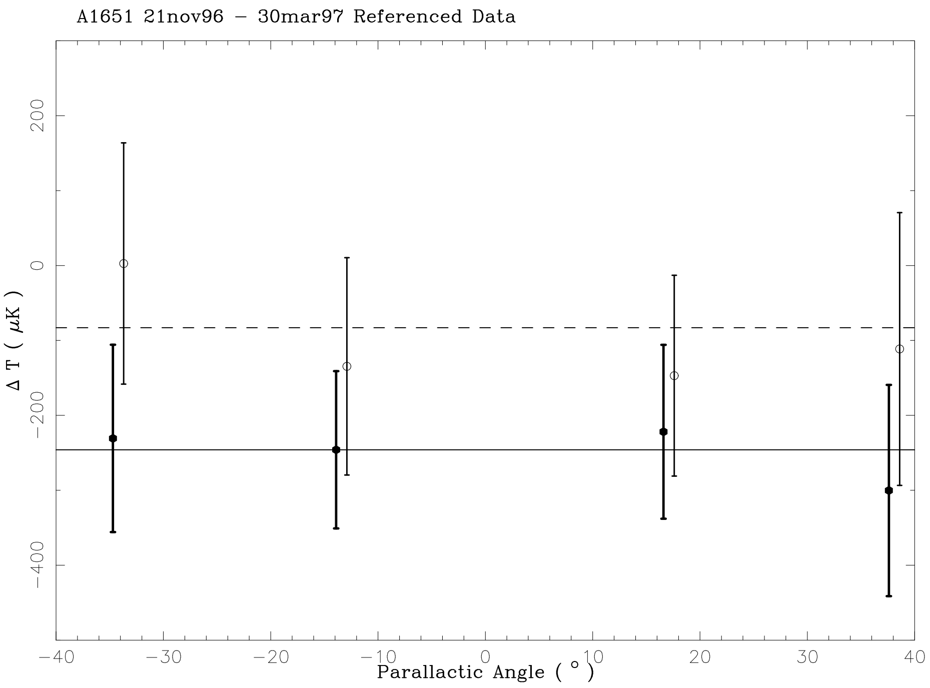

Figure 6.7: Referenced SZ data for A1651.

	η_{Obs}	η_{Gauss}	ΔT_o (μK)	χ_{rel}	y_{obs} (10^{-5})
A399	57.7%	81.2%	-322 ± 23	1.027	3.70 ± 0.42
A401	45.5%	76.4%	-765 ± 50	1.031	6.52 ± 0.43
A478	28.8%	83.8%	-1350 ± 101	1.033	7.77 ± 0.58
A1651	42.9%	86.0%	-573 ± 70	1.023	4.88 ± 0.59
A1656	52.8%	57.9%	-636 ± 100	1.035	6.38 ± 1.01
A2142	38.6%	81.2%	-1173 ± 67	1.037	9.10 ± 0.52
A2256	62.6%	84.6%	-402 ± 48	1.026	5.00 ± 0.60

Table 6.10: Summary of observational results on all clusters. ΔT_o does not include the effects of model uncertainties or cooling flow components, so is meant only to be indicative of the magnitude of the central decrement. Compton y-parameters have been corrected by the stated values of χ_{rel}.

6.5.2 Discrete Source Contamination

On arcminute scales at 30 GHz the dominant contaminating celestial signals are due to discrete radio sources, mostly radio galaxies and quasars. Myers et al. (1997) used the 87GB (Gregory & Condon 1991) and PMN (Griffith & Wright 1993) radio surveys, both at 4.85 GHz, to identify possibly confusing point sources. These sources were then observed at 18.5 GHz with the OVRO 40-m telescope, and the resulting fluxes subtracted from the data assuming a flat-spectrum extrapolation to 32 GHz. Unfortunately, these surveys have flux limits of 25 mJy, making the possibility of contamination by faint flat or inverted spectrum sources somewhat of a concern. The release of the NRAO VLA All Sky Survey (NVSS) data (Condon et al. 1998) has greatly improved this situation[3]. The NVSS is a 1.4 GHz all-sky survey which is complete to $\sim$ 2.5 mJy. This allows a dramatically improved safeguard against flat-spectrum sources; even for strongly inverted sources ($\alpha = +1$), we achieve nearly a factor of three improvement in sensitivity over using 87GB/PMN alone.

In the Fall of 1997, we undertook a program to identify and measure potentially contaminating point sources in the LEAD, MAIN, and TRAIL fields

[3]Note that while the date of the official NVSS publication is 1998, the data was made publicly available over the Internet as soon as the data were reduced and verified. Thus the reader is assured that the Fall 1997 observations which we describe herein were strictly causal in nature.

of A85, A399, A401, A754, A1651, A1795, and A2029. The identification was based on NVSS; the measurements were taken with the OVRO 40-m at 18.5 GHz. Sources were selected as follows. First, all sources in the NVSS within $30'$ of these 21 fields were extracted from the catalog using the NVSSLIST program. This resulted in 270 sources. For each field, and assuming a spectral index of $\alpha = +0.2$, we then calculated the equivalent temperature which would result given the 5.5-meter beam pattern and sensitivity. Sources in the ON beams which contribute $\Delta T < 30\,\mu$K were discarded, and sources in the REF beams which contribute less than twice this (when closest to the REF beam center) were also discarded; *any* sources, however, which were within $12'$ of the ON beam center and had 1.4 GHz fluxes greater than 50 mJy were retained. Note that while the $30\,\mu$K antenna temperature limit for $\alpha = +0.2$ is somewhat less stringent than what one may desire, this corresponds to a 1.4 GHz flux of ~ 4 mJy— already close to the NVSS completeness limit. At the end of this selection process, we had a total of 68 sources.

During October and November of 1997, we observed these 68 sources with the 40-meter telescope. The data were calibrated relative to 3C286 using the Baars et al. (1977) value $S_{3C286}(18.5\,\mathrm{GHz}) = 2.94$ Jy; this source was observed regularly during the period of observations. If we compare this to the observed *antenna temperatures*, calibrated relative to an internal noise calibration diode whose effective brightness temperature is independently determined to be $T_{Cal} = 0.991 \pm 0.004$, we find that the sensitivity is $\Gamma = 142.6 \pm 1.6$ mK/Jy. The 40-m telescope flexes slightly as it tracks sources across the sky, resulting in a significant variation of the telescope gain as a function of zenith angle. This was corrected for by dividing the data by a gain curve derived from long tracks on bright sources. Following Myers et al. (1997), we estimate an overall uncertainty of 6% in the 18.5 GHz calibration.

Since the NVSS was taken at a significantly higher angular resolution than the $1'.8$ FWHM of the 40-meter beam, in a few cases source confusion was a problem. If two sources separated by a distance δ on the sky are individually targeted for observation by a telescope with a resolution σ, the two observed fluxes $(S_{obs,1}, S_{obs,2})$ are related to the true fluxes (S_1, S_2) by

$$\begin{pmatrix} S_{obs,1} \\ S_{obs,2} \end{pmatrix} = \begin{pmatrix} 1 & e^{-\delta^2/2\sigma^2} \\ e^{-\delta^2/2\sigma^2} & 1 \end{pmatrix} \begin{pmatrix} S_1 \\ S_2 \end{pmatrix} \tag{6.13}$$

Therefore if we know the source positions, the beam width, and the observed fluxes, we can invert the matrix and obtain the true fluxes. As $\delta \to 0$ this matrix is singular, but in this limit a single measurement of the two sources is sufficient. For sources with separations comparable to the main beam, failing to account for source confusion will systematically overestimate the level of discrete source contamination. We correct our observed fluxes for confusion by inverting the matrix equivalent to that in Eq. 6.13 but which includes all sources within 2 Gaussian beam widths of any given source. Errors are determined by directly propagating the errors on the individual source fluxes. Note that the deconfusion process correlates the errors between individual source fluxes, so the uncertainty in our final point source subtraction for any given cluster is likely to be slightly overestimated. For sources that are closely spaced, the individual flux densities obtained by this procedure are not meaningful due to the amplification of measurement noise, but the sum of the two should be a good approximation to the true total flux density. In this case we grouped the sources together and assigned a flux density equal to the sum of the individual deconfused fluxes[4]. Overall, there were 29 out of 68 sources were confused; deconfusing the observed values often resulted in quite significant corrections to the individual flux densities.

Table 6.11 shows our 18.5 GHz flux density measurements for the 30 sources found in the LEAD, MAIN, and TRAIL fields of A399, A401, and A1651. Also shown are the NVSS flux densities and the 87GB/PMN flux densities where available. Some sources (such as 125948-0354) show clear evidence of variability; these sources are denoted by a "*". The results for the remaining clusters are in Appendix E

We extrapolate these fluxes to 32 GHz using the NVSS and 18.5 GHz data by assuming a power law of the form

$$S_\nu = S_o \left(\frac{\nu}{\nu_o} \right)^\alpha . \tag{6.14}$$

For sources with clear signs of variability (025806+132 , 025831+1334, 025937+1354, and 125948-0354), we instead use a flat-spectrum extrapolation from 18.5 GHz. While there may be some level of variability in the other sources, to consistently assume $\alpha = 0$ would systematically bias our final results since the emission from most discrete sources is due to synchrotron radiation with $\alpha \sim -0.7$. This consideration is more important as

[4]While it would be of some interest to study the stability of the solutions so obtained for $S_1 + S_2$ with respect to the addition of a noise vector on the left-hand side of Eq. 6.13, the 5.5-meter discrete source equivalent temperatures are not sensitive to subtleties at this level so this has not been attempted.

deeper surveys allow the identification of a greater number of contaminating sources per cluster. For sources with only NVSS and 18.5 GHz flux densities, we solved analytically for α using Eq. 6.14 and determined the uncertainties using standard propagation of errors; for sources which also had 4.85 GHz data, we fit the data to this function and determined the uncertainties from the diagonal elements of the covariance matrix. The resulting 32 GHz flux densities are shown in Table 6.12.

Since these observations were not contemporaneous with the 5.5-meter observations of A399 and A1651 some extra precautions are in order for the sources in these two clusters. Fortunately, two months of observations were conducted in Fall of 1996 (November and December) which allowed us to deal with the most potentially troublesome sources. Of particular concern are 025737+1300 in A399, a ~ 10 mJy source $4'.11$ from the center of the ON beam, and 125948-0354, the brightest (~ 50 mJy) known contaminating source in these three clusters which lies $6'.8$ from a REF beam in the MAIN field on A1651. These two sources had been previously identified from 87GB and were thus included in these observations. We use the Fall 1996 fluxes for these two sources, calibrated relative to the Baars et al. (1977) value for the flux density of 3C123, $S_{3C123} = 4.51$ Jy. These values are the ones shown in Table 6.12. The other sources in these clusters are all significantly weaker and lie in the REF beams.

Table 6.13 shows the *maximum* equivalent temperature generated by each of the identified sources in A399, A401, and A1651, along with the field and beam with which it is associated, its flux in mJy, its distance R from the center of the ON beam, the distance d of closest approach to any beam, and its position angle. Table 6.14 summarizes the discrete source contamination in each field; the $T_{ref,avg}$ results stated here have been averaged over a full track. This averaging substantially reduces the degree to which sources in the ref arcs influence our results; even for a cluster like A401, which relatively speaking has heavily contaminated REF arcs, the correction and the uncertainty therein are heavily dominated by a single source near the ON beam.

Source	RA	Dec.	$S_{18.5}$ mJy	$S_{4.85}$ mJy	$S_{1.4}$ mJy
023217+1244	02:32:17.35	12:44:59.1	4.41 ± 0.68	34.0 ± 5.0	79.30 ± 1.70
023232+1247	02:32:32.88	12:47:15.9	3.56 ± 0.97	—	23.60 ± 1.50
025618+1309	02:56:18.23	13:09:29.4	10.27 ± 1.80	52.0 ± 5.0	91.90 ± 7.90
025711+1325	02:57:11.77	13:25:16.1	3.32 ± 1.01	—	44.80 ± 2.20
025737+1300	02:57:37.20	13:00:49.3	14.06 ± 1.54	33.0 ± 5.0	47.90 ± 1.10
032233+1317	03:22:33.77	13:17:21.3	3.40 ± 1.13	—	15.10 ± 0.50
024131+1339	02:41:31.44	13:39:54.8	5.56 ± 0.97	—	96.70 ± 4.30
024212+1335	02:42:12.85	13:35:43.3	6.20 ± 0.99	—	15.00 ± 1.40
024251+1322	02:42:51.37	13:22:14.7	16 ± 2.6	—	150.70 ± 6.60
025806+1352*	02:58:06.70	13:52:39.2	10.02 ± 3.10	41 ± 11	24.70 ± 1.90
025810+1351	02:58:10.39	13:51:50.1	17.12 ± 6.38	—	72.60 ± 3.30
025811+1350	02:58:11.97	13:50:42.7	8.86 ± 3.25	—	24.20 ± 3.00
025831+1334*	02:58:31.89	13:34:17.3	35.70 ± 5.87	164 ± 23	68.70 ± 11.80
025835+1242	02:58:35.3	12:42:28	2.9 ± 1.1	—	43 ± 5
025915+1327	02:59:15.17	13:27:58.9	14.5 ± 1.4	—	54.70 ± 3.60
025937+1354*	02:59:37.57	13:54:36.5	28.14 ± 2.93	195 ± 27	75.10 ± 16.30
025939+1355	02:59:39.33	13:55:24.2	39.58 ± 2.47	—	31.80 ± 14.50
025941+1354	02:59:41.66	13:54:08.1	3.31 ± 2.30	—	9.80 ± 2.00
031510+1320	03:15:10.23	13:20:32.5	7.45 ± 1.37	—	75.20 ± 3.40
125948-0354*	12:59:48.55	-03:54:35.1	54.99 ± 1.31	115 ± 5	76.80 ± 2.40
130026-0350	13:00:26.18	-03:50:43.7	7.12 ± 1.29	—	31.40 ± 1.10
123804-0429	12:38:04.08	-04:29:21.6	6.54 ± 0.97	—	6.10 ± 0.60
123949-0405	12:39:49.02	-04:05:30.3	10.82 ± 0.94	—	92.60 ± 2.80
124005-0430	12:40:05.66	-04:30:05.5	9.67 ± 0.74	—	65.10 ± 2.40
124009-0420	12:40:09.19	-04:20:56.2	14.01 ± 0.95	—	84.40 ± 2.90
124010-0429	12:40:10.29	-04:29:13.2	5.64 ± 0.88	—	33.70 ± 1.50
124012-0412	12:40:12.81	-04:12:21.9	5.26 ± 1.18	—	10.90 ± 0.60
132107-0433	13:21:07.17	-04:33:02.6	3.54 ± 0.95	—	69.60 ± 2.50
132114-0401	13:21:14.82	-04:01:08.0	4.25 ± 0.72	—	19.50 ± 1.20
132142-0405	13:21:42.08	-04:05:56.0	7.38 ± 1.13	—	81.60 ± 2.90

Table 6.11: NVSS-selected point sources in the LEAD, MAIN, and TRAIL fields of A399, A401, and A1651. Shown are our deconfused 18.5 GHz flux densities (Epoch Fall 1997), the 4.85 GHz (PMN or 87GB) flux densities where available, and the NVSS flux densities. Sources marked with "*" show clear signs of variability.

Source	α	S_{32} mJy
023217+1244	-1.06	2.9 ± 0.4
023232+1247	-0.73	2.4 ± 0.8
025618+1309	-1.1	6.3 ± 0.7
025711+1325	-1.01	1.9 ± 0.7
025737+1300	—	$(8.9 \pm 0.1)^A$
032233+1317	-0.58	2.5 ± 1.0
024131+1339	-1.11	3.0 ± 0.6
024212+1335	-0.34	5.1 ± 1.0
024251+1322	-0.87	9.9 ± 2.0
025806+1352	—	$(10.0 \pm 3.1)^B$
025810+1351	-0.56	12.6 ± 5.7
025811+1350	-0.39	7.2 ± 3.2
025831+1334	—	$(35.7 \pm 5.9)^B$
025835+1242	-2.01	1.0 ± 0.5
025915+1327	-0.51	10.9 ± 1.3
025937+1354	—	$(28.1 \pm 2.9)^B$
025939+1355	-0.82	25.2 ± 1.9
025941+1354	-0.42	2.6 ± 2.2
031510+1320	-0.90	4.6 ± 1.0
125948-0354	—	$(78.3 \pm 0.4)^A$
130026-0350	-0.57	5.2 ± 1.1
123804-0429	0.03	6.6 ± 1.2
123949-0405	-0.83	6.9 ± 0.7
124005-0430	-0.74	6.4 ± 0.6
124009-0420	-0.70	9.8 ± 0.8
124010-0429	-0.69	3.9 ± 0.7
124012-0412	-0.28	4.5 ± 1.2
132107-0433	-1.15	1.9 ± 0.6
132114-0401	-0.59	3.1 ± 0.6
132142-0405	-0.93	4.4 ± 0.8

^{A} Epoch Fall 1996 flux (see text).
^{B} Flat-spectrum extrapolation from 18.5 GHz.

Table 6.12: 32 GHz flux densities for the sources in Table 6.11.

Field(beam)	Source	S_{32} (mJy)	T_{eq} (μK)	R $'$	d $'$	PA $^\circ$
A399L(ref)	023217+1244	2.9 ± 0.4	-2	18.82	6.61	160.9
A399L(ref)	023232+1247	2.4 ± 0.8	-7	18.42	3.94	147.3
A399(ref)	025618+1309	6.3 ± 0.7	-34	23.81	1.65	286.4
A399(ref)	025711+1325	1.9 ± 0.7	-3	24.54	5.44	336.5
A399(on)	025737+1300	8.9 ± 0.1	23	4.11	4.11	241.7
A399(ref)	025835+1242	1.0 ± 0.5	-4	22.87	3.14	152.5
A399(ref)	025915+1327	10.9 ± 1.3	0	32.32	10.16	38.7
A399T(ref)	032233+1317	2.5 ± 1.0	-13	24.00	1.84	307.5
A401T(ref)	031510+1320	4.6 ± 1.0	-1	15.16	8.22	201.4
A401(ref)	025711+1325	1.9 ± 0.7	-3	27.2	5.09	249.9
A401(ref)	025806+1352	10.0 ± 3.1	-58	21.7	1.19	325.9
A401(ref)	025810+1351	12.6 ± 5.7	-63	20.5	2.06	326.6
A401(ref)	025811+1350	7.2 ± 3.2	-29	19.4	2.91	325.8
A401(on)	025831+1334	35.7 ± 5.9	33	6.1	6.11	266.6
A401(on)	025915+1327	10.9 ± 1.3	3	8.0	8.00	146.5
A401(ref)	025937+1354	28.1 ± 2.9	-91	22.2	3.56	26.3
A401(ref)	025939+1355	25.2 ± 1.9	-76	23.1	3.75	26.3
A401(ref)	025941+1354	2.6 ± 2.2	-12	22.3	2.37	29.1
A401L(ref)	024131+1339	3.0 ± 0.6	-02	15.17	6.99	290.3
A401L(on)	024212+1335	5.1 ± 1.1	12	4.30	4.30	284.4
A401L(ref)	024251+1322	9.9 ± 2.0	-1	13.45	9.50	157.3
A1651L(ref)	123804-0429	6.6 ± 1.2	-36	21.40	1.68	213.5
A1651L(ref)	123949-0405	6.9 ± 0.7	-5	15.55	6.61	67.3
A1651L(ref)	124005-0430	6.4 ± 0.6	-17	26.21	4.05	135.1
A1651L(ref)	124009-0420	9.6 ± 0.8	-58	21.54	0.62	115.9
A1651L(ref)	124010-0429	3.9 ± 0.7	-9	26.44	4.28	132.0
A1651L(ref)	124012-0412	4.5 ± 1.2	-23	20.29	1.87	92.4
A1651(ref)	125948-0354	78.3 ± 10.0	-45	18.23	6.82	21.7
A1651(ref)	130026-0350	5.2 ± 1.1	-13	26.31	4.15	37.8
A1651T(ref)	132107-0433	1.9 ± 0.6	-1	28.62	6.46	138.8
A1651T(ref)	132114-0401	3.1 ± 0.6	-18	23.23	1.07	63.5
A1651T(ref)	132142-0405	4.4 ± 0.8	-4	28.13	5.97	78.6

Table 6.13: Summary of significant contaminating discrete sources for A399, A401, and A1651. In addition to the source name, field, flux density, and equivalent temperature, the distance R from the center of the on beam and the distance of closest approach "d" to the most-affected beam are also shown.

Field	N_{src}	Flux	T_{on}	T_{ref}(max)	T_{ref}(avg.)	T_{tot}
		mJy	μK	μK	μK	μK
A399L	2	5.3	0.0	-7	0.0	0.0
A399	5	29.0	23.3	-34	0.0	23.1 ± 1.6
A399T	1	2.5	0.0	-13	-5.8	-3.0 ± 1.2
A401T	1	4.6	0.0	-1	0.0	0.0
A401	9	134.2	35.2	-145	-13.3	28.6 ± 10
A401L	3	18.1	12.4	-2	0.0	12.3 ± 5.3
A1651L	6	37.9	0.0	-58	-21.7	-10.8 ± 0.6
A1651	2	83.5	0.0	-45	-1.8	-1.0 ± 0.1
A1651T	3	9.4	0.0	-18	-3.5	-1.7 ± 0.2

Table 6.14: Total discrete source contamination in A399, A401, and A1651.

Cluster	z	θ_o ($'$)	β	n_{eo} $10^{-3}\,h^{1/2}\,\mathrm{cm}^{-3}$	kT_e keV
A399	0.0715	4.33 ± 0.45	0.742 ± 0.042	3.23 ± 0.18	7.0 ± 0.2
A401	0.0748	2.26 ± 0.41	0.636 ± 0.047	7.90 ± 0.81	8.0 ± 0.2
A478	0.0900	1.00 ± 0.15	0.638 ± 0.014	27.81 ± 9.7	8.4 ± 0.7
A1651	0.0825	2.16 ± 0.36	0.712 ± 0.036	7.14 ± 3.2	6.1 ± 0.2
A1656	0.0232	9.32 ± 0.10	0.670 ± 0.003	4.52 ± 0.04	9.1 ± 0.4
A2142	0.0899	1.60 ± 0.12	0.635 ± 0.012	14.95 ± 1.0	9.7 ± 0.8
A2256	0.0601	5.49 ± 0.21	0.847 ± 0.024	4.08 ± 0.08	6.6 ± 0.2

Table 6.15: Summary of cluster model parameters used in the interpretation of our data. Quoted errors are approximate 68% errors about the best-fit model; for the actual confidence intervals which follow from our x-ray analysis, see Ch. 4 , § 4.4.

6.6 Interpretation

6.6.1 Baryonic Surface Densities

As pointed out by Myers et al. (1997), the SZE also yields a direct (i.e., Hubble-constant independent) measurement of the surface density of baryons in a cluster averaged over the telescope beam. This can be shown to be

$$\Sigma_G = 7.013 \times 10^{13} \left(\frac{1\,\mathrm{keV}}{T_e}\right) \times \left(\frac{y_{sw}}{10^{-5}\,\eta_G}\right)\ \mathrm{M}_\odot\,\mathrm{Mpc}^{-2}. \qquad (6.15)$$

Here η_G is the Gaussian efficiency as defined in Eq. 2.59. These are shown for both isothermal and hybrid cluster models in Table 6.16. Due to the fact that the hybrid models switch out less flux, lower surface densities are required to produce a fixed switched decrement, and the surface densities for the hybrid models are therefore $\sim 15\%$ lower than those for the isothermal models. All the clusters show similar surface densities, $\sim 7.0 \times 10^{13}\,\mathrm{M}_\odot\,\mathrm{Mpc}^{-2}$ for the isothermal models.

Cluster	Isothermal		Hybrid	
	η_G	Σ_G [A]	η_G	Σ_G [A]
A399	81.2%	4.55 ± 0.55	93.8%	3.94 ± 0.48
A401	76.4%	7.70 ± 0.56	—	—
A478	83.8%	7.74 ± 0.85	95.4%	6.80 ± 0.75
A1651	86.0%	6.50 ± 0.83	—	—
A1656	57.9%	8.49 ± 1.40	66.6%	7.38 ± 1.21
A2142	81.2%	8.08 ± 0.80	94.6%	6.93 ± 0.69
A2256	84.6%	6.28 ± 0.78	94.5%	5.62 ± 0.70
(Average)	—	7.0 ± 1.6	—	6.1 ± 1.4

[A] In units of $10^{13}\,\mathrm{M}_\odot\,\mathrm{Mpc}^{-2}$.

Table 6.16: Baryonic surface mass densities for isothermal and hybrid cluster models.

6.6.2 H_0

In this section, we present a measurement of the Hubble constant based on the SZE observations discussed in § 6.4 and § 6.5 and the x-ray models of Chapter 4. Before discussing our actual results, we present a schematic derivation of H_0 to motivate and clarify what follows.

The idea is as follows. The x-ray flux F_X observed at a distance $D_L(z)$ from a cluster is

$$F_X \propto \frac{1}{D_L^2(z)} \int d^3V n_e n_p \tag{6.16}$$

where $D_L(z)$ is the luminosity distance to the cluster, n_e and n_p are the electron and proton number densities in the intra-cluster medium (ICM), and the integral is over the volume of the ICM. If the distribution of ICM electrons (and protons) follows the spherically symmetric β model,

$$n_e(R) = n_{eo}(1 + R^2/R_0^2)^{-3\beta/2} \tag{6.17}$$

where n_{eo} is the central electron density, R is the spherical metric radius from the cluster center, and R_0 is a characteristic scale. Consider that we have $\theta_0 = R_0/D_A(z)$ (where $D_A(z)$ is the angular distance diameter) and β in hand from x-ray images of the cluster. Then if F_X is measured, we obtain

$$n_{eo} \propto \sqrt{\frac{D_L^2(z)}{D_A^3(z) \int \zeta^2 \, d\zeta \, (1 + \zeta^2/\theta_0^2)^{-3\beta}} F_X}. \tag{6.18}$$

The integral here is a dimensionless form factor which we have expressed in terms of $\zeta = R/D_A(z)$. Counting up the distances , we see that the x-ray observations determine n_{eo} up to a factor of $h^{1/2}$. At low frequencies ($\nu \lesssim 20$ GHz), the decrement at the cluster center due to the SZE is given by

$$\Delta T = -2\, T_{CMB} \times \frac{kT_e}{m_e c^2} \times \sigma_T \int dz \, n_e(z). \tag{6.19}$$

Here σ_T is the Thompson-scattering cross-section, and the integral is along the line of site. Employing the density model inferred from x-ray observations

$$n_e(z) = n_{eo}\, h^{1/2}\, (1 + z^2/R_0^2)^{-3\beta/2} \tag{6.20}$$

and changing variables to $\xi = z/D_A(z)$, the observed SZE decrement will be:

$$\Delta T_{obs} = -2\, T_{CMB} \times \frac{kT_e}{m_e c^2}\, h^{1/2}\, n_{eo}\, D_A(z) \int d\xi (1 + \xi^2/\theta_0^2)^{-3\beta/2}). \tag{6.21}$$

Absorbing everything on the right-hand side but h into what we will call ΔT_{pred} — which is just the SZE decrement which would be observed if $h = 1$ — we find

$$h = \left(\frac{\Delta T_{pred}}{\Delta T_{obs}} \right)^2 . \tag{6.22}$$

The heart of the matter is in Eq. 6.21. Consider the more general case that the observable ΔT_{obs} is given by

$$\Delta T_{obs} = \alpha \int dz\, f(z/R_0) \tag{6.23}$$

where α is a constant which can be fixed independently and may contain powers of h, and f is a function which can be determined independently but is assumed to be dimensionless (for the case at hand α is fixed from x-ray observations and contains a power $h^{1/2}$). Then using the same change of variables we have

$$\Delta T_{obs} = \alpha\, D_A(z) \int d\xi\, f(\xi/\theta_0). \tag{6.24}$$

Thus the distance enters the problem in two places, and only in the degenerate case $\alpha \propto h$ does it vanish. Except in that case, the h dependence of α just determines how the final solution for h will depend on the ratio $\Delta T_{pred}/\Delta T_{obs}$. It is therefore not quite correct to think of the SZE as an angular distance measure; it actually measures some combination of angular and luminosity distances (although since these only differ by factors of $(1+z)$ in any cosmology, this may be a semantic distinction).

For the realistic case, the telescope switching pattern must be taken into account. In terms of the y parameter now, the observed decrement will be

$$y_{pred} = \frac{1}{\Omega_{Beam}} \int d\Omega\, y(\hat{\Omega})\, R_{N,sw}(\hat{\Omega}); \tag{6.25}$$

$y(\hat{\Omega})$ itself is computed from the density models of Chapter 4 and an assumed temperature profile. Then we have

$$h = \left(\frac{y_{pred}}{y_{obs}} \right)^2 . \tag{6.26}$$

y_{pred} was calculated using an integration code was written in `C`, and checked against two independent integration codes (one of which being the code used by Myers et al. (1997)) and an analytic test case with results agreeing to better than 1%. The new code offers the possibility, not available in the previous code, of allowing for hybrid isothermal/adiabatic models with arbitrary isothermal radii and adiabatic indices. For more details on the form of the integral we have used, see Myers et al. (1997).

We explore two classes of models in this analysis: isothermal and hybrid isothermal/adiabatic models (see § 2.2). For the hybrid models, we take $R_{iso} = 500\,h^{-1}\,\mathrm{kpc}$ and $\gamma = 1.5$. The model predictions and observations (§ 6.4 and § 6.5) for all 7 clusters (A399, A401, A478, A1651, Coma, A2142, and A2256) are shown in Table 6.6.2 along with the Hubble constants they imply. Due to the statistically significant LEAD–TRAIL difference observed in A1651 and A401, we do not include these results in our final sample until further confirmation is available. The y_{pred} values for the isothermal models in Table 6.6.2 are computed from the *mean* of the τ_{sw} distribution from our Monte Carlo cluster analysis (Table 4.10). The uncertainties are computed by adding in quadrature the 1σ temperature error bar (symmetrized if necessary) with the uncertainty in the optical depth determined by the Monte Carlo fits. The hybrid predictions are calculated from the best fit models, and assumed to have the same uncertainties as the isothermal predictions.[5] Using the Leitch (1998) measurement of the RMS of intrinsic CMB fluctuations on these scales ($\sim 78 \pm 11\,\mu\mathrm{K}$), we estimate that CMB anisotropies contribute an uncertainty of $\delta y \sim 0.25 \times 10^{-5}$ given a typical scan pattern. This is included in the $h^{1/2}$ error bar.

The values of H_0 implied by our models are significantly higher than those which resulted from the models adopted by Myers et al.: the isothermal models for the best 5 clusters give $H_0 = 70 \pm 5\ \mathrm{km\,s^{-1}\,Mpc^{-1}}$. The results are not highly sensitive to the choice of isothermal versus hybrid temperature models; for both our final sample and the 7 clusters as a whole, the hybrid models reduce H_0 by 2 $\mathrm{km\,s^{-1}\,Mpc^{-1}}$ relative to the isothermal models. For all but the Coma cluster, we adopt the isothermal model; following Herbig et al. (1995), we use the hybrid isothermal/adiabatic model (Hughes et al. 1988a,b) with the previously stated parameters. This results in the measurement presented in Table 6.18: $H_0 = 71 \pm 5\ \mathrm{km\,s^{-1}\,Mpc^{-1}}$ (internal scatter only). Including the systematic radio and x-ray calibration errors, we have $H_0 = (71 \pm 5)^{+5}_{-4} \pm 6\ \mathrm{km\,s^{-1}\,Mpc^{-1}}$, or $H_0 = 71(\pm 5)_{\mathrm{random}}(\pm 8)_{\mathrm{calib.}}$ $\mathrm{km\,s^{-1}\,Mpc^{-1}}$ overall.

[5] Although this is not entirely realistic, it will only turn out to matter for Coma. For this cluster, the dominant uncertainty is Ω_{Beam}.

The increase in H_0 over the results in Myers et al. is largely due to the fact that the optical depth for Compton scattering is higher in our analysis than in the previous models. In addition, A399 yields a Hubble constant on the high end of the distribution. Table 6.19 shows how the current models have changed relative to the models employed by Myers et al. (1997). In evaluating the significance of this, the estimated $\sim 15\%$ modeling errors estimated by these authors should be kept in mind. Our adoption of the Markevitch et al. (1998) ASCA temperatures also raises H_0 slightly over the value which would be obtained using the (GINGA and EXOSAT) temperatures of Myers et al. If we adopt these old temperatures (except for A399, for which we keep the ASCA temperature) the 5 cluster sample yields $H_0 = 67 \pm 10$ km s^{-1} Mpc^{-1}. The most notable change is in A478, for which the ASCA temperature implies an H_0 a full 56% higher than that implied by the temperature (6.6 keV) used by Myers et al. Since many of the GINGA and EXOSAT data are fit to single-component plasmas with no account for cooling flow emission, and in a cooling flow cluster well over half of the cluster luminosity can come from within the cooling radius, it is likely that cooling flow emission is the origin of the bias. It is worthy of note that using the ASCA-based temperatures halves the scatter in the derived H_0 values.

The increase of τ_{sw} bears further comment. This change is not surprising for A2142, which had the oldest least reliable density model (based on the Einstein analyses of Abramopoulos & Ku 1983). In contrast, the Coma, A478, and A2142 predictions for τ_{sw} were all based on recent analyses of ROSAT data and appeared to be fairly reasonable. The discrepancy could be due to the fact that in most cases, the central densities in the literature are derived using the central regions of the x-ray image; this method is more subject to Poisson noise and β model parameter degeneracies than our approach (as noted in § 2.1). By way of comparison we calculated τ_{sw} using the Mohr et al. (1999) models of A2256 and Coma, obtaining values that agree with ours to better than 2% in both cases. Mohr et al. use an approach similar to our own for estimating the central densities (at least for the clusters which are well-fit by a single β model).

The distribution of H_0 values for the individual clusters shows no evidence for scatter beyond that expected from the observational and modeling uncertainties. Figure 6.8 shows the $h^{1/2}$ values and errors for A399, A478, A1656, A2142, and A2256, along with a least-squares fit to a constant. The best fit has $\chi^2 = 1.38$ for $\nu = 4$, which implies $\chi^2_\nu = 0.34$. This is consistent with a constant value for $h^{1/2}$, and appears to suggest that our error bars have been slightly overestimated. Since for $\nu = 4$ there is approximately a 15% chance of observing χ^2_ν values this small or smaller for Gaussian-distributed data, this is not highly significant. The standard deviation of the individual $h^{1/2}$ measurements about the best fit is 0.068. Our analysis indicates that projection effects and other random errors that we may not have accounted for are not important at the level of accuracy we have achieved, and that in order to distinguish these effects from other sources of noise more precise models and observations are necessary.

The significance of these results will be discussed further in Chapter 7.

Cluster	$y_{obs}/10^{-5}$	ISOTHERMAL			HYBRID		
		$y_{pred}/10^{-5}$	$h^{1/2}$	H_0	$y_{pred}/10^{-5}$	$h^{1/2}$	H_0
A399	3.70 ± 0.42	3.42 ± 0.22	0.924 ± 0.135	85^{+27}_{-23}	3.36 ± 0.21	0.908 ± 0.125	82^{+25}_{-23}
(A401)	6.93 ± 0.46	4.95 ± 0.32	0.714 ± 0.071	51^{+10}_{-9}	4.89 ± 0.31	0.706 ± 0.070	50^{+10}_{-9}
A478	7.77 ± 0.58	6.05 ± 0.54	0.779 ± 0.093	61^{+15}_{-14}	5.85 ± 0.52	0.753 ± 0.090	57^{+14}_{-13}
(A1651)	4.88 ± 0.59	2.92 ± 0.17	0.598 ± 0.086	36^{+10}_{-9}	2.83 ± 0.172	0.580 ± 0.084	34^{+9}_{-8}
A1656	6.38 ± 1.01	4.91 ± 0.37	0.770 ± 0.132	59^{+23}_{-20}	5.00 ± 0.38	0.784 ± 0.14	61^{+23}_{-21}
A2142	9.10 ± 0.52	8.12 ± 0.74	0.892 ± 0.100	80^{+18}_{-17}	7.84 ± 0.72	0.862 ± 0.096	74^{+17}_{-16}
A2256	5.00 ± 0.60	4.11 ± 0.26	0.822 ± 0.118	68^{+21}_{-18}	4.09 ± 0.26	0.818 ± 0.118	$67^{+16.7}_{-14.6}$
(All clust.)			0.786 ± 0.041	62 ± 7		0.773 ± 0.041	60^{+7}_{-6}
SAMPLE			0.837 ± 0.031	70 ± 5		0.825 ± 0.024	68 ± 5

Table 6.17: Observed Compton y's for 7 clusters, along with predicted y's for both isothermal and hybrid cluster atmosphere models. Clusters in parentheses have been excluded from the sample average.

Cluster	$y_{obs}/10^{-5}$	$y_{pred}/10^{-5}$	$h^{1/2}$	H_0
A399	3.70 ± 0.42	3.42 ± 0.22	0.924 ± 0.135	85^{+27}_{-23}
A478	7.77 ± 0.58	6.05 ± 0.54	0.779 ± 0.094	61^{+15}_{-14}
A1656	6.38 ± 1.01	5.00 ± 0.38	0.784 ± 0.141	61^{+23}_{-21}
A2142	9.10 ± 0.52	8.12 ± 0.74	0.893 ± 0.099	80^{+19}_{-17}
A2256	5.00 ± 0.60	4.11 ± 0.26	0.822 ± 0.118	68^{+21}_{-19}
SAMPLE	—	—	0.841 ± 0.029	$\mathbf{71 \pm 5}$

Table 6.18: Summary of H_0 results on the 5 clusters in our final sample, using the best available models.

Cluster	T_e	τ_{sw}
A478	+28%	+13%
A1656	±0%	+6%
A2142	+5%	+12%
A2256	−12%	+12%

Table 6.19: Change in cluster model parameters between Myers et al. (1997) and this work.

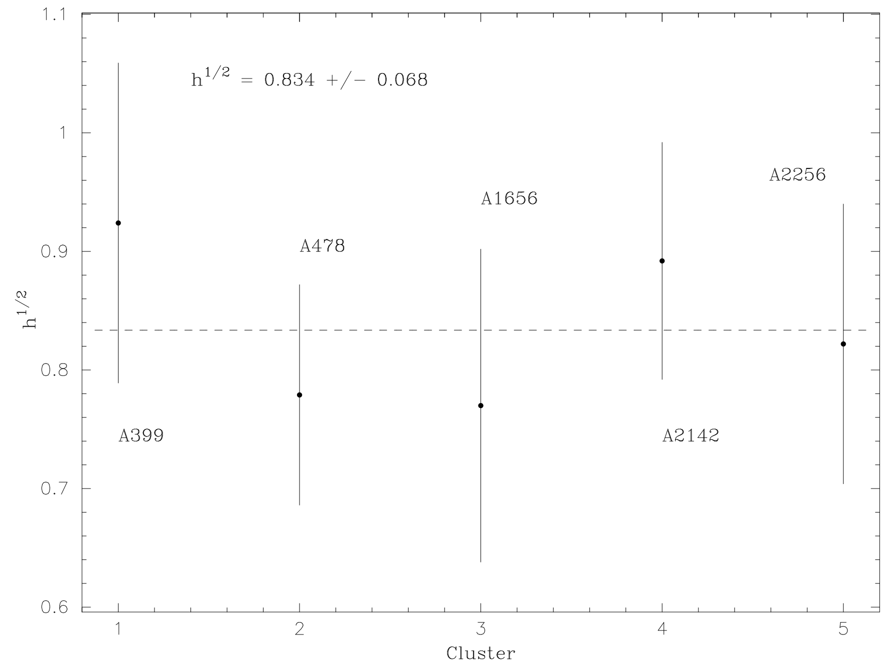

Figure 6.8: Observed values of $h^{1/2}$ for the 5 clusters in our final sample. The straight line indicates the least-squares fit of a constant to the data, which has $\chi^2_\nu = 0.34$ for $\nu = 4$.

Chapter 7

Conclusions

The primary goal of this thesis was to derive an improved measurement of the Hubble constant from SZE observations, x-ray models, and an improved radio calibration. We were most successful in this respect, obtaining a value of $H_0 = 71 \pm 5\,^{+5}_{-4} \pm 6\ \mathrm{km\,s^{-1}\,Mpc^{-1}}$, or $H_0 = 71(\pm 5)_{rand.}(\pm 8)_{calib.}\ \mathrm{km\,s^{-1}\,Mpc^{-1}}$. This is the most accurate measurement of H_0 from the SZE to date, and the only one based on an unbiased cluster sample. Our result is in agreement with recent Cepheid-based determinations of the Hubble constant (Madore et al. 1999) which yield $72 \pm 5 \pm 7\ \mathrm{km\,s^{-1}\,Mpc^{-1}}$. Myers et al. (1997) obtained (ignoring calibration uncertainties) $H_0 = 54^{+12}_{-11}\ \mathrm{km\,s^{-1}\,Mpc^{-1}}$, relative to which the current work represents an improvement of greater than a factor of two in precision. In addition, the calibration uncertainty in our experiment has been reduced by a factor of two due to the measurements presented in Chapter 5, which yield $S_{cas,1994} = 194^{+5}_{-6}$ Jy. The direct calibration of our recent SZE observations off of Cas A renders our results independent of any uncertainties due to the measurement of intermediate flux ratios— an opportunity which will be difficult to replicate with the instruments likely to dominate SZE work in the near future (all of which are either in the southern hemisphere, or possess beams too small to effectively calibrate off of Cas A).

The most important improvement in the present H_0 measurement from the OVRO sample is the development of high-quality ICM models based on the most recent ROSAT and ASCA data. Our Monte-Carlo analysis of Chapter 4 quantifies for the first time the real uncertainties in our SZE predictions due to the density profile determination and shows them to be relatively small compared to other limiting factors (such as the x-ray absolute flux calibration!). This is primarily due to the fact that the ROSAT data directly constrain the cluster density profiles. While for any given cluster there may be a fairly large class of admissible β models, they all must therefore amount to operationally similar descriptions of the ICM itself. The adoption of the ASCA-measured ICM temperatures significantly increases the precision of our results. Our ROSAT-based density models are in excellent agreement with the independent analysis of Mohr et al. (1999), with the mean baryonic mass ratio between the two analyses for 20 clusters in them both agreeing to better than 1%. The precision of our analysis (and that of Mohr et al.) stems in part from the fact that we use the total x-ray flux in the cluster to determine the electron density instead of the central surface brightness. This method is less subject to Poisson noise and the well-known parameter degeneracies which arise in β model fitting.

In addition, our analysis of 22 x-ray clusters yields cosmologically interesting information on its own. The mean ICM mass fraction we derive, $f_{ICM} = (7.02 \pm 0.28)\, h^{-3/2} \times 10^{-2}$ (at R_{500}), can be combined with Big Bang Nucleosynthesis constraints to yield a measurement of the total matter content of the universe. Using $\Omega_B h^2 = 0.019 \pm 0.001$ (Burles & Tytler 1998) together with our measured gas mass fraction ($= \Omega_B/\Omega_M$ under the "fair sample" hypothesis) , we find $\Omega_M = 0.26\, h^{-1/2}$. With our result $h = 0.71 \pm 0.09$ (including calibration uncertainties), we have[1] $\Omega_M = 0.30 \pm 0.06$. This is consistent with large-scale structure estimates of Ω_M, as well as those derived from cluster evolution (Bahcall et al. 1999). Even the most contrived models for the dynamical state of the ICM would have a difficult time producing the extra factor of 3 required to attain the canonical $\Omega_M = 1$ universe. Recent observations of intrinsic CMB anisotropy on arcminute to degree scales (Netterfield et al. 1997; Leitch 1998; Miller et al. 1999) suggest the existence of an acoustic peak at $l \sim 200$, implying $\Omega_M + \Omega_\Lambda \sim 1$; these lines of evidence may collectively indicate the existence of a non-zero cosmological constant or other energy density component such as quintessence (Wang et al. 1999). This would be consistent with the recent results of Perlmutter et al. (1999) who, using SN Ia's as standard candles, map out a luminosity distance which is inconsistent with a flat $\Omega_\Lambda = 0$ cosmology at 99% confidence (including identified systematics in their data). Constraining $\Omega_M + \Omega_\Lambda = 1$, these

[1]Although this may be regarded as an upper limit due to the possible of the presence of baryons which do not show up in x-rays, in practice it is likely that there uncertainties associated with the total mass at at least this level and so we treat it as an equality with the caveat that a $\sim 20\%$ uncertainty might reasonably be associated with the result due to the total mass uncertainties.

authors find $\Omega_M = 0.28^{+0.09}_{-0.08}{}^{+0.05}_{-0.04}$ (1 σ statistical and systematic errors, respectively) consistent with the value $\Omega_M = 0.30 \pm 0.06$ which results from our x-ray cluster analysis plus H_0 from the SZE. Note that the concordance of these results comes on the basis of independent observational *and* theoretical grounds: the SN Ia value results from assuming a flat cosmology plus the observed $D_L(z)$, whereas the x-ray cluster value of Ω_M results from the HSE gas mass fraction measurements plus Big Bang Nucleosynthesis. All of these assumptions will be stringently tested by CMB observations (both from the ground and from orbit), x-ray observatories, and larger SN Ia samples which will allow tests of systematics such as dimming by photometrically colorless dust.

The value of H_0 which results from our SZE survey implies a Hubble time ($\equiv H_0^{-1}$) of $(13.8 \pm 1.2) \times 10^9$ years. While the scale for the age of the universe is set by H_0^{-1}, the exact value is cosmology dependent; we compute the constant of proportionality using the expressions of Kolb & Turner (1990). For a flat CDM cosmology ($\Omega_M = 1$, $\Omega_\Lambda = 0$) the age of the universe, t_0, is

$$t_0 = \frac{2}{3} H_0^{-1} \tag{7.1}$$

which would imply an age of $(9.2 \pm 0.8) \times 10^9$ years. For an open, $\Omega_M = 0.3$ universe we find $t_0 = 0.81 \times H_0^{-1}$, or $t_0 = (11.2 \pm 1) \times 10^9$ years with $h = 0.71 \pm 0.09$. For a flat universe with $\Omega_M = 0.3$ and $\Omega_\Lambda = 0.7$ we find $t_0 = 0.96 \times H_0^{-1}$ or $t_0 = (13.3 \pm 1.2) \times 10^9$ years with $h = 0.71 \pm 0.09$. These estimates can be compared with lower limits on the age of the universe determined by main-sequence fitting in star clusters. Two recent calculations give (Reid 1997; D'Antona et al. 1997) $t_0 = (12 \pm 1) \times 10^9$ years, and a third (Chaboyer et al. 1998) finds $t_0 = (11.5 \pm 1.3) \times 10^9$ years. These measurements are inconsistent or only marginally consistent with the age of a flat CDM universe given our H_0. Barring unusually long globular cluster formation times ($\gtrsim 2 \times 10^9$ years), the globular cluster limits on the age of the universe are consistent with both open, matter-dominated and flat lambda (or quintessence) cosmologies. If the globular cluster formation times were to be long, the lambda cosmology (or H_0 values on the low end of the range allowed by our measurements) would be favored.

Our results also serve as something of a cautionary tale, the lesson being: the potential (in this case, model-based) systematic errors associated with any given result must be borne in mind when evaluating said result. It is clear that the density models and temperature models employed by Myers et al. were indeed in error at the estimated level ($\sim$ 15%). It should then come as no surprise that the result we get (with significantly better models in hand) comes in $\sim$ 30% higher than the Myers et al. result. The excellent agreement between our ICM masses and those obtained in a completely independent analysis argues that the density models are well understood, and that further improvements are likely to come from other directions. In particular, the large differences between the ASCA temperatures and those from previous experiments were somewhat unexpected, and suggest that detailed study of the x-ray spectra and possible systematics (due, e.g., to multi-phase or cooling flow emission) might prove beneficial. Furthermore, convincing spatially resolved spectra of the ICM have yet to be obtained, and this could be a source of bias in our predictions at the $\sim$ 15% level. Substructure in the ICM is another possible source of bias at the same level. While there is as yet no direct observational evidence for these effects, neither is there unambiguous evidence against them.

In spite of the possibility of model uncertainties at this level, there is good reason to be optimistic. The advantage of the SZE as a distance measure does not stem from the fact that there are no associated systematic uncertainties (no experiment can claim this). Instead, it is due to the fact that the method is based on relatively simple astrophysics, about which current and near future experiments will tell us a great deal. With this information (and a lot of hard work!) it will be possible to directly address these potential systematics. The CBI will lead in this field by measuring the SZE with greater sensitivity than possible on the OVRO 5.5-meter , and extending the coverage of the sample discussed in Chapter 3. It is not unreasonable to expect a determination of H_0 to an accuracy of between 8 and 10 % from this program, including systematics and model uncertainties. In the long term it is clear that SZE-based measurements of H_0 with accuracies much better than this will be difficult. If nothing else, absolute calibration of both radio and x-ray telescopes is likely to be a limiting factor. For example if the radio and x-ray data were each calibrated to 2%, a 6% systematic error would be implied in the Hubble constant. In light of this we may expect work in the more distant future to emphasize the redshift-independent nature of the SZ signal (e.g., high-redshift cluster searches or q_0 measurements) and the kinematic effect for peculiar velocity measurements (which are less affected by calibration uncertainties) . In any case there is much to be done, and we can expect developments to continue apace for some time to come.

Appendix A

Cluster Images and Profiles

Appendix B

XSPEC Analysis Results

In this appendix we tabulate the principal results of our `XSPEC` model-fitting. For the primary exposure of each cluster, we list k for the best-fitting Raymond-Smith model, along with the reduced χ^2 of the fit. The codes in parentheses after the exposure indicate whether Galactic (G) absorption was assumed, or the ROSAT (R) data was used to fit for the hydrogen column density; and whether the central $150\,h^{-1}$ kpc was included in the spectrum (1) or not (0). The "anomalously" low values of χ^2_ν for some of the data are due primarily to the fact that the number of degrees of freedom is small ($1 \leq \nu \leq 4$). Where a second cool component was included in the fit, we indicate the resulting normalization in the comments (as k_2). We only included cool components when they gave a significant reduction in χ^2_ν; however, the amplitudes were not always significantly constrained. The temperatures of all such components were fixed at $T_{e2} = 1.0$ keV. The analyses used for our density models are bolded; other analyses are included for comparison. The comments also indicate what energy channels were used in the analysis; unless otherwise specified, the channels used were R4, R5, R6, and R7 ($0.5-2.0$ keV).

Exposure	$k/10^{-2}$	χ^2_ν	ν	Comments
A85BM(0G)	4.73 ± 0.06	4.37	3	
A85BM(1G)	8.56 ± 0.30	2.85	2	$k_2/10^{-2} = 0.84 \pm 0.21$
A399BM(1G)	3.71 ± 0.06	2.20	3	
A401BM(1G)	6.02 ± 0.23	2.67	2	$k_2/10^{-2} = 0.63 \pm 0.18$
A401BM(1G)	6.93 ± 0.08	7.80	3	no soft component.
A478A(0G)	2.75 ± 0.04	17.7	3	
A478A(0R)	3.27 ± 0.09	1.91	2	nH $= (21.1 \pm 1.0) \times 10^{20}$ cm^{-2}
A478A(1G)	6.58 ± 0.22	66.2	2	$k_2/10^{-2} = 0.00 \pm 0.26$
A478A(1R)	7.87 ± 0.26	2.40	1	nH $= (25.0 \pm 1.6) \times 10^{20}$ cm^{-2} $k_2/10^{-2} = 0.65 \pm 0.43$
A478A(1R)	8.23 ± 0.18	3.20	2	nH $= (22.5 \pm 0.7) \times 10^{20}$ cm^{-2} no soft component
A754BM(1G)	9.89 ± 0.10	0.7	4	$R1, R4+$; identical result as $R4+$
A780A(0G)	1.89 ± 0.03	2.98	3	
A780A(1G)	5.69 ± 0.06	12.8	3	
A1651A(0G)	1.71 ± 0.04	0.24	3	
A1651A(1G)	3.25 ± 0.06	0.7	3	
A1656BM(1G)	44.6 ± 0.3	6.2	3	
A1795BHM(0G)	3.03 ± 0.03	3.6	3	
A1795BHM(1G)	6.85 ± 0.20	2.81	3	$R2, R4+$; $k_2/10^{-2} = 0.72 \pm 0.15$
A2029BM(0G)	3.71 ± 0.05	0.85	2	
A2029BM(1G)	8.18 ± 0.28	0.17	2	$k_2/10^{-2} = 0.66 \pm 0.21$
A2142BM(0G)	5.22 ± 0.05	1.0	3	
A2142BM(1G)	8.68 ± 0.08	1.4	3	
A2244A(1G)	2.66 ± 0.07	2.95	3	
A2255A(1G)	2.65 ± 0.04	3.84	3	
A2256BM(1G)	7.15 ± 0.07	2.5	3	
A2597A(0G)	0.663 ± 0.027	1.76	3	
A3112A(0G)	1.46 ± 0.03	1.52	3	
A3112A(1G)	3.45 ± 0.20	0.19	2	$k_2/10^{-2} = 0.37 \pm 0.19$
A3158A(1G)	4.62 ± 0.09	0.42	5	
A3266A(1G)	7.12 ± 0.08	0.52	3	
A3558A(1G)	7.47 ± 0.25	4.68	2	$k_2/10^{-2} = 0.81 \pm 0.18$
A3571A(0G)	9.14 ± 0.13	0.5	3	
A3571A(1G)	15.15 ± 0.18	0.05	3	
A3667A(1G)	10.47 ± 0.11	3.34	3	
A3921C(0G)	1.62 ± 0.03	3.1	3	
A3921C(1G)	1.86 ± 0.10	0.87	2	$k_2/10^{-2} = 0.22 \pm 0.11$
A3921C(1G)	2.18 ± 0.04	3.99	3	no soft component

Appendix C

Integrals of the Isothermal Beta Model

For reference, a number of useful integrals involving the isothermal beta-model are recorded here. For the sake of clarifying the mathematics, we express everything in terms of electronic mass integrals (for the Sunyaev-Zeldovich integrals) or emission integrals (for the x-ray integrals); most observables of physical interest are simply and intuitively related to these model-dependent quantities. All of the results quoted here are valid for $0.5 < \beta < 1.0$. Except for the bremsstrahlung emission integrals, which for non-isothermal models then involve a spatial average of the Gaunt factor, all of these results are easily generalized to the case of pure adiabatic models. While comparably simple results are not obtainable for the most physically motivated models (hybrid isothermal/adiabatic ones), these expressions are useful for simple estimation, or for calculation inside the isothermal radius (typically about $0.5\,h^{-1}$ Mpc). Since the x-rays tend to give a strongly core-weighted picture of clusters, the x-ray formulae given here should be valid for most hybrid models (especially for application to ROSAT PSPC data).

As explained in § 2.2, the isothermal beta-model assumes that the electrons in the ICM are isothermal and have a spatial density like

$$n_e(r) = n_{eo}\left[1 + (\frac{r}{r_0})^2\right]^{-3\beta/2}. \qquad \text{(C.1)}$$

Integrating this density (at projected radius ρ) along the line of sight yields the electron mass surface-density on the sky:

$$\Sigma_e(\rho) = n_{eo} r_0 \sqrt{\pi}\, \frac{\Gamma(3\beta/2 - 1/2)}{\Gamma(3\beta/2)} \times \left[1 + (\frac{\rho}{r_0})^2\right]^{-3\beta/2+1/2}, \tag{C.2}$$

where we have used the relation

$$\int_{-\infty}^{+\infty} dx\, (1 + x^2 + y^2)^{-B} = \sqrt{\pi}\, \frac{\Gamma(B - 1/2)}{\Gamma(B)} \times (1 + y^2)^{-B+1/2}. \tag{C.3}$$

Both the SZ-effect and the baryonic mass surface-density are proportional to Σ_e in the context of isothermal $\beta-$models. A single-dish radio telescope (with a Gaussian beam width σ) measures the beam-weighted average of the signal on the sky

$$\Delta T_{obs} = \int\int d\Omega \frac{1}{2\pi\sigma^2} e^{-\rho^2/2\sigma^2} \Delta T(\hat{\Omega}) \tag{C.4}$$

so it is convenient to define a beam averaged electron surface mass density $\overline{\Sigma_e}$,

$$\overline{\Sigma_e} = \int\int d\Omega \frac{1}{2\pi\sigma^2} e^{-\rho^2/2\sigma^2} \Sigma_e(\rho) \tag{C.5}$$

For for the Σ_e given by equation Eq. C.2 this expression can be reduced to the nominally analytic although ungainly form

$$\overline{\Sigma_e} = n_{e0} r_0 \frac{\sqrt{\pi}}{\Gamma(3\beta/2)} \left(\frac{r_0^2}{2\sigma^2}\right)^{3\beta/2-1/2} e^{r_0^2/2\sigma^2} \mathrm{Csc}\left(\frac{\pi}{2}(3\beta - 1)\right) \times \tag{C.6}$$

$$\left[\pi + \frac{3}{2}(1-\beta)\Gamma\left(\frac{3}{2}(\beta-1)\right)\Gamma\left(\frac{3}{2}(\beta-1), 0, \frac{r_0^2}{2\sigma^2}\right)\mathrm{Sin}\left(\frac{\pi}{2}(3\beta-1)\right)\right].$$

Here $\Gamma(a, x, y)$ is the generalized incomplete Gamma function ($\Gamma(a, x, y) = \Gamma(a, x) - \Gamma(a, y)$). $\overline{\Sigma_e}$ is well defined for $\beta > \frac{1}{3}$.

The total electronic mass enclosed within a sphere of radius R may be obtained for a general isothermal $\beta-$ model in terms of a Hypergeometric function. We find

$$M_e(< R) = \frac{4}{3}\pi r_0^3 n_{eo} \left(\frac{R}{r_0}\right)^3 {}_2F_1\left(\frac{3}{2}, \frac{3\beta}{2}, \frac{5}{2}, -(\frac{R}{r_0})^2\right). \tag{C.7}$$

The total baryonic mass within the sphere is proportional to this quantity. For the special case $\beta = 2/3$ we may evaluate Eq. C.7 in terms of elementary functions; we obtain:

$$M_e(< R) = 4\pi r_0^3 n_{e0} \times (\frac{R}{r_0} - \mathrm{ArcTan}(\frac{R}{r_0})) \tag{C.8}$$

It is clear that this does not converge as $R \to \infty$, indicating that at some large scale the model is inappropriate as a description of the cluster medium. The equivalent of $M_e(< R)$ in *cylindrical* projection is of greater interest in interpreting the SZE observations. Integrating the azimuthally symmetric function $\Sigma_e(\rho)$ given by Eq. C.2, we find that the total electronic mass contained within a projected radius ρ is

$$M_e(< \rho) = \sqrt{\pi}\,\frac{\Gamma(3\beta/2-1/2)}{\Gamma(3\beta/2)} n_{e0} r_0^3 \times \frac{2\pi}{3(1-\beta)} \times \left((1+(\frac{\rho}{r_0})^2)^{\frac{3}{2}(1-\beta)} - 1\right) \tag{C.9}$$

A convenient measure of the thermal bremsstrahlung radiation is the *emission integral* EI:

$$EI = \int d^3V n_e n_h. \tag{C.10}$$

Henceforth we assume $n_e = n_h$ everywhere. For an isothermal beta model, the contribution of regions at radii $< R$ to EI is (by analogy with Eq. C.7)

$$EI(< R) = \frac{4}{3}\pi r_0^3 n_{e0}^2 \left(\frac{R}{r_0}\right)^3 {}_2F_1\left(\frac{3}{2}, 3\beta, \frac{5}{2}, -(\frac{R}{r_0})^2\right). \tag{C.11}$$

As $R \to \infty$ EI goes to

$$EI = \pi^{\frac{3}{2}} r_0^3 n_{e0}^2 \frac{\Gamma(3\beta - 3/2)}{\Gamma(3\beta)}. \tag{C.12}$$

For $\beta = 2/3$, these have the simple forms

$$EI(< R) = 2\pi r_0^3 n_{e0}^2 \left[\mathrm{ArcTan}\left(\frac{R}{r_0}\right) - \frac{R/r_0}{1+(R/r_0)^2}\right] \tag{C.13}$$

and

$$EI = \pi r_0^3 n_{e0}^2. \tag{C.14}$$

We may define a 1-dimensional analog to the emission integral which is proportional to the x-ray surface brightness:

$$X(\rho) = \int n_e^2(r) dz \tag{C.15}$$

where dz is a path-length element along the line of sight. Then we have, using Eq. C.3

$$X(\rho) = n_{e0}^2 r_0 \sqrt{\pi} \frac{\Gamma(3\beta - 1/2)}{\Gamma(3\beta)} \left(1 + (\frac{\rho}{r_0})^2\right)^{-3\beta+1/2}. \tag{C.16}$$

Then we find, in analogy with Eq. C.9, the contribution to EI from regions within projected radius ρ to be:

$$EI(<\rho) = n_{e0}^2 r_0^3 \sqrt{\pi}\frac{\Gamma(3\beta - 1/2)}{\Gamma(3\beta)} \times \frac{2\pi}{3(2\beta-1)}\left[1 - \left(1 + (\frac{\rho}{r_0})^2\right)^{\frac{3}{2}(1-2\beta)}\right]. \tag{C.17}$$

If we consider the value of EI with contributions between an inner radius ρ_1 and an outer radius ρ_2 we find

$$EI(\rho_1, \rho_2) = n_{e0}^2 r_0^3 \sqrt{\pi}\frac{\Gamma(3\beta - 1/2)}{\Gamma(3\beta)} \times \frac{2\pi}{3(2\beta-1)}\left[C(\rho_1) - C(\rho_2)\right] \tag{C.18}$$

where

$$C(q) = \left(1 + (\frac{q}{r_0})^2\right)^{\frac{3}{2}(1-2\beta)}. \tag{C.19}$$

All of these calculations are in terms of the physical radius at the cluster (i.e., cm, not radians), but ρ and r_0 can be trivially translated into angular units with the appropriate factors of D_A.

It is also useful to relate the x-ray surface-brightness to the total flux within a region bounded by two concentric circles of radii θ_1 and θ_2. For an isothermal β model, the x-ray surface brightness will be given by Eq. C.16 with the central surface brightness playing the role of the factor

$$I_x = n_{e0}^2 r_0 \sqrt{\pi}\frac{\Gamma(3\beta - 1/2)}{\Gamma(3\beta)}. \tag{C.20}$$

Comparison with Eq. C.18 shows that the total flux between these two radii is

$$F_x(\theta_1, \theta_2) = I_x \theta_0^2 \times \frac{2\pi}{3(2\beta-1)}\left[C'(\theta_1) - C'(\theta_2)\right] \tag{C.21}$$

with

$$C'(\theta) = \left(1 + (\frac{\theta}{\theta_0})^2\right)^{\frac{3}{2}(1-2\beta)}. \tag{C.22}$$

Appendix D

1.5-m Control Code Reference

List of Valid Commands
================================
acquisition
anwait
autowrap
average
bgdebug
buffer
cal
cancel
clearqueue
close
corrections
diode
disconnect
dumpsw
dumptot
exit
flux
hold
ibwrt
interlock
liaparam
local
log

mancal
nobuff
observe
offset
pmodel
poffset
point
position
powermeter
pparam
query
quit
radparam
readcat
readpow
record
relwait
remote
repaint
rlog
runqueue
schedule
schsub
service
setsource
showqueue
status
stow
testproc
timeproc
track
window
wrap

Command Parser
=================================

Commands are generally of the form

cmd

or

cmd (key—(key=value)+)

meaning that commands take either no arguments, a single key as argument, or one or more key/value pairs as arguments. All command, key, and value tokens are case insensitive. "cmd" strings are matched to the list of valid commands using a maximal string match; this "st" will not return a match, but "sto" will be identified as "stow" by the parser. The same matching principles apply to the set of key tokens associated with any individual command.

Note that there is no general mechanism for matching value tokens. In particular, string-valued value tokens must match one of the valid value tokens exactly (except for case).

Command Descriptions
==============================

acquisition - Set the tcp's acquisition threshold for establishing whether the command az/el is acquired or not acquired. An azimuth and elevation threshold in degrees are defined, as well an integer number of times that the telescope must be found within this distance of the command position for acquired status to be declared (permitting the continuation of radiometry procedures if "ANWAIT yes" has been declared). This number of times is ultimately interpreted in terms of a number of calls to some low level procedure; this procedure is called about once every 0.1-0.15 sec.

```
USAGE: acquisition (key=val)
  keys           vals
----       ------
az,el          threshold in degrees (0.03,0.06 typically)
threshold   an integer (5 is typically sufficient).
```

CLASS: foreground

APROPOS: anwait

anwait - "anwait" controls a state variable that determines whether or not the tcp will wait for the current predict position to be acquired before issuing radiometry commands.

USAGE: anwait (on—off)

CLASS: foreground

autowrap - "autowrap" controls a state variable that determines whether or not the tcp will automatically wrap to the other az sector when the predict position is within 3 degrees of a hard limit. It is generally preferable to set the wrap state manually using "wrap" since "autowrap" may engage the wrap during a radiometry procedure, which may cause confusion.

USAGE: autowrap (on—off)

CLASS: foreground

APROPOS: wrap

average - Sample average switched and total power from the receiver. The radiometry parameters asamp,ainteg, aidle, and areps are set by the command "radparameters". The control program performs asamp integrations of length ainteg x 0.1 sec, recording the resulting switched power measurement in a logfile entry as channel 36. A delay of aidle seconds is imposed between reps, which may be safely set to zero if desired. The usage of non-zero IDLEs are particularly useful for measurements of the CAL diode, as they allow a consistent "settling time" to be imposed. If total power information is available (use the command "powermeter" to inform the control program of tp info availability) then total power information will also be recorded in channel 33.

The standard deviation reported on a measurement is the error in the mean as computed from the scatter in the samples.

For an explanation of start and stop time logic, see the section on "Scheduler Logic".

USAGE: autowrap [start=xx:xx:xx] [stop=xx:xx:xx]

CLASS: foreground

APROPOS: radparameters.

WARNING: see the radparameters warning.

bgdebug - A debugging procedure.

CLASS: background

buffer - Sets the tcp to buffer foreground commands into the queue. This behavior will continue until a "nobuffer" command is issued. By default the commands in the queue are not executed; execution is intiated by issueing a "runqueue" command. Note that the buffering state and the queue-execution state of the tcp are independent.

For an explanation of the difference between foreground, background, and instant commands see the section on "Scheduler Logic".

USAGE: buffer

CLASS: background

APROPOS: nobuffer runqueue hold clearqueue showqueue

cal - Execute a CAL procedure. Radiometry parameters for this are controlled through the variables csamp,cinteg,cidle, and creps, accessed via "radparameters". This procedure works the same as the 5m/40m CAL procedures; note however the standard caveat for all radiometry procedures.

USAGE: cal [start=xx:xx:xx] [stop=xx:xx:xx]

CLASS: foreground

APROPOS: radparameters

WARNING: see "radparameters" warning.

cancel - Issuing a "cancel" command cancels the current procedure.

USAGE: cancel

CLASS: instant

WARNING: the tcp does not sample user input during (individual) radiometrci integrations; "cancel" may therefore take effect only after up to one integration period.

clearqueue - Clears the command queue.

USAGE: clearqueue

CLASS: instant

APROPOS: nobuffer buffer runqueue hold showqueue

IMPROVEMENT: currently clearqueue also sets the scheduler to non-buffering mode. Insure that changing this behavior will cause no problems and do so.

close - If there is a current remote connection, "close" causes the tcp to close this connection. It does not, however, cause the tcp to stop polling for new connections.

USAGE: close

CLASS: background

APROPOS: remote local disconnect

corrections - Set the pointing model coefficients. All coefficients, consistent with standard practice on the 5m/40m are in arcminutes.

USAGE: corrections (key=val)+ valid keys are az1-az8,za1-za4.

CLASS: foreground

APROPOS: pmodel

diode - "diode" allows the diode to be manually turned on and off.

USAGE: diode (on—off)

CLASS: foreground

APROPOS: mancal

disconnect - "disconnect" causes the tcp to close active remote connections. It is identical in its behavior to "close", but is a foreground procedure; thus it may be put into the queue and executed after a series of other commands.

USAGE: disconnect

CLASS: foreground

APROPOS: close

dumpsw - Perform a dump of 512 consecutive samples of switched power. The samples are obtained at approximately 0.1 second intervals. The dump format is typographically the same as the 5m/40m dump format; the first pair of columns, however, corresponds to switched power, and the second pair of columns corresponds to the elapsed time in milliseconds since the last sample was obtained. A similar format is used for switched power dumps. Dumps are recorded in c:\1m\logger. This is unlike the 5m/40m dumps wherein the first columns corresponds to average total power, and the second ones to the requested dump channels.

USAGE: dumpsw

CLASS: foreground

APROPOS: dumptot

dumptot - This procedure is the same as "dumpsw", except it obtains samples of total power from the powermeter.

USAGE: dumptot

CLASS: foreground

APROPOS: dumpsw

exit - shuts down the tcp. Not allowed if the tcp is in remote mode.

USAGE: exit

CLASS: foreground

flux - perform a FLUX procedure. Identical to standard OVRO 5/40 -m FLUX procedures. Access to the radiometry parameters fsamp, freps, fidle, and finteg is provided by the radparameters command.

USAGE: flux

CLASS: foreground

WARNING: c.f. radparameters.

foffset - Set the az/el foffsets. These are offsets, in degrees, which are *directly* added to the command angle. In particular, the fixed az offset (azfo) is an encoder-based and not a sky-based offset angle.

USAGE: foffset (key=offset) valid keys are azimuth,elevation. offset is a floating point number in *degrees* .

CLASS: foreground

APROPOS: poffset offset

hold - temporarily halt execution of the command queue. Execution is resumed upon the issuance of a "runqueue" command.

USAGE: hold

CLASS: instant

APROPOS: runqueue showqueue buffer nobuff

ibwrt - A low-level command which provides the ability to communicate directly to the GPIB card.

USAGE: ibwrt (string)

CLASS: foreground

interlock - A low-level command which provides the ability to set the az/el interlock status bytes directly.

USAGE: interlock (key=k)+ valid keys=(az—el) k=integer.

CLASS: foreground

liaparam - "liaparam" sets the operating parameters for the lock-in amplifier.

```
USAGE:liaparam (key=value)+

valid keys    valid values
----------------------------
sensitivity   100nV, 200nV, 500nV, 1uV,2uV,5uV,10uV,20uV
50uV,100uV,200uV,500uV,1mV,2mV,5mV,10mV,
20mV,50mV,100mV,200mV,500mV.

dynres       low,norm,high

pretime       1mS,3mS,10mS,30mS,100mS,300mS,1s,3s,10s,
30s,100s.
```

```
posttime      0s,0.1s,1s

expand       x1,x10

relative      on,off

offset        on,off
```

CLASS: foreground

APROPOS: ibwrite

local - "local" takes the tcp out of remote mode and stops polling for remote connections. Use with caution!!

USAGE: local

CLASS: instant

IMPROVEMENT: prohibit in remote mode. ensure <ESC> from kbd will perform this function.

log - Make an entry in the log file.

USAGE: log (string)

CLASS: foreground

mancal - "mancal" turns the cal diode on and off. It differs from "diode" only in that it is an instant command rather than a foreground command.

USAGE: mancal (on—off)

nobuff - "nobuff" takes the scheduler out of buffering mode. Subsequent commands are executed directly; commands which are in the queue remain there until executed sequentially. See the section on "Scheduler Logic" for a fuller explanation.

USAGE: nobuff

CLASS: instant

APROPOS: buffer runqueue showqueue hold

observe - "observe" searches for a planet or source in the ephemerides and if found, selects this source's position as the basis for az/el predict computations. "observe" does not actually command the telescope to follow the predicted position (see "track").

USAGE: observe (key=name) valid keys are src,source, and planet. Currently venus, jupiter, saturn, the moon, and the sun are valid "planets".

CLASS: foreground.

APROPOS: track readcat

offset - "offset" causes az/el offsets to be added to the predicted az/el positions. These offsets are measured in degrees, and are treated as being on the sky (i.e., the azo is divided by cos(el) before they are added to the command angle sent to the pedestal).

USAGE: offset (key=offset) valid keys are azimuth,elevation. offset is a floating point number in *degrees.*

CLASS: foreground

APROPOS: poffset foffset

pmodel - "pmodel" turns the pointing model on and off.

USAGE: pmodel (on—off)

CLASS: foreground

poffset - "poffset" allows the offsets derived from pointing procedures to be modified or zeroed. The az poffset is treated as being on the sky, i.e., it is divided by cos(el) before being added to the command angle.

USAGE: poffset (key=offset) valid keys are azimuth,elevation. offset is a floating point number in *degrees.*

point - "point" performs a pointing procedure consisting of one on-target AVERAGE procedure and four off-target AVERAGE procedures at +/- the pointing offset in az and el. The average data are first fit directly to a parabola in each direction and scans implying large offsets or opposite curvatures (in az/el) are rejected and flagged as FAILED points. Data which pass this test are fit to a gaussian plus constant switched power model using a standard nonlinear least-squared method. The preliminary parabolic fit greatly increases the stabliity of the solution (by rejecting unstable solutions!).

USAGE: point [start=xx:xx:xx] [stop=xx:xx:xx]

CLASS: foreground

APROPOS: poffset pparam

position - "position" commands the telescope to some az/el. As a side effect of this the telescope is put into track mode and the source is set to "ALTAZ".

If the telescope is requested to go within 3 degrees of the hard limit of the current sector and autowrap is on, the tcp will automatically drive the telescope to an intermediate position before requesting the user-requested position. This has the effect of putting the telescope in the other (safe) wrap. If autowrap is not enabled, the telescope will drive to the limit and disable tracking.

USAGE: position (key=position)+ valid keys are azimuth,elevation. position is a floating point number in degrees.

CLASS: foreground

APROPOS: autowrap wrap

powermeter - enables/disables the powermeter readout capability.

USAGE: powermeter (on—off)

CLASS: foreground

pparam - set the pointing paramters (beam FWHM, pointing offsets).

query - "query" reports the status of various parameters (chosen by the key token) to the user. Results are not output to the log file; the command analagous to this which causes logfile output is "record".

USAGE: query (key) valid keys are lia,radiometer.

CLASS: background

IMPROVEMENTS: add pparam.

quit - exits the control program. Not allowed in remote mode.

USAGE: quit

CLASS: instant

APROPOS: exit

radparam - "radparam" sets the radiometry parameters for the various radiometry procedures (flux,cal, and average).

```
USAGE: radparam (key=value)+
valid keys    valid values
----------------------------
fsamples,
csamples,     integer (number of integration periods)
asamples

freps,
creps,      integer
areps

finteg,
cinteg,      integer (x0.1 seconds)
ainteg       number of 0.1 sec samples in an
                                   integration period.

fidle,
cidle,        integer (xseconds)
aidle

foffset,      float (degrees)
feoffset
```

CLASS: foreground

APROPOS: flux,cal,average.

WARNING: The time it takes to read a single sample from both the lock-in and the powermeter sometimes exceeds 0.1 seconds. Warning messages are generated when this occurs. The noise statistics of the measurement, however, will not be affected by this. Problems would arise if the lock-in were sampled *more* rapidly than the integration time intrinsic to the lock-in, but this is never the case.

readcat - reads a source catalog off of c: (flute).

USAGE: readcat

CLASS: foreground

readpow - a low-level procedure reporting the output of the powermeter.

USAGE: readpow

CLASS: foreground

APROPOS: powermeter

record - Record the time or the state of the lock-in-amplifier or radiometry parameters in the logfile.

USAGE: record key valid keys are lia, radiometer, offsets, time, corrections.

CLASS: foreground

IMPROVEMENT: add pparam.

relwait - Waits a specified number of seconds.

USAGE: relwait (integer)

CLASS: foreground

remote - Put the tcp in remote controlled state. Currently executing commands continue to execute. Remote connections are watched for and accepted.

USAGE: remote

CLASS: background

repaint - Redisplay the screen on FLUTE.

USAGE: remote

CLASS: instant

rlog - Initiate remote transmission of logfile entries.

USAGE: rlog

CLASS: instant

runqueue - Initiate execution of buffered commands. If no commands are in the queue, the scheduler is left in "hold" mode (it won't execute subsequently buffered commands).

USAGE: runqueue

CLASS: instant

schedule - Submit a schedule to the tcp. NOTE that this command operates differently from the tcp itself (in the trailer) than from a remote connection. From a remote connection, the command is intercepted by the UNIX server program and a schedule is searched for in the snout file system. From the console of the control pc in the trailer, a schedule file is searched for on the pc's file system. It is undesirable to be able to access the DOS filesystem remotely because it is not stable: failure to find a file may cause the control program to crash.

For the case of a remotely submitted schedule, the operations are as follows. 1) The tcp is put into buffering mode. 2) The contents of the schedule file are sent line-by-line. 3) The tcp performs a rudimentary parse of each line as it arrives; gross errors or unkown commands will produce error messages. A successful read will generate no error messages. The scheduler is in any case left in a buffering, non-executing state. To initiate execution, the user must issue a "run" command.

USAGE: schedule (filename) filename should include the full path.

CLASS: background

WARNING: currently no more than about 150 commands may be stored in the queue.

schsub - Read a schedule into the queue from the local DOS file system. Since this command is not an instant

service - Send the telescope to 310 degrees az, 90 degrees elevation.

USAGE: service

CLASS: foreground

setsource - Set the source tag manually.

USAGE: setsource (name)

CLASS: foreground

showqueue - Show the queue of current commands, starting with the next to be executed.

USAGE: showqueue

CLASS: instant

status - Request a status update to be sent out on the network.

USAGE: status

CLASS: instant

stow - Send the telescope to 0 degrees az, 60 degrees el.

USAGE: stow

CLASS: foreground

testproc - a debugging procedure

CLASS: background

timeproc - a debugging procedure

CLASS background

track - Enable/Disable tracking. With tracking disabled, the telescope does not move.

USAGE: track (on—off)

CLASS: foreground

(window)

wrap - Force the telescope to a preset position in the specified wrap. For a "wrap cw" request, this is az=180; for a "wrap ccw" request this is az=0.

The cw wrap limit is +33.34 degrees of azimuth; the ccw limit is +262.34 (-96.66) degrees of azimuth. The cw sector is defined to be from +130 degrees to +33.34 degrees azimuth (inclusive clockwise); the ccw sector is defined to be from +130 to -96.66 degrees azimuth (inclusive counterclockwise).

USAGE: wrap (cw—ccw)

CLASS: foreground

APROPOS: autowrap position

Scheduler Logic
================================

The scheduler is simply a set of rules for putting commands into and taking commands out of a command queue. There are 4 commands which determine the state of the scheduler: buffer/nobuff (which determine if incoming commands are put into the queue or not) and runqueue/hold (which determine whether or not commands are being taken out of the queue, i.e., executed). The default state is nobuff/hold. If there are commands in the queue, any of the four possible states are valid; otherwise, nobuff/hold is set by default.

There are three classes of commands which have different interactions with the scheduler. The distinctions between these three are only important if the scheduler is buffering commands and/or there is a command currently executing. 1) foreground commands: These are commands which require the undivided attention of the tcp, and should not be allowed to occur while other (foreground) commands are executed. Generally any commands which require a finite amount of time to execute, where finite is defined in an arbitrary way, are classified as foreground commands, as well as those which change the tracking/radiometric state of the tcp. If the scheduler is buffering, these commands are put at the end of the queue. Otherwise they are executed (if no other command is executing) or thrown away (if there's another command executing). 2) background commands: These are commands which do not require the undivided attention of the tcp in that it they do not affect radiometry or tracking. They are therefore executed even if another command is executing at the time they are received, unless the scheduler is buffering, in which case they are put at the end of the queue. 3) instant commands: Instant commands are always executed instantly, regardless of the state of the scheduler/execution queue. These commands include, for example, the command to start running the queue and the "quit" command.

Regardless of the buffering state of the scheduler, a rudimentary level of parsing is performed on user input on a line-by-line basis (as the commands are received by the tcp). In general this level of parsing is sufficient only to reject unkown commands; in particular, keyword/value pairs are not in general processed until execution. One exception is the start/stop times associated with radiometry procedures, which are tested for proper time format at the time they are first received. Bad keywords or values therefore may cause unexpected behavior of the tcp but will not cause fatal errors (unlike the original version!).

The start and stop times associated with radiometry procedures are interpreted as LST's. The start and stop times define a necessary conditions for the execution of the procedure: (time > start) && (time < stop). If only one time is given, only this condition is applied. Start times lying more than 12 hours in the future are interpreted as lying in the past, and the procedure is skipped.

Basic Control Scheme
==================================

The pc in the trailer controls the telescope by talking to the 3840 (pedestal control unit) through a serial line; switched power is sampled from a lock-in-amplifier via GPIB interface; total power is sampled from an HP power-meter via GPIB also. The telescope control program (tcp) runs on this pc. The pc talks to the rest of the world via tcp/ip sockets. In the configuration we have chosen, the tcp runs under DOS with FTP software's Terminate and Stay Resident (TSR) tcp/ip kernal allowing the tcp to use standard BSD sockets to talk to other programs. The pc's network name is flute.ovro.caltech.edu.

A sockets server intermediate between the pc itself and client terminal interface programs (tip's) has been set up, allowing the more network-accessible UNIX filesystem to be exploited for schedule file storage and retrieval, and logfile access. This program, the so-called flute server or fsrv, is in constant communication with flute and records all logfile output of the tcp in a standard directory (currently /scr/cm/mason/1m/log). Other clients, remote or local, may connect to fsrv at any time; input received from these clients is relayed to the tcp, and tcp output is relayed to currently active clients on request.

A tcl/tk semi-graphical tip has been constructed (tip1m). This is the standard client for fsrv.

In practice it has been found that the most convenient mode of operation is locally initially, remotely logged observation. This permits the observer to carefully check all aspects of the instrumental setup prior to the start of observations and monitor the progress of observations as they occur.

All logfiles are currently in /scr/cm/mason/1m/log on snout, and the equivalent directories on snug and cosmo. Snout is the location to which fsrv itself archives the data. Data are recorded in a form consistent with 5m/40m logfile format and consequently readable by cmbprog, etc.

Appendix E

NVSS-Selected Discrete Source Survey

Source	RA	Dec.	$S_{18.5}$	$S_{4.85}$	$S_{1.4}$
001802−0903	00:18:02.20	−09:03:14.4	5.31 ± 1.33	—	52.30 ± 2.50
002023−0915	00:20:23.37	−09:15:16.0	15.92 ± 1.44	—	33.70 ± 1.80
004024−0915	00:40:24.36	−09:15:27.3	13.86 ± 1.28	—	22.60 ± 5.40
004129−0922	00:41:29.21	−09:22:40.1	5.19 ± 1.65	—	39.60 ± 7.10
004151−0925	00:41:51.05	−09:25:48.0	15.00 ± 2.0	—	67.80 ± 3.10
010621−0928	01:06:21.59	−09:28:32.2	4.11 ± 0.78	—	15.20 ± 1.50
084852−0955	08:48:52.84	−09:55:25.2	3.45 ± 1.05	—	51.30 ± 2.50
084912−0928	08:49:12.03	−09:28:01.6	11.89 ± 2.33	—	24.90 ± 1.50
090802−0959	09:08:02.38	−09:59:40.9	46.24 ± 5.64	—	84.00 ± 7.80
090806−1001	09:08:06.21	−10:01:28.6	10.40 ± 2.00	—	16.30 ± 10.10
090824−0933	09:08:24.41	−09:33:37.2	41.19 ± 3.05	121 ± 5.0	153.20 ± 6.20
090829−0927	09:08:29.61	−09:27:38.1	6.33 ± 0.82	—	56.30 ± 2.70
090918−0943	09:09:18.14	−09:43:15.8	511.55 ± 1.83	33 ± 4	8.40 ± 2.20
090930−0923	09:09:30.99	−09:23:10.6	28.05 ± 2.05	194 ± 5	61.70 ± 6.40
090932−0922	09:09:32.16	−09:22:18.9	18.12 ± 1.61	—	30.80 ± 5.30
090954−1003	09:09:54.60	−10:03:08.8	6.06 ± 0.84	—	85.70 ± 3.90
091015−0934	09:10:15.03	−09:34:28.3	8.01 ± 0.89	—	43.50 ± 7.10
091017−0937	09:10:17.55	−09:37:03.4	33.51 ± 0.90	—	26.20 ± 5.20
091021−0936	09:10:21.31	−09:36:31.2	19.70 ± 0.4	161 ± 5	8.20 ± 0.5
091022−0935	09:10:22.73	−09:35:18.5	6.83 ± 0.90	—	92.50 ± 8.60
092659−0930	09:26:59.80	−09:30:09.1	3.75 ± 0.96	—	6.50 ± 0.50
092718−0929	09:27:18.30	−09:29:25.0	3.65 ± 0.93	—	25.30 ± 1.70
092722−0927	09:27:22.90	−09:27:50.7	3.50 ± 0.95	—	13.30 ± 1.50
092730−0926	09:27:30.57	−09:26:35.8	4.51 ± 0.87	—	38.70 ± 2.00
151226+0553	15:12:26.85	+05:53:02.5	2.50 ± 0.75	—	9.90 ± 1.30
145327+0545	14:53:27.15	+05:45:39.3	3.20 ± 0.83	—	19.30 ± 0.70
145426+0555	14:54:26.25	+05:55:43.5	2.81 ± 0.76	—	32.90 ± 1.10
145434+0536	14:54:34.91	+05:36:50.0	6.04 ± 0.89	—	50.30 ± 2.40
145452+0547	14:54:52.84	+05:47:52.9	4.38 ± 0.56	—	7.10 ± 0.50
150947+0545	15:09:47.20	+05:45:17.0	67.83 ± 2.46	153.00 ± 22.00	—
151141+0518	15:11:41.18	+05:18:09.6	535.27 ± 15.45	59.6 ± 1.8	501.00 ± 70.00
152707+0552	15:27:07.03	+05:52:15.2	4.07 ± 1.20	—	16.70 ± 1.20
152746+0543	15:27:46.32	+05:43:24.0	14.68 ± 1.16	—	4.50 ± 7.90
152805+0544	15:28:05.02	+05:44:28.5	30.84 ± 1.01	—	47.00 ± 1.80
152823+0546	15:28:23.98	+05:46:40.3	4.93 ± 0.94	—	53.30 ± 5.30
152831+0546	15:28:31.63	+05:46:55.5	5.69 ± 1.06	—	78.80 ± 4.90
152834+0547	15:28:34.55	+05:47:54.0	13.24 ± 1.34	—	44.00 ± 2.70
152844+0552	15:28:44.59	+05:52:17.5	31.40 ± 0.91	—	45.80 ± 4.40

Table E.1: OVRO 40-m 18.5 GHz flux densities for the point sources in the LEAD, MAIN, and TRAIL fields of A85, A754, and A2029. The field positions that we searched are shown in Table E.3.

Source	α	S_{32}
001802−0903	−0.89	3.27 ± 0.99
002023−0915	−0.29	13.58 ± 1.50
004024−0915	−0.84	8.73 ± 0.98
004129−0922	−0.79	3.37 ± 1.31
004151−0925	−0.58	10.89 ± 1.76
010621−0928	−0.51	3.11 ± 0.72
084852−0955	−1.05	1.95 ± 0.72
084912−0928	−0.29	10.16 ± 2.42
090802−0959	−0.54	34.49 ± 5.11
090806−1001	−1.18	5.46 ± 1.27
090824−0933	−0.45	39.65 ± 1.99
090829−0927	−0.85	3.98 ± 0.63
090918−0943	0^A	511.55 ± 1.83
090930−0923	−0.54	33.54 ± 1.39
090932−0922	−0.77	11.91 ± 1.29
090954−1003	−1.03	3.45 ± 0.58
091015−0934	−1.12	4.34 ± 0.59
091017−0937	−0.51	25.29 ± 0.85
091021−0936	1.19	15.15 ± 1.90
091022−0935	−1.29	3.36 ± 0.54
092659−0930	−0.21	3.34 ± 1.04
092718−0929	−0.75	2.42 ± 0.75
092722−0927	−0.52	2.64 ± 0.87
092730−0926	−0.83	2.86 ± 0.67
151226+0553	−0.53	1.87 ± 0.68
145327+0545	−0.70	2.19 ± 0.69
145426+0555	−0.95	1.67 ± 0.55
145434+0536	−0.82	3.85 ± 0.69
145452+0547	−0.19	3.95 ± 0.62
150947+0545	0.41	43.42 ± 15.29
151141+0518	0^A	535.27 ± 15.45
152707+0552	−0.55	3.02 ± 1.08
152746+0543	−1.02	8.39 ± 0.81
152805+0544	−0.16	28.20 ± 1.14
152823+0546	−0.92	2.97 ± 0.69
152831+0546	−1.02	3.26 ± 0.74
152834+0547	−0.47	10.26 ± 1.27
152844+0552	−0.59	22.67 ± 0.81

[A] Indications of variability; $\alpha = 0$ assumed.

Table E.2: 32 GHz flux densities for the sources in Table E.1.

Source	RA	Dec.
A85L23	00:18:51.31	−09:17:56.34
A85	00:41:51.31	−09:17:56.34
A85T23	01:04:51.31	−09:17:56.34
A754L19	08:50:15.75	−09:41:10.15
A754	09:09:15.75	−09:41:10.15
A754T19	09:28:15.75	−09:41:10.15
A2029L17	14:53:31.95	+05:44:37.96
A2029	15:10:55.95	+05:44:37.96
A2029T17	15:28:19.95	+05:44:37.96

Table E.3: Field positions used in the NVSS point source search.

Bibliography

Abell G.O., 1958, Astrophys. J. Suppl., 3, 211

Abell G.O., Corwin H G. J., Olowin R.P., 1989, Astrophys. J. Suppl., 70, 1

Abramopoulos F., Ku W.H.M., 1983, Astrophys. J., 271, 446

Allen S.W., Fabian A.C., Johnstone R.M., White D.A., Daines S.J., Edge A.C., Stewart G.C., 1993, Mon. Not. R. Astr. Soc., 262, 901

Anders E., Grevesse N., 1989, Geochimica et Cosmochimica Acta, 53, 197

Baars J.W.M., Genzel R., Pauliny-Toth I.I.K., Witzel A., 1977, Astron. Astrophys., 61, 99

Bahcall J.N., Sarazin C.L., 1977, Astrophys. J. Letters, 213, L99

Bahcall N.A., Ostriker J.P., Perlmutter S., Steinhardt P.J., 1999, Science, 284, 1481

Baird R.C., Newell A.C., Stubenrauch C.F., 1988, IEEE Transactions on Antennas and Propagation, 36, 727

Biggs A.D., Browne I.W.A., Helbig P., Koopmans L.V.E., Wilkinson P.N., Perley R.A., 1999, Mon. Not. R. Astr. Soc., 304, 349

Birkinshaw M., 1999, Phys.Rept., 310, 97

Birkinshaw M., Hughes J.P., 1994, Astrophys. J., 420, 33

Birkinshaw M., Hughes J.P., Arnaud K.A., 1991, Astrophys. J., 379, 466

Briel U.G., Henry J.P., 1994, Nature, 372, 439

Briel U.G., Henry J.P., 1996, Astrophys. J., 472, 131

Briel U.G., Henry J.P., Boehringer H., 1992, Astron. Astrophys., 259, L31

Burles S., Tytler D., 1998, Astrophys. J., 507, 732

Carlstrom J.E., Joy M., Grego L., 1996, Astrophys. J. Letters, 456, L75

Cavaliere A., Fusco-Femiano R., 1976, Astrophys. J., 49, 137

Cavaliere A., Danese L., De Zotti G., 1979, Astron. Astrophys., 75, 322

Chaboyer B., Demarque P., Kernan P.J., Krauss L.M., 1998, Astrophys. J., 494, 96

Challinor A., Lasenby A., 1998, Astrophys. J., 499, 1

Condon J.J., Cotton W.D., Greisen E.W., Yin Q.F., Perley R.A., Taylor G.B., Broderick J.J., 1998, Astron. J., 115, 1693

Conway R.G., Kellermann K.I., Long R.J., 1963, Mon. Not. R. Astr. Soc., 125, 261

Daisuke N., Sulkanen M.E., Evrard A.E., 1999, Mon. Not. R. Astr. Soc., submitted

Dalton G.B., Efstathiou G., Maddox S.J., Sutherland W.J., 1994, Mon. Not. R. Astr. Soc., 269, 151

D'Antona F., Caloi V., Mazzitelli I., 1997, Astrophys. J., 477, 519

David L.P., Slyz A., Jones C., Forman W., Vrtilek S.D., Arnaud K.A., 1993, Astrophys. J., 412, 479

Devlin M.J., De Oliveira-Costa A., Herbig T., Miller A.D., Netterfield C.B., Page L.A., Tegmark M., 1998, Astrophys. J. Letters, 509, L69

Ebeling H., Voges W., Bohringer H., Edge A.C., Huchra J.P., Briel U.G., 1996, Mon. Not. R. Astr. Soc., 281, 799

Edge A.C., Stewart G.C., Fabian A.C., Arnaud K.A., 1990, Mon. Not. R. Astr. Soc., 245, 559

Efanov V., Moiseev I., Kislayoakov A., Naumov A., 1971, Icarus, 14, 198

Epstein E.E., 1971, Icarus, 14, 214

Evrard A.E., Metzler C.A., Navarro J.F., 1996, Astrophys. J., 469, 494

Fassnacht C.D., 1999, Determining the Distance Scale with CLASS: Studies of Two New Gravitational Lenses and a Measurement of the Hubble Constant. Ph.D. thesis, California Inst. of Tech., Pasadena, CA.

Fixsen D.J., Cheng E.S., Gales J.M., Mather J.C., Shafer R.A., Wright E.L., 1996, Astrophys. J., 473, 576

Francis M., 1998, private communication

Francis M.H., Kremer D.P., Repjar A.G., 1990, Microwaves & RF, 29, 77

Fritz G., Davidsen A., Meekins J.F., Friedman H., 1971, Astrophys. J. Letters, 164, L81

Garmire G.P., Nousek J.A., Apparao K.M.V., Burrows D.N., Fink R.L., Kraft R.P., 1992, Astrophys. J., 399, 694

Giacconi R., Murray S., Gursky H., Kellogg E., Schreier E., Tananbaum H., 1972, Astrophys. J., 178, 281

Grainge K., Jones M., Pooley G., Saunders R., Baker J., Haynes T., Edge A., 1996, Mon. Not. R. Astr. Soc., 278, L17

Grego L., 1998, Galaxy Cluster Gas Fractions From Interferometric Measurements of the Sunyaev-Zel'dovich Effect. Ph.D. thesis, California Institute of Technology, Pasadena, CA

Gregory P.C., Condon J.J., 1991, Astrophys. J. Suppl., 75, 1011

Griffith M.R., Wright A.E., 1993, Astron. J., 105, 1666

Gull S.F., Northover K.J.E., 1976, Nature, 263, 572

Gunn K.F., Thomas P.A., 1996, Mon. Not. R. Astr. Soc., 281, 1133

Gursky H., Kellogg E., Murray S., Leong C., Tananbaum H., Giacconi R., 1971, Astrophys. J. Letters, 167, L81

Hemmati H., Mather J.C., Eichhorn W.L., 1985, Applied Optics, 24, 4489

Herbig T., 1994, A measurement of the Sunyaev-Zeldovich effect in the Coma cluster of galaxies. Ph.D. thesis, California Inst. of Tech., Pasadena, CA.

Herbig T., Lawrence C.R., Readhead A.C.S., Gulkis S., 1995, Astrophys. J. Letters, 449, L5

Herrnstein J.R., 1999, In Highly Redshifted Radio Lines, ASP Conf. Series Vol. 156, Ed. by C. L. Carilli, S. J. E. Radford, K. M. Menten, & G. I. Langston., p. 275, astro-ph/9803039

Hobbs R., Knapp S., 1971, Icarus, 14, 204

Holzapfel W.L., et al., 1997, Astrophys. J., 480, 449

Hubble E., Humason M.L., 1931, Astrophys. J., 74, 43

Hughes J.P., Gorenstein P., Fabricant D., 1988a, Astrophys. J., 329, 82

Hughes J.P., Yamashita K., Okumura Y., Tsunemi H., Matsuoka M., 1988b, Astrophys. J., 327, 615

Irwin J.A., Bregman J.N., Evrard A.E., 1999, Astrophys. J., in press

Itoh N., Kohyama Y., Nozawa S., 1998, Astrophys. J., 502, 7

Iwasawa K., Fabian A., Nandra K., 1999, Mon. Not. R. Astr. Soc., in press

Jensen J.B., Tonry J.L., Luppino G.A., 1999, Astrophys. J., 510, 71

Jones M.E., Scott P., 1998, In Proceedings of the XXXIII Rencontres de Moriond

Kellermann K.I., 1964, Astrophys. J., 140, 969

Kellermann K.I., Pauliny-Toth I.I.K., Williams P.J.S., 1969, Astrophys. J., 157, 1

Klein M.J., Gulkis S., 1978, Icarus, 35, 44

Kolb E.W., Turner M.S., 1990, The early universe. Frontiers in Physics, Reading, MA: Addison-Wesley

Krauss J., 1986, Radio Astronomy. Cygnus-Quasar, Ohio

Kundic T., et al., 1997, Astrophys. J., 482, 75

Leitch E., 1998, A Measurement of Anisotropy in the Microwave Background on $7' - 22'$ Scales. Ph.D. thesis, California Inst. of Tech., Pasadena, CA.

Leitch E., Readhead A., Pearson T., Myers S.T., Gulkis S., 1999, Astrophys. J., in press

Lo Y., Lee S., eds., 1993, Antenna Handbook Vol. IV, New York, Van Nostrand Reinhold

Madore B.F., Freedman W.L., 1998, Astrophys. J., 492, 110

Madore B.F., et al., 1999, Astrophys. J., 515, 29

Markevitch M., 1999, Astrophys. J., in press

Markevitch M., Forman W.R., Sarazin C.L., Vikhlinin A., 1998, Astrophys. J., 503, 77

Marshall F.J., Clark G.W., 1984, Astrophys. J., 287, 633

Miller A.D., Caldwell R., Herbig T., Page L., Torbet E., Tran H., Devlin M., Puchalla J., 1999, Astrophys. J., submitted

Mitchell R.J., Culhane J.L., Davison P.J.N., Ives J.C., 1976, Mon. Not. R. Astr. Soc., 175, 29P

Mohr J.J., Mathiesen B., Evrard A.E., 1999, Astrophys. J., in press,astro-ph/9901281

Morsi H., 1997. Private communication

M^{c}Cammon D., Burrows D.N., Sanders W.T., Kraushaar W.L., 1983, Astrophys. J., 269, 107

Myers S.T., Baker J.E., Readhead A.C.S., Leitch E.M., Herbig T., 1997, Astrophys. J., 485, 1

National Institute of Standards and Technology, 1990, Nist report of special test on 1.5-m offset cassegrain clear aperture antenna at 32 ghz. Tech. rep., NIST

Navarro J.F., Frenk C.S., White S.D.M., 1995, Mon. Not. R. Astr. Soc., 275, 720

Netterfield C.B., Devlin M.J., Jarolik N., Page L., Wollack E.J., 1997, Astrophys. J., 474, 47

Neumann D., Arnaud M., 1999, Astron. Astrophys., submitted

Newell A.C., Ward R.D., MCFarlane E.J., 1988, IEEE Transactions on Antennas and Propagation, 36, 792

Nulsen P.E.J., 1986, Mon. Not. R. Astr. Soc., 221, 377

Penzias A.A., Wilson R.W., 1965, Astrophys. J., 142, 419

Peres C.B., Fabian A.C., Edge A.C., Allen S.W., Johnstone R.M., White D.A., 1998, Mon. Not. R. Astr. Soc., 298, 416

Perlmutter S., et al., 1999, Astrophys. J., 517, 565

Press W.H., Teukolsky S.A., Vetterling W.T., Flannery B.P., 1992, Numerical recipes in C. The art of scientific computing 2nd ed. Cambridge University Press, Cambridge

Rahmat-Samii Y., 1993, In Matsumoto H., ed., Modern Radio Science

Raymond J.C., Smith B.W., 1977, Astrophys. J. Suppl., 35, 419

Readhead A., Padin S., Pearson T., Cartwright J., Myers S.T., 1999, Publs. Astr. Soc. Pacif., in preparation, also http://astro.caltech.edu/~tjp/CBI/

Readhead A.C.S., Lawrence C.R., Myers S.T., Sargent W.L.W., Hardebeck H.E., Moffet A.T., 1989, Astrophys. J., 346, 566

Reid I.N., 1997, Astron. J., 114, 161

Rephaeli Y., 1995, Astrophys. J., 445, 33

Riess A.G., et al., 1998, Astron. J., 116, 1009

Rohlfs K., Wilson T.L., 1996, Tools of Radio Astronomy. Springer-Verlag, Berlin Heidelberg New York

Rybicki G.B., Lightman A.P., 1979, Radiative processes in astrophysics. Wiley-Interscience, New York

Sandage A., Saha A., Tammann G.A., Labhardt L., Panagia N., Macchetto F.D., 1996, Astrophys. J. Letters, 460, L15

Sarazin C.L., 1988, X-ray emission from clusters of galaxies. Cambridge Astrophysics Series, Cambridge University Press, Cambridge

Sazonov S.Y., Sunyaev R.A., 1998, Astrophys. J., 508, 1

Scaramella R., Zamorani G., Vettolani G., Chincarini G., 1991, Astron. J., 101, 342

Schutz B.F., 1985, A first course in general relativity. Cambridge University Press, Cambridge

Snowden S.L., M^{c}Cammon D., Burrows D.N., Mendenhall J.A., 1994, Astrophys. J., 424, 714

Snowden S.L., et al., 1995, Astrophys. J., 454, 643

Sodre L. J., Capelato H.V., Steiner J.E., Proust D., Mazure A., 1992, Mon. Not. R. Astr. Soc., 259, 233

Stanek K.Z., Zaritsky D., Harris J., 1998, Astrophys. J. Letters, 500, L141, astro-ph/9803181

Struble M.F., Rood H.J., 1991, Astrophys. J. Suppl., 77, 363

Sunyaev R.A., Zeldovich I.B., 1970, Astrophys. Space Sci., 7, 3

Sunyaev R.A., Zeldovich I.B., 1980, Mon. Not. R. Astr. Soc., 190, 413

Tegmark M., Efstathiou G., 1996, Mon. Not. R. Astr. Soc., 281, 1297

Thomas P., 1988, Mon. Not. R. Astr. Soc., 235, 315

Thomsen B., Baum W.A., Hammergren M., Worthey G., 1997, Astrophys. J. Letters, 483, L37

Tonry J., Schneider D.P., 1988, Astron. J., 96, 807

Torbet E., et al., 1999, Astrophys. J., in press, astro-ph/9905100

Trafton L.M., 1965, A Study Of The Energy Balance In The Atmospheres Of The Major Planets. Ph.D. thesis, California Institute Of Technology

Ulich B.L., 1981, Astron. J., 86, 1619

Van Haarlem M.P., Frenk C.S., White S.D.M., 1997, Mon. Not. R. Astr. Soc., 287, 817

Vettolani G., Chincarini G., Scaramella R., Zamorani G., 1990, Astron. J., 99, 1709

Vikhlinin A., Forman W., Jones C., 1999, Astrophys. J., in press

Wang L., Caldwell R., Ostriker J., Steinhardt P.J., 1999, Cosmic concordance and quintessence. Astro-ph/9901388

Waxman E., Miralda-Escude J., 1995, Astrophys. J., 451, 451

Weinberg S., 1972, Gravitation and cosmology: Principles and applications of the general theory of relativity. Wiley, New York

White D.A., Fabian A.C., 1995, Mon. Not. R. Astr. Soc., 273, 72

White M., Carlstrom J.E., Dragovan M., Holzapfel W.L., 1999, Astrophys. J., 514, 12

Wright M., Dickel J., Koralesky B., Rudnick L., 1999. Astro-ph/9901417

Wrixon G., Welch W., Thornton D., 1971, Astrophys. J., 169, 171